University of Nebraska Medical Center
BREAKTHROUGHS FOR LIFE

University of Nebraska Medical Center
DigitalCommons@UNMC

Theses & Dissertations

Graduate Studies

Summer 8-19-2016

Assessment and Mechanisms of Autonomic Function in Health and Disease

Peter Ricci Pellegrino
University of Nebraska Medical Center

Follow this and additional works at: https://digitalcommons.unmc.edu/etd

Recommended Citation

Pellegrino, Peter Ricci, "Assessment and Mechanisms of Autonomic Function in Health and Disease" (2016). *Theses & Dissertations*. 129.
https://digitalcommons.unmc.edu/etd/129

This Dissertation is brought to you for free and open access by the Graduate Studies at DigitalCommons@UNMC. It has been accepted for inclusion in Theses & Dissertations by an authorized administrator of DigitalCommons@UNMC. For more information, please contact digitalcommons@unmc.edu.

Assessment and Mechanisms of Autonomic Function in Health and Disease

by

Peter Ricci Pellegrino

A DISSERTATION

Presented to the Faculty of
the University of Nebraska Graduate College
in Partial Fulfillment of the Requirements
for the Degree of Doctor of Philosophy

Cellular & Integrative Physiology
Graduate Program

Under the Supervision of Professor Irving H. Zucker

University of Nebraska Medical Center

Omaha, Nebraska

August 2016

Supervisory Committee:

Babu J. Padanilam, Ph.D.
Debra Romberger, M.D.
Harold D. Schultz, Ph.D.
Matthew C. Zimmerman, Ph.D.

Acknowledgements

Done properly, this section would be longer than the rest of the dissertation. I feel commissioning statues more appropriate than writing a few words; know that my gratitude far exceeds the confines of these pages.

I will start by thanking Dr. Zucker, who as a great mentor has supported me beyond reason over the last four years. He took a chance by letting me join the lab without doing a traditional summer rotation, continued to help me troubleshoot absolutely everything as my project evolved over the years, and even, with one eyebrow raised with well-intentioned concern, ordered rabbits for me to do new experiments just a few weeks ago. He is eminently approachable despite the many demands on his time, and he always provides important insight into any issue, research or otherwise. His deep enthusiasm for and tireless dedication to his craft is unlike anything I had ever known before and something that I hope to one day emulate.

The rest of the Zucker Laboratory was instrumental in my doctoral journey. Dr. Hanjun Wang's exuberance, work ethic, and brilliance give me hope that Dr. Zucker's qualities might be contagious. Dr. Gao taught me to perform rabbit surgery and was always very approachable for any issue. Kaye's immeasurable patience and attention to detail were crucial to the success of these projects and my sanity. Johnnie helped me recover from my most grave mistakes and continues to this day to help me with even the most elementary things. Tara, instead of shaming me for my going-out-of-business-sale approach to experiments the last few months, has gone above and beyond to help me. Karla dealt with my ineptitude with molecular techniques and everything else with supreme patience and was a heartfelt mentor. Bryan Becker lent his steady, selfless demeanor to any problem I faced. Alicia, with whom I collaborated extensively, is someone who can honestly do anything and is probably the true source of many of the ideas I will present as my own in the coming chapters. Thanks to the new graduate students May and Ahmed for making me feel like I have something to teach even though I suspect they already know more than me.

I also need to express my gratitude to my committee, whose support I appreciate and whose perspectives shaped both my project and my development as an aspiring scientist over the last four years. Dr. Padanilam always posed important, multi-layered questions. Dr. Romberger, despite her extremely busy schedule, always made time to help me, whether with fellowship applications, career advice, or introductions to clinical faculty. Dr. Schultz chaired the committee for my comprehensive exam, helped me develop respiratory curriculum for physiology recitation, and provided critical research discussion. Dr. Zimmerman offered me great advice based on his own graduate and career experience and always offered important perspective in committee meetings.

To the other CIP trainees with whom I have shared comradery and growth, thank you all. I have had positive interactions with all of the other CIP faculty, and I am thankful for their support over the last several years. To the CIP administrative staff, Cindy, Pearl, Kim, and Deb, you ladies rock. Thank you to the M.D./Ph.D. Scholars Program, especially to Dr. Shelley Smith for her encouragement and Sonja Cox for her tireless support and helpfulness.

To the many mentors I have had before arriving in Omaha, including Vincent Magnotta, Bob Chiusano, Jeremy Maniak, Ralph Cardinal, Chandan Reddy, and Sergio Martinoia, thank you. Thank you to my dear friends whom I miss every day. To Adriana, my dearest friend, for her steadfast support and boundless warmth. To Candice, for her enthusiasm and energy. To my big brother Jose and his girls Tonia and Sofia, mi mancate. To Laura for her undying belief in me. To Richard, Arman, and Joe for their refusal to let busy schedules, geographical separation, and my reclusive nature get in the way of our friendships.

For my angel, I try every day to make you proud. My parents, two of the greatest, most loving people I have ever known, whose support made it impossible for me to fail as someone of my capacities and defects should. To my adoring sister Lynn and my nephew Giuseppino, I love you both very much. To my girls, the lights of my life, I live every day for your happiness. You are the reason I dream at night and rise from bed in the morning. Thank you for making me the richest man on Earth.

Assessment and Mechanisms of Autonomic Function in Health and Disease: A Role of Central Rho Kinase

Peter Ricci Pellegrino

University of Nebraska Medical Center, 2016

Supervisor: Irving H. Zucker, Ph.D.

The autonomic nervous system is a master regulator of homeostasis, and the conviction that autonomic outflow is important on a patient-by-patient, minute-to-minute basis in both health and disease is the motivation for this thesis. The dissertation explores three aims that advance our understanding of the autonomic nervous system by elucidating the molecular mechanisms of autonomic regulation, validating widely used techniques for autonomic assessment, and developing and applying a new method to assess sympathetic vascular control.

The first aim of the dissertation was to investigate the role of the Rho kinase pathway as a mediator of the autonomic effects of central angiotensin-II. This study was performed in conscious, chronically instrumented rabbits that received intracerebroventricular infusions of angiotensin-II, angiotensin-II with the specific Rho kinase inhibitor Fasudil, Fasudil alone, or a vehicle control over two weeks. Baseline hemodynamics were assessed daily, and cardiac and global vasomotor sympathetic tone was assessed by the hemodynamic response to autonomic blockers. Angiotensin-II raised blood pressure and cardiac and global vasomotor sympathetic outflow in a Rho-kinase dependent manner. In a separate cohort, renal sympathetic nerve activity was directly recorded and sympathetic baroreflex sensitivity was assessed, providing clear evidence that angiotensin-II increases renal sympathetic nerve activity and impairs baroreflex control thereof via a Rho kinase-dependent mechanism. In summary, the pressor, sympatho-excitatory, and baroreflex dysfunction caused by central angiotensin-II depend on Rho kinase activation.

The second aim was to investigate the relationship between measures of pulse rate variability obtained by a chronically implanted arterial pressure telemeter with measures of heart rate variability derived by the standard electrocardiogram and the ability of pulse rate variability to reflect the autonomic contributions of heart rate variability. This study was conducted in conscious rabbits chronically instrumented with epicardial leads and arterial pressure telemeters. The autonomic contribution to pulse rate variability was assessed by pharmacological blockade, and the intrinsic variability of pulse rate was assessed by ventricular pacing. This study showed that pulse rate variability is a generally acceptable surrogate for heart rate variability for time- and frequency-domain measures, but the additional contribution of respiration to and the differing nonlinear properties of pulse rate variability should be considered by investigators.

The third aim was to critically test the idea that the renal sympathetic nerves do not participate in the physiological control of renal blood flow. This study was conducted in conscious rabbits that underwent unilateral renal denervation and chronic instrumentation with arterial pressure telemeters and bilateral renal blood flow probes. Using time-varying transfer function analysis, this study showed active, rhythmic vasoconstriction of the renal vasculature with baroreflex properties in normally innervated kidneys, consistent with sympathetic vasomotion, which was absent in denervated kidneys. This refutes the long-held idea that sympathetic control of the renal vasculature is not physiological and has important applications to the burgeoning field of therapeutic renal denervation for cardiovascular disease.

Table of Contents

List of Figures

List of Tables

List of Abbreviations

3D	three-dimensional
aCSF	artificial cerebrospinal fluid
Ang II	angiotensin II
ANOVA	analysis of variance
AP	arterial pressure
AT1R	angiotensin type-1 receptor
DBP	diastolic blood pressure
DDNx	bilaterally denervated rabbits
DFA	detrended fluctuation analysis
DNx	denervated
ECFV	extracellular fluid volume
ECG	electrocardiogram
Fas	Fasudil
FFT	Fast Fourier Transform
G	gain
GDP	gross domestic product
GFR	glomerular filtration rate
HF	high-frequency
HR	heart rate
HRV	heart rate variability
ICV	intracerebroventricular
INV	innervated
IV	intravenous
LF	low-frequency
LF/HF	low-frequency to high-frequency ratio
MAP	mean arterial pressure
MR	myogenic response
MSE	multiscale entropy
MYPT	myosin phosphatase
NTS	nucleus tractus solitarii
nu	normalized units

PRV	pulse rate variability
PVH	paraventricular hypothalamus
PVN	paraventricular nucleus of the hypothalamus
RAAS	renin-angiotensin-aldosterone system
RBF	renal blood flow
RM	repeated measure
RMSSD	root mean square of successive differences
ROCK1	Rho-associated protein kinase 1
ROCK2	Rho-associated protein kinase 2
RSNA	renal sympathetic nerve activity
RVLM	rostral ventrolateral medulla
SBP	systolic blood pressure
SDNN	standard deviation of normal-to-normal intervals
SFO	subfornical organ
SNA	sympathetic nerve activity
TBS	Tris-buffered saline
TGF	tubuloglomerular feedback
Veh	artificial cerebrospinal fluid vehicle
VLF	very-low frequency

Introduction

Cardiovascular Disease

Cardiovascular disease is arguably the most significant health problem in American society[1]. Over 85 million American adults have at least one type of cardiovascular disease, and cardiovascular disease has been the leading cause of death in the United States every year since 1900 with the exception of 1918 (when the influenza pandemic made infectious disease the leading cause of death). In 2013, cardiovascular disease was the underlying cause of death in over 30% of mortalities in the United States and played a role in over half of all deaths. The direct and indirect costs of cardiovascular disease in the United States in 2009 totaled $313 billion (>2% of total GDP). On a global scale, cardiovascular disease remains an eminent problem, accounting for over 17 million deaths (~31%) in 2013 and costing $863 billion in 2010 (~1.4% of global GDP).

Hypertension

Hypertension is the most common form of cardiovascular disease, with an estimated prevalence of 80 million in the United States and nearly 1 billion worldwide in 2016[1]. Clinically, hypertension is diagnosed as a systolic blood pressure greater than or equal to 140 mm Hg or diastolic blood pressure greater than or equal to 90 mm Hg at two or more visits although there is growing momentum for the use of ambulatory blood pressure monitoring in diagnosis. Hypertension predisposes to heart failure, stroke, myocardial infarction, and vascular disease. Hypertension is the number one health risk factor in terms of its impact on disability-adjusted life years, and thus the need for new prevention and treatment strategies is significant.

Despite the high clinical burden of hypertension, fundamental gaps in our understanding of the disease remain, and over 90% of incident hypertension is of unknown etiology. Pharmacotherapy is targeted at lowering blood pressure. Thiazide diuretics, calcium channel blockers, angiotensin-converting enzyme inhibitors, and angiotensin receptor blockers are the mainstays of medical therapy, but other classes of drugs, including combined α_1/β-blocking agents, vasodilating β-blockers, central α_2-adrenergic agonists, direct vasodilators, aldosterone receptor

antagonists, adrenergic neuronal depleting agents, and loop diuretics, are also used[2]. On the horizon are non-pharmacological therapies like baroreceptor stimulation, renal denervation, carotid body denervation, and arteriovenous anastomosis for patients with treatment-resistant hypertension[3–5]. Hypertensive patients are also strongly recommended to follow lifestyle like smoking cessation, physical activity, weight loss, and eating a heahy diet low in sodium.

Renin-Angiotensin-Aldosterone System

The renin-angiotensin-aldosterone system (RAAS) is a humoral cascade important in the control of arterial pressure and extracellular fluid volume. Dysregulation of the RAAS is common in hypertension, and, as previously mentioned, the RAAS is an important therapeutic target in hypertension as well as other cardiovascular and renal diseases.

The classical circulating RAAS cascade is controlled by the stimulus-induced release of renin by juxtaglomerular cells in the kidney. Several stimuli are believed to induce renin secretion: decreased afferent arteriolar pressure sensed by renal baroreceptors, decreases in NaCl flux sensed by the macula densa, diminished negative feedback by angiotensin-II (AngII) itself directly on the juxtaglomerular cells, and sympathetic β_1-adrenergic stimulation of the juxtaglomerular cells. The control of renin secretion is a key determinant of systemic RAAS activity as renin regulates the rate-limiting step of the RAAS by cleaving angiotensinogen, secreted constitutively by the liver, to form the biologically inert decapeptide angiotensin-I. Angiotensin-I is then cleaved to form the biologically active octapeptide AngII by the membrane-bound angiotensin-converting enzyme, which is found abundantly in vascular endothelial cells in the lung as well as microvillar brush border cells in the kidney and neuroepithelial cells. AngII, the primary effector peptide of the RAAS, increases blood pressure, expands the extracellular fluid volume, and stimulates the synthesis of aldosterone by binding to the angiotensin type-1 receptor (AT1R) on different cells in the body. Clinically, circulating RAAS activation can be assessed by measuring plasma renin activity. About 60% of essential hypertensive patients have normal plasma renin activity, 15% have

elevated plasma renin activity, and 25% have low plasma renin activity. Unfortunately, this stratification is not useful for predicting the response to particular antihypertensive agents, and plasma renin activity is not routinely measured in the assessment and management of patients with essential hypertension.

In addition to the circulating RAAS, local tissue RAAS have been described in the heart, blood vessels, kidney, adrenal glands, pituitary, adipose tissue, testes, ovaries, skin, carotid body, and brain [6]. Of particular relevance to this dissertation is the fact that all components of the RAAS are present in the central nervous system, and the central RAAS is dysregulated in preclinical models of hypertension[7]. Importantly, even in preclinical models in which plasma renin activity is low, brain RAAS activity is elevated, suggesting that human hypertensive patients may show similar incongruities between circulating and brain RAAS.

This summary only scratches the surface of the RAAS. Other components, including prorenin, renin, angiotensin-III, angiotensin-IV, angiotensin(1-7), aldosterone, the prorenin receptor, angiotensin type-2 receptor, angiotensin type-3 receptor, angiotensin type-4 receptor, the Mas receptor, angiotensin-I converting enzyme 2, chymases, and neprilysin, are also important in physiology and pathophysiology, but they are not central to this dissertation.

The Autonomic Nervous System

The autonomic nervous system is composed of two main branches: the sympathetic and parasympathetic nervous systems. These limbs work in concert to maintain body homeostasis, or, in disease, they may collude to foment dysregulation. All cells in the autonomic nervous system are derived from neural crest cells that migrate via the ventromedial stream to aggregate into ganglia and innervate their target tissues, providing homeostatic control of cardiovascular, respiratory, gastrointestinal, urogenital, cutaneous, and adipose systems. These post-ganglionic autonomic neurons are innervated by pre-ganglionic neurons in the central nervous system, originating either from the lateral spinal cord or the brain stem. Sympathetic preganglionic neurons

in turn receive input from brainstem areas like the rostral ventrolateral medulla (RVLM) and the hypothalamus like the paraventricular nucleus (PVN). The central autonomic nuclei in the brain stem and hypothalamus receive and integrate visceral input from baroreceptor, cardiac receptor, chemoreceptor, and pulmonary mechanoreceptor afferents that terminate in the nucleus tractus solitarii. The main neurotransmitter in both sympathetic and parasympathetic ganglia is acetylcholine, which acts at the ganglionic-type nicotinic receptor to activate post-ganglionic neurons. This ganglionic neurotransmission can be blocked by drugs like hexamethonium and trimetaphan that antagonize the nicotinic receptors in the autonomic ganglia.

Pre-ganglionic neurons of the parasympathetic nervous system originate either cranially in the brain stem or caudally in the lowest levels of the spinal cord. Pre-ganglionic neurons originating in the brain stem travel along cranial nerves III, VII, IX, and X to innervate post-ganglionic neurons. Cranial nerve X is particular in the respect that its pre-ganglionic neurons do not innervate cranial ganglia but instead travel to ganglia innervating the thoracic and abdominal viscera. Everything caudal to the midgut receives its parasympathetic innervation by pelvic splanchnic preganglionic neurons whose cell bodies are located in the lateral gray horn at levels T12-L2 of the spinal cord. Generally, the parasympathetic ganglia are very close to or located within the target organ, so the preganglionic neurons have long axons compared to postganglionic neurons. The main post-ganglionic neurotransmitter in the parasympathetic nervous system is acetylcholine, which mediates its effects by binding to muscarinic receptors. Briefly, parasympathetic outflow causes miosis, ciliary muscle contraction, lacrimation, salivation, decreases in chronotropy, dromotropy, and inotropy, bronchoconstriction, GI motility and secretion, micturition, and erection. The effects of parasympathetic outflow can be blocked by muscarinic receptor blockade with atropine.

Preganglionic sympathetic fibers arise in the lateral gray horn of the thoracic and lumbar segments of the spinal cord and synapse in sympathetic ganglia either in the sympathetic chain or in prevertebral ganglia. Postganglionic neurons whose cell bodies reside in these sympathetic ganglia then innervate target tissues. One notable exception is the chromaffin cells of the adrenal

medulla, which are essentially specialized, secretory postganglionic neurons that release norepinephrine and epinephrine into the circulation in response to preganglionic input. Briefly, the sympathetic nervous system causes pupillodilation, increases in chronotropy, dromotropy. Inotropy, and lusitropy, bronchodilation, GI stasis, urinary retention, uterine contraction and relaxation, ejaculation, vasoconstriction and dilation, sweating, lipolysis, and glycogenolysis. The main post-ganglionic neurotransmitter in the sympathetic nervous system is norepinephrine although many other postganglionic neurotransmitters play specialized roles (e.g., acetylcholine mediates sympathetic sudomotion). Blockade of sympathetic outflow with adrenergic receptor blockers are a mainstay of therapy in cardiovascular disease. Importantly for studies in this thesis, the effects of the sympathetic nervous system on chronotropy can be blocked by administration of a beta-adrenergic blocker like metoprolol.

Closely tied to the motor arms of the autonomic nervous system are visceral afferents, which sense physiologic and pathophysiologic mechanical and chemical stimuli and elicit reflex autonomic responses. Visceral afferents are made up of finely myelinated Aβ and Aδ fibers and unmyelinated C fibers that ascend to the CNS either via the vagus nerve or sympathetic pathways. The nucleus tractus solitarii is a major relay center for visceral afferent traffic, and neurons in the nucleus tractus solitarii project to important autonomic centers involved in the regulation of sympathetic and parasympathetic outflow.

Several important autonomic reflexes are disturbed in experimental and clinical cardiovascular disease, including the cardiopulmonary baroreflex, central/peripheral chemoreceptor reflexes, the cardiac sympathetic afferent reflex, the exercise pressor reflex, and the arterial baroreflex. The arterial baroreflex, a negative feedback loop that acutely buffers changes in systemic perfusion pressure, is a focus of this dissertation. Afferents from baroreceptors in the carotid sinus and aortic arch ascend in cranial nerves IX and X to the nucleus tractus solitarii. This input then projects to the dorsal motor nucleus of the vagus and via the caudal ventrolateral medulla to the rostral ventrolateral medulla. Preganglionic parasympathetic neurons in the dorsal motor

nucleus of the vagus and presympathetic neurons in the rostral ventrolateral medulla form the efferent limb of the reflex. The negative feedback is such that increases in blood pressure are corrected by reflex decreases in heart rate, contractility, total peripheral resistance while decreases in blood pressure are corrected by reflex increases in heart rate, contractility, and total peripheral resistance and decreases in capacitance. This reflex is generally believed to exert tonic sympathoinhibition, and the attenuation of baroreflex sensitivity in cardiovascular disease may explain some of the sympatho-excitation observed in these patients.

In addition to the aforementioned brain stem areas important in autonomic control, several regions of the forebrain merit mention because of their importance in this thesis. The first is the subfornical organ (SFO), a circumventricular organ that mediates the autonomic response to both circulating and intraventricular AngII[8,9]. The second is the paraventricular nucleus of the hypothalamus (PVH), which is a key integrator of visceral stimuli and site of dysregulation in cardiovascular disease[10,11].

Sympatho-excitation in Hypertension

Measures of sympathetic outflow are generally elevated in patients with hypertension and animal models of experimental hypertension; however, sympatho-excitation is not a *sine qua non* of human hypertension as depicted by some clinical researchers. Studies in which muscle sympathetic nerve activity (SNA) was directly recorded indicate that about one third of hypertensive patients have normal sympathetic outflow[12]. Whether or not this heterogeneity in sympathetic outflow reflects differences in etiology, is prognostic for disease sequelae, or could be useful for management of care (e.g., predicting therapy responsiveness) remains to be elucidated.

The factors that have been implicated as causal factors in the sympatho-excitation of hypertension are too numerous to discuss here. Two elements that are central to this dissertation are baroreflex dysfunction and AngII. As discussed previously, the arterial baroreflex inhibits sympathetic outflow in response to increased AP, restoring normal blood pressure levels. Patients

with hypertension show baroreflex resetting to a higher AP although only certain types of hypertensive patients (those with diastolic dysfunction) show blunted baroreflex gain[13].

The capacity of AngII to increase sympathetic outflow was first described over forty years ago [14,15]. Since then, studies have shown the autonomic centers of the brain, including the circumventricular organs, nucleus tractus solitarii, and the rostral ventrolateral medulla, to be important sites for the binding of central AngII[9]. In the central nervous system, AngII raises sympathetic outflow and causes baroreflex resetting and blunting[16]. Over the last twenty years, the intracellular mediators of AT1R signaling in AngII-mediated sympatho-excitation have become an important topic of investigation [17].

RhoA/Rho kinase Pathway

RhoA is a ubiquitously expressed small GTPase that is involved in many fundamental cellular processes. As a small GTPase, it is active in its GTP-bound form and becomes inactivated when its intrinsic GTPase activity hydrolyzes bound GTP to GDP. RhoA is activated by various guanine nucleotide exchange factors, deactivated by GTPase activating proteins. Cytosolic RhoA is inactive, requiring isoprenylation for membrane localization, which can be inhibited by blocking isoprenoid synthesis (e.g., by statins) or isoprenoid transferases. The guanine nucleotide dissociation inhibitors prevent both dissociation of hydrolyzed GDP and membrane translocation, blocking RhoA activation. In vitro studies with dominant positive and dominant negative RhoA mutants have shown a role for RhoA in transcription, cell transformation, cell cycle progression, vesicular trafficking, axonogenesis, dendritic spine formation, cell polarization, cell migration, cell-cell adhesion, nitric oxide bioavailability, and generation of superoxide. Congruent with its importance in these essential processes, RhoA knockout mouse embryos die very early. Rho kinase is the main effector of RhoA. It exists in two isoforms, ROCK1 and ROCK2, which are ubiquitously expressed in the human and mouse[18]. As a serine/threonine kinase, Rho kinase

phosphorylates residues on many target proteins, including adducin, vimentin, LIM-kinase, and the myosin-binding subunit of myosin phosphatase (MYPT). ROCK1 and ROCK2 knockout mice are generally embryonic lethal; less than 10% of C57BL/6 mice survive, dying with open eyes and omphalocele. The most oft-used inhibitors of Rho kinase are Y-27632 and Fasudil (Fas).

This thesis investigates the role of Rho kinase in AngII-mediated autonomic dysfunction. The RhoA/Rho-kinase pathway has been demonstrated to play a key role in Ang II signaling and function in non-neuronal cells, including vascular smooth muscle cells, endothelial cells, and cardiomyocytes[19–22]. Selective knockout of a specific RhoA activator from the vascular smooth muscle cells of mice completely prevents the pressor effect of systemic AngII infusion without affecting basal blood pressure[23]. AngII signaling through the AT1R activates RhoA by several mechanisms, including stimulating RhoGEFs Arhgef1[23] and p63RhoGEF[24] and inhibiting RhoGAP p190A[25]. In the context of cardiovascular disease, Rho kinase activation stimulates formation of the sympatho-excitatory superoxide radical via phosphorylation of p38-MAPK which in turn activates NADPH oxidase, and Rho kinase decreases nitric oxide synthesis by decreasing the nitric oxide synthase activity and destabilizing its mRNA. Thus, central Rho kinase activation by AT1R signaling would be expected to raise sympathetic outflow

Physiological Variability, Autonomic Rhythms, and Pink Noise

All physiological parameters that we measure (e.g., heart rate, arterial pressure, renal blood flow, renal sympathetic nerve activity) display considerable variability over time. The autonomic nervous system is an important source of this physiological variability, and changes in autonomic outflow, either acutely after pharmacological blockade or chronically with the development of disease, alter the variability of physiological parameters. Much of this thesis is dedicated to the investigation of physiological variability and the exploration of the autonomic underpinnings thereof. While measures of physiological variability are prognostic for mortality among patients

with cardiovascular and renal disease, the clinical utility of such measures is very low despite over a century of investigation (and about 45 years using digital signal processing techniques).

The autonomic nervous system is not the only source of variability in physiological parameters, although it is the fastest-acting source of variability. The fact that the autonomic nervous system acts faster than other systems allows one to appreciate its importance even with short-term (~5 minutes in the human) recordings of parameters like heart rate or arterial pressure. This also allows its influence to be examined using frequency analysis, which is a technique by which a signal occurring in time is decomposed into frequency (see Chapter III for a more comprehensive introduction). The sympathetic nervous system makes important contributions to peripheral resistance, arterial pressure, and heart rate variability in the low-frequency (LF) range. The parasympathetic nervous system affects heart rate variability (and thereby arterial pressure variability) in both the LF and high-frequency (HF) ranges. The source of LF oscillations in autonomic rhythms is debated; the two predominant theories are that these rhythms arise either due to a central oscillator that oscillates in this LF range or due to resonance arising from time delays in the baroreflex arc. The HF oscillations in heart rate variability arise due to the mechanical effects of respiration on the circulation, which in create rhythms in autonomic outflow at these frequencies. The reason that only the parasympathetic nervous system can cause HF oscillations in heart rate is due to the presence of fast, muscarinic ionotropic receptors at the sinoatrial node, which allow these HF oscillations in vagal nerve activity to affect heart rate (whereas the slow, adrenergic metabotropic receptors act as a low-pass filter, eliminating such rhythms).

Underlying these rhythmic contributions of the autonomic nervous system to physiological parameters are rhythms in efferent traffic along the autonomic nerves themselves. Sympathetic nerve activity is rhythmic and entrains to the respiratory frequency, which falls in the HF range, and to the cardiac frequency. Another important sympathetic rhythm occurs in the LF range, giving rise to arterial pressure oscillations known as Mayer waves as well as sympathetic rhythms in HR.

One should not introduce short-term physiological variability without talking about pink noise, which is the other significant source of variability in autonomic frequency ranges. Pink noise is so named because it falls somewhere between white (Gaussian) and red (Brownian) noise. White noise is noise with a flat power spectrum (like white light, which contains equal power of all wavelengths in the visible spectrum); each new value of white noise is completely random and independent of the previous value. Red noise is simply the integral of white noise; it is noise where each new value is the sum of a completely random value and the previous value. With many additions, the previous value component outweighs the contribution of the new random values (which may be negative or positive, frequently negating one another), and, with slow changes more common than fast changes, low-frequencies predominate (like red light, the lowest-frequency light in the visible spectrum). The power spectrum for red noise follows a $1/\text{frequency}^2$ power-law. Pink noise is just a bit of red and white noise mixed together, resulting in a 1/frequency power spectrum. Sophisticated techniques can characterize this fractal component of physiological variability [26].

Analyzing physiological signals over the last four years has given me a few insights that I feel are underappreciated and merit emphasis. First, the mean value of a physiological measure is more important than any measure of variability. In many manuscripts, the authors dedicate paragraphs to their discussion of changes in HR variability (HRV) when a change in HR receives only passing mention. Not only is the mean measure more important, but measures of variability correlate in some way with the mean measure, and thus using measures of variability in the presence of mean differences is inherently confounded. Second, time-domain variability affects frequency-domain variability; the total variance in time is equal to the total spectral power in frequency by Parseval's theorem. Third, different frequency ranges are not independent of one another (because of the presence of pink noise, which gives physiological variability its characteristic, inverse power-law spectrum). The interdependence of these parameters is important for scientific reporting and physiological interpretation. Where any frequency-domain parameter is reported, so, too, should all other frequency-domain indexes, time-domain indexes, and the parameter mean be reported.

Objectives of the Dissertation

I believe that the autonomic nervous system is important on a patient-by-patient, minute-to-minute basis in both health and disease, and thus, any contributions which advance our understanding of autonomic outflow, whether by elucidating the molecular mechanisms of autonomic regulation, validating widely used techniques for autonomic assessment, or developing new methods to assess autonomic outflow, are important. This thesis is made up of three distinct contributions to our understanding of autonomic outflow in which I played a key role, and this conviction is the common thread that ties them together.

Specifically, the objectives set forth in this dissertation are as follows:

1. To assess the functional role of Rho kinase in the autonomic effects of central AngII in conscious, chronically instrumented rabbits.
2. To investigate the correlation and agreement between measures of heart rate variability obtained by electrocardiography and pulse rate variability obtained by indwelling arterial pressure catheters as well as the autonomic basis for each signal.
3. To test the dogma that the sympathetic nervous system does not control renal blood flow except in disease.

These seemingly disparate objectives all target the overarching goal of quantitatively evaluating autonomic function as an integrated system and its coupling to circulatory regulation. Each objective will be presented in the following chapters with each study containing a brief introduction, detailed methods, results and brief discussion of major findings. A final discussion will follow, an overview of the major findings and implications of the dissertation.

Chapter I: Central Angiotensin-II Increases Blood Pressure and Sympathetic Outflow via Rho Kinase Activation in Conscious Rabbits

Introduction

Activation of the RAAS and sympatho-excitation are important maladaptive mechanisms in cardiovascular, renal, and metabolic disease[27–30]. In these chronic diseases, the RAAS and the sympathetic nervous system interact in a particularly deleterious, feedforward manner[15,31]. The primary effector peptide of the RAAS, AngII acts via the AngII type 1 receptor

in the brain to raise blood pressure, increase sympathetic outflow, and impair baroreflex function[32,33]. Recently, the intracellular mediators of AT1R signaling in both the periphery and the brain have garnered increasing interest[19,34,35]. Specifically, signaling in autonomic centers in the forebrain like the subfornical organ (SFO) and the paraventricular regions of the hypothalamus (PVH) is particularly important experimental models of AngII-induced hypertension and cardiovascular disease[36–40].

Many studies have shown that the RhoA/Rho kinase pathway is a crucial downstream effector of AT1R activation by AngII in the heart, endothelium, and vasculature[20,21,23]. RhoA/Rho kinase is particularly important in actin cytoskeleton assembly, calcium sensitization, and nitric oxide bioavailability[41,42]. Patients with diseases characterized by RAAS activation and autonomic dysfunction like hypertension and heart failure have elevated peripheral Rho kinase activity[24,43–45].

While logistical issues have prevented assaying central Rho kinase activity in patients, central Rho kinase activity is elevated in experimental models of hypertension and heart failure[44,46–49]. Moreover, central Rho kinase inhibition has beneficial autonomic effects in experimental models of cardiovascular disease[44,46,48–51]. Despite the importance of Rho kinase in peripheral AT1R signaling and central autonomic regulation, the interaction between the autonomic effects of central AngII and the Rho kinase pathway has never been directly tested. Therefore, in the present study, we hypothesized that AngII mediates its central effects by activation of the Rho kinase pathway, leading to baroreflex dysfunction, increased sympathetic tone, and hypertension.

Methods

Animals

Experiments were carried out on male New Zealand White rabbits ranging in weight from 3.1 to 4.5 kg (Charles River Laboratories, International, Wilmington, MA). All experiments were reviewed and approved by the University of Nebraska Medical Center Institutional Animal Care and Use Committee and carried out in accordance with the Guide for the Care and Use of Laboratory Animals of the National Institutes of Health. Rabbits were housed in individual cages in a temperature-controlled room (23º C) with a 12:12 hour light-dark cycle (lights on at 07:00, lights off at 19:00). Rabbits were given ad libitum access to reverse-osmosis purified water and high-fiber rabbit chow (Teklad 2031, Envigo RMS, Indianapolis, IN).

Within-subjects Cohort

To test the hypothesis that Rho kinase activation mediates the hemodynamic and autonomic effects of central AngII, six rabbits were instrumented with arterial pressure (AP) radiotelemetry transducers and intracerebroventricular (ICV) cannulae. Each rabbit received ICV infusions of AngII (40 ng/min; Sigma-Aldrich Corp., St. Louis, MO), AngII plus the Rho kinase inhibitor Fasudil (Fas, 175 ng/min; GeneDEPOT, Barker, TX), Fas alone, and artificial cerebrospinal fluid vehicle (Veh) via osmotic minipump in a randomized order. Mean arterial pressure (MAP) and HR were measured daily, and volume status32, cardiac parasympathetic tone33, cardiac sympathetic tone, global sympathetic vasomotor tone, and baroreflex function were assessed on days 10 through 14 of treatment by IV administration of FITC-sinistrin, autonomic blockers, or vasoactive drugs. This time period (days 10 through 14 of treatment) is referred to as the late phase of treatment. Between treatment infusions, rabbits received a 7-14 day washout with a Veh minipump.

Between-subjects Cohort

To test the hypothesis that Rho kinase activation mediates the renal sympatho-excitation caused by central AngII, rabbits were instrumented with radiotelemetry transducers, ICV cannulae, and renal sympathetic nerve electrodes. Seven days after renal nerve electrode surgery, resting RSNA and baroreflex control of RSNA were assessed. Not all chronic sympathetic nerve electrode implantations were successful (Figure 6), and rabbits without RSNA bursts one week after implantation were excluded from the study. Rabbits were subsequently euthanized and perfused with paraformaldehyde, and their brains were collected for molecular analysis.

Chronic Instrumentation

Each rabbit was chronically instrumented with an arterial pressure (AP) radiotelemetry and an ICV cannula connected to an osmotic minipump using sterile surgical technique. Following induction with an intramuscular bolus of ketamine (35 mg/kg) and xylazine (5.8 mg/kg), rabbits were intubated, and anesthesia was maintained with 1-2% isoflurane. After a femoral cut down, the tip of an AP telemetry catheter (model PA-C40, Data Sciences International, New Brighton, MN) was advanced into the abdominal aorta via the right femoral artery and secured. A scalp incision was made, the skull was cleared of connective tissue, and an ICV cannula was implanted 3 mm lateral to bregma. A periscapular incision was made, and a catheter was threaded subcutaneously from the scalp to the periscapular subcutaneous pocket. The cranial end of the catheter was connected to the ICV cannula, and the caudal end was connected to a vehicle-filled osmotic minipump (Alzet 2ML2, DURECT Corporation, Cupertino, CA). On the day of surgery, rabbits received pre-surgical enrofloxacin (22.7 mg subcutaneous, Bayer HealthCare LLC, Shawnee Mission, KS) and buprenorphine for pain control upon emergence from anesthesia. Rabbits received a three-day post-operative course of enrofloxacin and carprofen (4 mg/kg subcutaneous, Zoetis, Lincoln, NE) respectively. Each rabbit was allowed to recover for at least ten days, during which time the rabbit was acclimated to the procedure room and trained to rest calmly in a Plexiglas box. Rabbits in the between-subjects cohort underwent a subsequent surgery in which a bipolar

electrode was implanted on the left renal nerve. The left kidney was approached retroperitoneally via a flank incision, the largest renal nerve bundle was carefully dissected, and two platinum electrodes were wrapped around the dissected nerve section and fixed using Kwik-Sil adhesive (World Precision Instruments, Inc., Sarasota, FL). A ground loop electrode was secured to nearby tissue with 6-0 Prolene. Each electrode was electrically coupled to a Teflon-coated stainless steel wire, which was fixed to the renal artery with 6-0 Prolene, and all three leads were exteriorized via a common Silastic tube. The ICV vehicle infusion osmotic minipump was replaced with a treatment osmotic minipump, as described below, during the same surgery. Rabbits were given the same perioperative antibiotic regimen as above, but the analgesic regimen was supplemented with a 72-hour fentanyl patch (25 mcg/hr transdermal). Rabbits were allowed to recover seven days from RSNA surgery before experiments were begun.

Replacement of Osmotic Minipumps

Osmotic minipumps were replaced using sterile technique under general and local anesthesia with AP and heart rate (HR) monitoring. Rabbits were anesthetized with an intramuscular bolus of ketamine (17.5 mg/kg) and xylazine (2.9 mg/kg) and a local periscapular infiltration of bupivacaine (0.25 mg). An incision was made into the periscapular subcutaneous pocket containing the osmotic minipump to be replaced, and the pump was removed and the catheter connecting it to the ICV cannula was cut. A new osmotic minipump was connected to the catheter and implanted. The incision was closed with interrupted, external Prolene sutures. The content of the osmotic minipump was aspirated, and the aspirated volumes were always within 2 standard deviations of the manufacturer tolerances for pump volume and pump rate. When treatment pumps were placed, the function of the catheter and ICV cannula was first tested by giving a 100 nmol AngII bolus, which robustly raises MAP when given ICV but has no effect on if given subcutaneously (e.g., if the catheter is disconnected from the ICV cannula). Rabbits

received the same antibiotic regimen as for instrumentation and a one-time post-operative dose of buprenorphine (0.02 mg/kg subcutaneously) for pain control.

Dose-Finding Study

Three rabbits were used in a pilot study to identify doses of Angiotensin-II which raised blood pressure when administered ICV. Four ICV doses (10 ng/min, 20 ng/min, 30 ng/min, and 40 ng/min) were attempted, with only the highest showing a pressor effect. Three ICV doses (87.5 ng/min, 175 ng/min, and 350 ng/min) of Fas were co-infused with AngII. The two rabbits who initially received the lowest dose of Fas did not show any attenuation of the pressor effect of AngII. The rabbit who received the highest dose suffered acute neurological symptoms approximately 18 hours after implantation of the minipump and died quickly thereafter. It is unclear if this was related to central Rho kinase inhibition or an off-target mechanism. The 175 ng/min dose of Fas blocked the pressor effect of central AngII, but, clearly, the therapeutic window for central Fas to block the pressor effect of central AngII in rabbits is relatively narrow. The results for the two rabbits who completed the dose-finding study were used for power analysis.

Resting Recordings from Within-Subjects Study

The rabbits rested in a Plexiglas box in a dimly lit procedure room for at least 30 minutes at approximately the same time each morning. Pulsatile AP was digitized at a sampling frequency of 1 kHz via a 16-channel PowerLab system (ADInstruments, Inc., Colorado Springs, CO). Heart rate was derived from the pulse rate of the AP signal.

Pharmacological Assessment of Autonomic Tone

Intravenous (IV) administration of autonomic blockers in the afternoon of days 11 through 13 was used to assess the effects of ICV treatments on autonomic tone. After local infiltration with bupivacaine, an IV catheter was inserted into a marginal ear vein to allow IV administration of cardiac autonomic blockers. Each rabbit was allowed to rest for ten minutes after the placement of

the IV catheter, at which point a 1 mL bolus of saline was given and recording of pulsatile arterial pressure was initiated. Fifteen minutes later, atropine methyl bromide (0.2 mg/kg bolus; Sigma-Aldrich Corp., St. Louis, MO), metoprolol bitartrate (1 mg/kg bolus; Sigma-Aldrich Corp., St. Louis, MO), or hexamethonium bromide (3 mg/kg/min infusion for ten minutes; Sigma-Aldrich Corp., St. Louis, MO) was administered IV. Atropine, a muscarinic antagonist, blocks the effects of vagal control of sinoatrial node rhythmicity, and thus the increase in HR after atropine is a surrogate for resting cardiac parasympathetic tone. Metoprolol, a $beta_1$-adrenergic antagonist, blocks the effects of sympathetic control of sinoatrial node rhythmicity, and thus the decrease in HR after metoprolol administration is a surrogate for resting cardiac sympathetic tone. Hexamethonium, a ganglionic blocker, causes hypotension mainly by blocking sympathetic vasoconstrictor tone, and thus the maximal decrease in AP during the course of the hexamethonium infusion is a surrogate for global resting sympathetic vasomotor tone.

Assessment of Baroreflex Control of Heart Rate

On the afternoon of day 14, baroreflex control of HR was assessed by infusion of vasoactive drugs. After IV access was obtained as above, an IV infusion of sodium nitroprusside (100 µg/kg/min) was initiated and AP was driven down until HR reached a plateau. After the rabbit recovered completely, an infusion of phenylephrine (40 µg/kg/min) was initiated, and AP was driven up until HR reached a plateau. The HR and systolic blood pressure (SBP) for each beat were paired, and these pairs were then separated based on SBP into 2 mmHg wide bins. The median SBP and HR for each bin were fitted to a five-parameter logistic equation[52].

Volume Status Experiment

Four of the six rabbits underwent a volume status study on day 10 of ICV treatment using a previously described protocol in order to assess effects of the ICV treatment on volume regulation[53]. This was undertaken to because of the widely touted importance of renal sympathetic control of volume status in hypertension. This was a technique that we had not perfected when the

first two rabbits were enrolled, hence their exclusion. Briefly, the marginal ear vein and central ear artery of the conscious rabbit were catheterized after local lidocaine infiltration. A bolus of FITC-sinistrin (Fresenius Kabi, Linz, Austria) was given IV and quickly flushed. Blood samples (3 mL) from the arterial catheter were collected at 3, 7, 10, 15, 45, 75 and 105 minutes after the FITC-sinistrin bolus. The plasma fluorescence was measured and compared to a standard curve in order to derive the FITC-sinistrin plasma concentration. The FITC-sinistrin plasma concentration was fitted to a two-exponential decay equation, and the physiological parameters of the fitted open two-compartment pharmacokinetic model were derived. Specifically, glomerular filtration rate (GFR), the volumes of the high- and low-perfusion compartments ($V_{high\text{-}perfusion}$ and $V_{low\text{-}perfusion}$, respectively), and the first-order kinetic constants between the compartments $k_{high \rightarrow low}$ and $k_{low \rightarrow high}$ and out of the system k_{elim} (i.e. $GFR/V_{high\text{-}perfusion}$) are reported. The sum of the high- and low-perfusion compartments equals the extracellular fluid volume (ECFV).

Recording of RSNA

RSNA was differentially pre-amplified 10,000-fold, band-pass filtered from 100 to 1000 Hz (Grass P55, Natus Medical Inc., Warwick, RI), digitized at 1 kHz, rectified, and integrated with a 20-ms time constant. Resting RSNA was quantified as a percent of the nasopharyngeal reflex, burst frequency, and burst incidence. The nasopharyngeal reflex was elicited by drawing thick cigarette smoke into a 60-mL syringe and emptying the syringe into the face of the rabbit over 10 seconds. At the end of the experiment, the electrical zero (i.e. noise) was determined by administering a 30 mg/kg IV bolus of hexamethonium, which abolished RSNA. The resting integrated nerve activity minus the electrical zero was expressed as a percent of the maximal five-second integrated RSNA during elicitation of the nasopharyngeal reflex minus the electrical zero (i.e. [resting activity – electrical zero]/[nasopharyngeal maximum – electrical zero]x100%). Burst frequency was determined by manually setting a burst threshold above the noise floor of an artifact-free section of resting activity with a retrigger delay of 100 msec and expressed as bursts/min. Burst

incidence, the number of bursts per 100 heart beats, was determined by normalizing the burst frequency to the HR. Baroreflex control of RSNA was assessed just as performed as described above, except the rate of phenylephrine infusion was decreased from 40 μg/kg/min to 10 μg/kg/min. Beat-averaged integrated RSNA was paired with the preceding DBP, and these pairs were then separated based on DBP into 2 mmHg wide bins. The median DBP and integrated RSNA for each bin were fitted to a five-parameter logistic equation, but because baroreflex control of RSNA in the rabbit shows hypo- and hypertensive reversal[54], the lower plateau and the range of the logistic curve were fixed to match the DBP bins with the lowest and highest RSNA, respectively. Frequency-domain analysis was performed on RSNA. In brief, 5-minute artifact-free sections of data were linearly reinterpolated at 5.12 Hz, and the modified periodogram was computed via the Welch method using 50% overlapping, Hamming-tapered 60-second windows. VLF was considered 0-0.20 Hz, LF was considered 0.20 Hz to 0.45 Hz, and HF was considered 0.76 to 1.5 Hz, and the power in these frequencies is expressed as a percentage of the total power from 0-1.5 Hz. We hypothesized that greater sympathorespiratory coupling would result in elevated RSNA HF power in AngII-infused rabbits.

Assessment of Rho Kinase Activity

To validate that central AngII activates Rho kinase and that this activation is inhibited by Fasudil, Rho kinase activity was assessed using a LiCor Odyssey scanner to perform quantitative immunofluorescence[55] on sagittal brain slices with antibodies raised against the 696-threonine phosphorylated form of the Rho kinase target myosin phosphatase targeting protein (p-MYPT).

Rabbits were anti-coagulated with heparin (1000 international unit IV bolus), euthanized with 3 mL Fatal-Plus (Vortech Pharmaceuticals, Dearborn Michigan) IV bolus, and an intracardiac perfusion was performed with Tris-buffered saline (TBS) followed by 4% paraformaldehyde. The tissue was quickly removed and post-fixed for 36 hours in 4% paraformaldehyde and dehydrated in 3% sucrose prepared with TBS at 4°C. Next, a midline sagittal cut was made and one half of the

brain was blocked on an aluminum plate in Tissue Tek OCT Compound (Sakura Finetek, Torrance, CA) medium and stored at – 80°C until further processing. On the day of processing, brain tissue was acclimated to - 20°C and the tissue was sliced into 150 µm sections starting at the midline and placed in TBS.

Tissue slices were placed in TBS-based blocking buffer for 1 hour at room temperature with gentle shaking (LiCor, Lincoln, NE). Following this, the slices were exposed to a solution of 1:1000 p-MYPT mouse primary antibodies (sc-377531, Santa Cruz Biotechnology, Santa Cruz, CA) overnight at 4 °C with gentle shaking. The following morning, slices were rinsed with moderate shaking 4x for 15 minutes in 0.1% TBS-T. Slices were then exposed to a 1:10,000 dilution of donkey anti-mouse secondary antibody (925-68022, LiCor Bioscienes, Lincoln, NE) while protected from light with gentle shaking at room temperature. After incubation the tissues were rinsed with moderating shaking 4x for 15 minutes at room temperature, while protected from light. Slices were then placed into TBS until mounted. Tissues were removed from the TBS and mounted using a Versatool Kit (Elegant Instruments, Omaha, NE), placed on a glass slide, briefly rinsed in water and allowed to dry at room temperature protected from light for an allowed to completely dry before scanning.

All brains were scanned together at 42 µm resolution using a LiCor Odyssey Scanner. The resulting fluorescence image was then exported to MATLAB for image processing. The fluorescence intensity histogram was clearly bimodal, with the low-intensity background pixels composing one peak and the high-intensity brain tissue pixels composing another peak. The fluorescence intensity histogram was used to manually identify the maximum background intensity for the entire fluorescent image by selecting an intensity value that was between both peaks. Then, each brain slice was coarsely traced, and that region was then thresholded to exclude pixels whose intensity was below the maximum background intensity (indicating there was no brain, e.g., pixels in the third ventricle). This brain mask was then used to quantify the mean intensity (after subtracting the maximum background intensity) for each slice as well as for the quantification of

the mean p-MYPT fluorescence intensity in the SFO and PVH of each brain. Within each brain mask, the SFO was carefully traced, and the difference between the mean fluorescence intensity the maximum background intensity was used as the Rho kinase activity level. In a saggital slice, it is impossible to know the exact borders of the paraventricular hypothalamic nucleus (PVN), so we have adopted the nomenclature PVH in acquiescence of this fact. Uniformly sized and oriented boxes (see Figure 9) were placed in the PVH, and the mean p-MYPT fluorescence intensity above the background was used as an assessment of Rho kinase activity in the PVH.

Power Analysis and Sample Size Justification

The within-subjects cohort was powered to detect an AngII x Fas interaction on MAP via two-way ANOVA (Figure 1). Data from the dose-finding study were used for power analysis. The mean and standard deviation of MAP for each treatment were calculated and used to calculate the AngII x Fas and within-treatment sum-square error using a simple between-subjects two-way ANOVA approach, obviating known difficulties with multi-factor RM ANOVA power analysis[56]. This yields a more conservative estimate of sample size as the within-subjects design increases power. Since we did not have data for Fas alone infusion and had previously observed no effect on MAP from ICV Fas infusion (albeit a different dose) in healthy rabbits[46], the Veh mean and standard deviation were used for power analysis. The AngII x Fas and within-treatment sum of squares were used to calculate the effect size η^2, and GPower was used to compute the required sample size for $\beta > 0.80$. This showed that we needed 5 rabbits per treatment; we enrolled 6 rabbits due to the likelihood of instrumentation failure over the course of such a long study. All rabbits completed all four treatments.

The between-subjects cohort was powered to detect an AngII x Fas interaction on resting RSNA via two-way ANOVA using data from the literature (Figure 6). A study of 15 normal rabbits showed that RSNA when normalized to the nasopharyngeal reflex was 7.0% with a standard deviation of 4.6%[57]. Another previous study showed that a seven-day infusion of a non-pressor

dose of ICV AngII caused a 2.6-fold increase in resting RSNA normalized to the nasopharyngeal reflex with a similar increase in the standard deviation of resting RSNA, thus 18.4% was estimated as the mean and 12.0% the standard deviation for AngII-infused rabbits[58]. We assumed that Fas alone would not affect RSNA and that coadministration of Fas would completely block the AngII-mediated renal sympatho-excitation, mirroring what we had observed with global sympathetic vasomotor tone in the within-subjects study (i.e. $\mu_{Fas} = \mu_{AngII+Fas} = \mu_{Veh}$ and $\sigma_{Fas} = \sigma_{AngII+Fas} = \sigma_{Veh}$). This was used to compute an effect size η^2, and GPower was used to compute the required sample size for $\beta > 0.80$.

Statistical Analysis

Individual data are shown via dot plots with each dot representing one rabbit, and group data are displayed as group mean ± SEM. Statistical testing on endpoints from the within-subjects study was performed using two-way or three-way repeated measure (RM) analysis of variance (ANOVA) with $\alpha = 0.05$. Statistical testing on endpoints from the between-subjects study was performed using two-way ANOVA with $\alpha = 0.05$. The P values for the AngII, Fas, and AngII x Fas terms from the ANOVA are reported throughout the manuscript. Crucial to the central hypothesis of this manuscript, $P_{AngII \times Fas} < \alpha$ indicates that the response to AngII is significantly modified by Fas, i.e. that there is a non-additive interaction between AngII and Fas. This allows for statistical testing of the hypothesis that the effects of AngII are mediated by the Rho kinase pathway. In the absence of a significant interaction (i.e. $P_{AngII \times Fas} >> \alpha$), $P_{AngII} < \alpha$ indicates that AngII significantly affects the endpoint independent of Fas. This would be the expected result for a Rho kinase-independent effect of AngII. If the ANOVA reached statistical significance, it was followed by Bonferroni-corrected, paired t-tests of Veh versus AngII and AngII versus AngII+Fas ($\alpha = 0.025$). These t-tests were chosen as they most closely relate to the central hypothesis of the study while other t-tests (e.g., Veh vs. Fas) were foregone in order to decrease the effect of corrections for multiple comparisons on power.

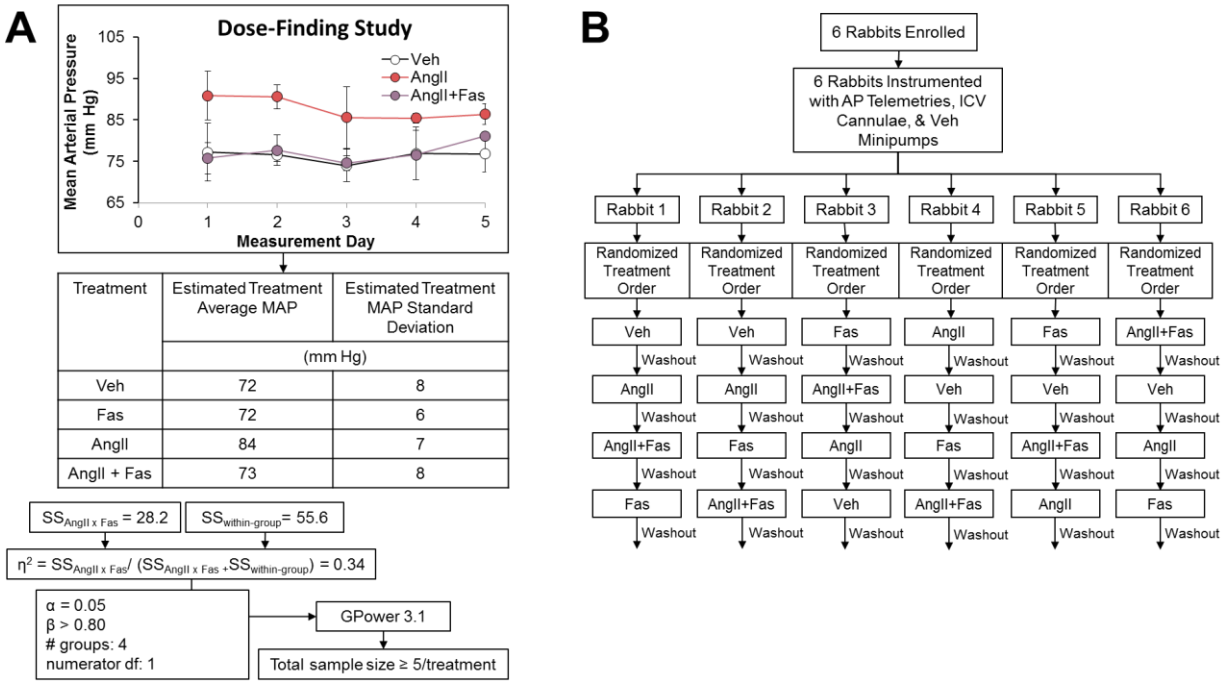

Figure 1 – Power Analysis and Flow Chart for the Within-Subjects Cohort.

(A) Power analysis for effect of ICV treatment on MAP observed in dose-finding study. (B) Each rabbit received all four ICV treatmments in random order.

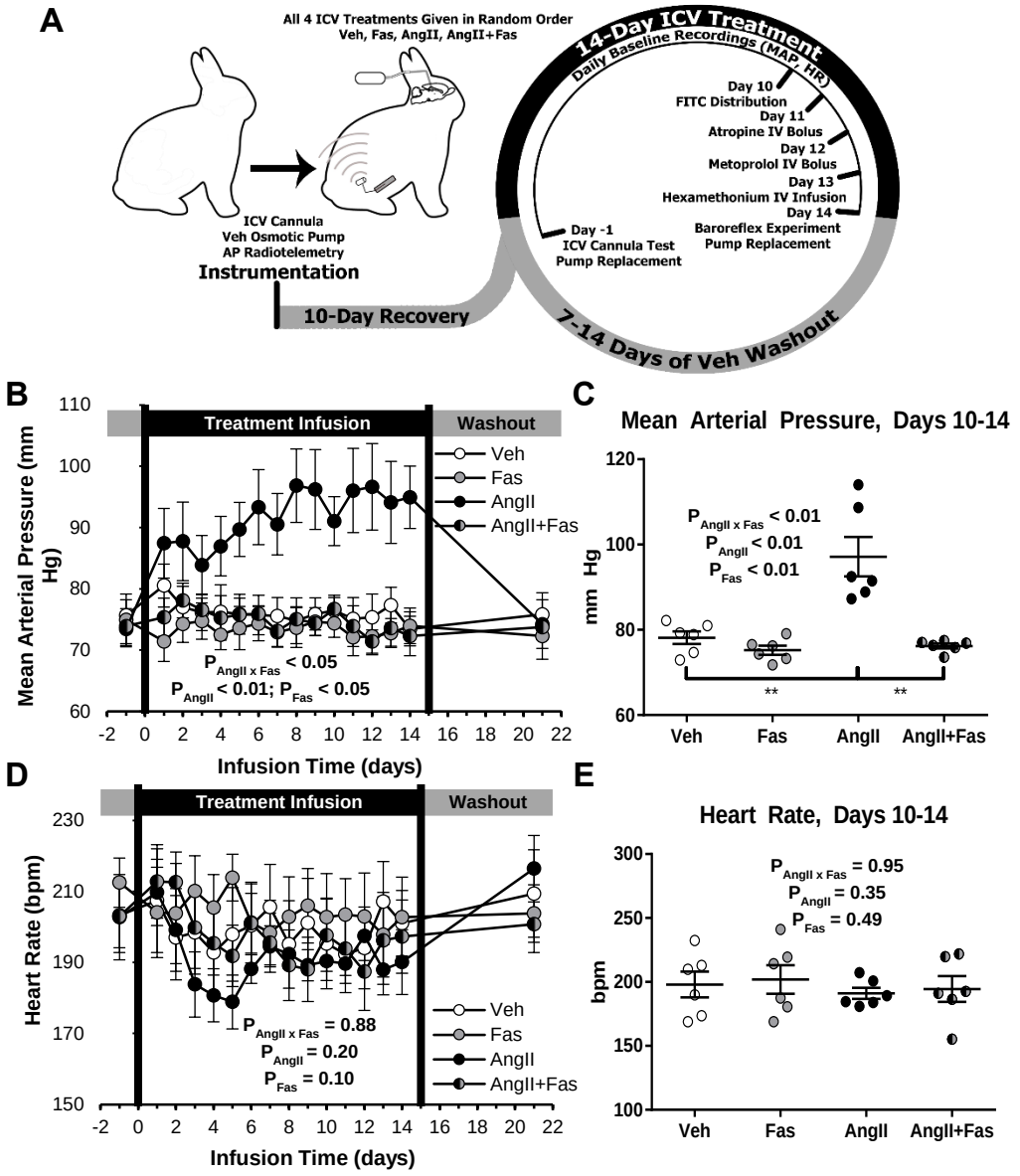

Figure 2 – Baseline Hemodynamics from the Within-subjects Cohort.

(A) Within-subjects study design illustrating basic experimental paradigm. (B) Average MAP over the course of each ICV treatment infusion and (C) the average MAP for each rabbit over days 10 through 14 of each ICV treatment. (D) Average HR over the course of each ICV treatment infusion and (E) the average HR for each rabbit over days 10 through 14 of each treatment infusion. *, $P < 0.025$; **, $P < 0.01$

Results

Resting Hemodynamics

We set out to evaluate the role of the Rho kinase pathway in the effect of AngII on basal hemodynamics by measuring MAP and HR daily over the course of ICV treatments. Power analysis and treatment order for this cohort can be found in Figure 1 while the experiment paradigm is shown in Figure 2A. Compared to Veh treatment, ICV infusion of AngII significantly increased MAP in all rabbits (Figure 2B and C), and this increase in MAP was abolished by co-administration of Fas. The statistically significant interaction between AngII and Fas indicates that ICV AngII-mediated increases MAP are dependent on Rho kinase activation. Conversely, none of the treatments had a significant effect on HR during the entire course of the infusion (Figure 2D) or in the late phase of infusion (Figure 2E).

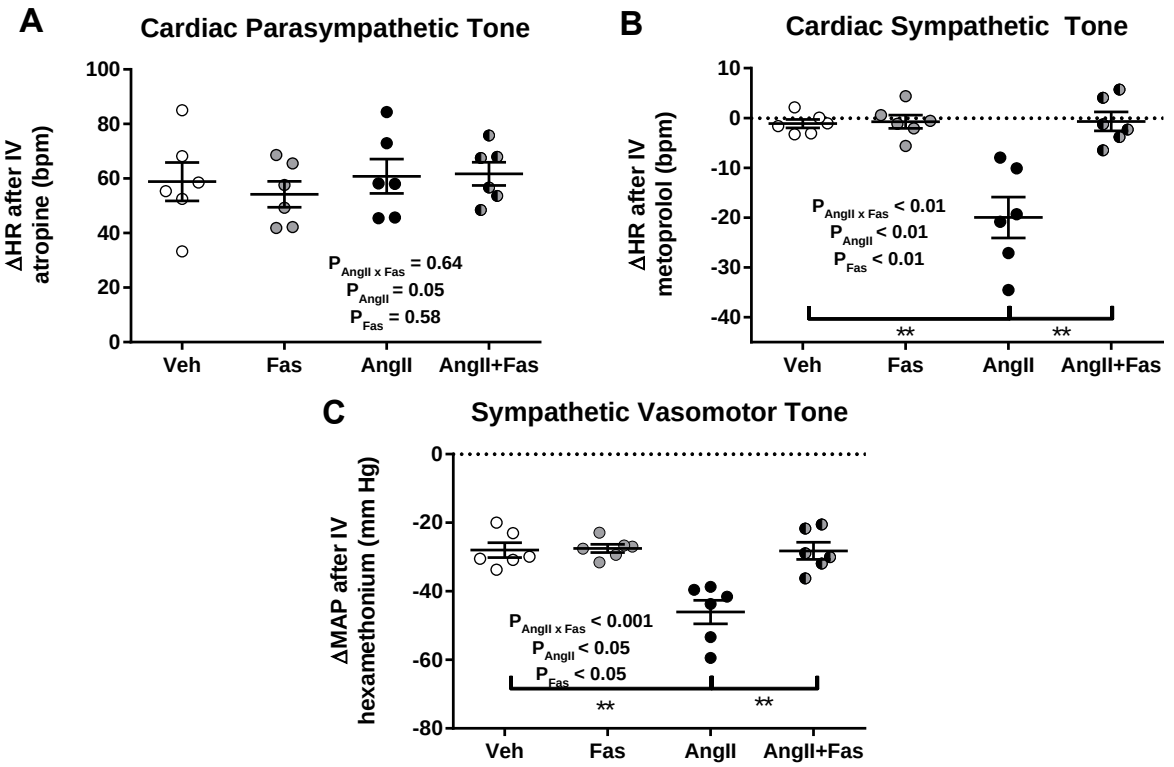

Figure 3 – Autonomic Blockade Experiments.

(A) Cardiac parasympathetic tone assessed by the HR response to atropine. (B) Cardiac sympathetic tone assessed by the HR response to metoprolol. (C) Global sympathetic vasomotor tone assessed by the MAP response to hexamethonium. *, P < 0.025; **, P < 0.01

Table 1 – Heart rate from atropine experiments

	Veh	Fas	AngII	AngII+Fas	$P_{AngII \times Veh}$	P_{AngII}	P_{Fas}
HR before atropine (bpm)	196 ± 10	205 ± 9	199 ± 5	197 ± 14	0.55	0.63	0.67
HR after atropine (bpm)	255 ± 17	259 ± 13	260 ± 10	259 ± 16	0.83	0.65	0.83

Table 2 – Heart rate from metoprolol experiments

	Veh	Fas	AngII	AngII+Fas	$P_{AngII \times Veh}$	P_{AngII}	P_{Fas}
HR before metoprolol (bpm)	204 ± 15	193 ± 13	205 ± 7	192 ± 15	0.88	0.94	0.06
HR after metoprolol (bpm)	203 ± 14	193 ± 12	185 ± 3	191 ± 14	0.41	0.29	0.66

Table 3 – Mean arterial pressure from hexamethonium experiments

	Veh	Fas	AngII	AngII+Fas	$P_{AngII \times Veh}$	P_{AngII}	P_{Fas}
MAP before hexamethonium (mm Hg)	82 ± 2	79 ± 2	101 ± 4	78 ± 2	< 0.05	< 0.05	< 0.01
MAP after hexamethonium (mm Hg)	53 ± 2	52 ± 2	55 ± 5	50 ± 2	0.56	0.96	0.23

Pharmacological Assessment of Autonomic Balance

Cardiac parasympathetic tone was assessed by the HR response to atropine. This was not significantly affected by any ICV treatment (Figure 3A, Table 1). Cardiac sympathetic tone assessed by the HR response to metoprolol was significantly increased by ICV infusion of AngII, and this cardiac sympatho-excitation was blocked by Fas co-administration (Figure 3B, Table 2). The statistically significant interaction between AngII and Fas indicates that the AngII-mediated cardiac sympatho-excitation depends on Rho kinase activation.

Global sympathetic vasomotor tone assessed by the MAP response to hexamethonium was significantly elevated by ICV infusion of AngII, and again co-administration of Fas blocked this elevation despite Fas alone having little effect (Figure 3C, Table 3). This interaction between AngII and Fas indicates that AngII elevates sympathetic vasomotor tone by Rho kinase activation.

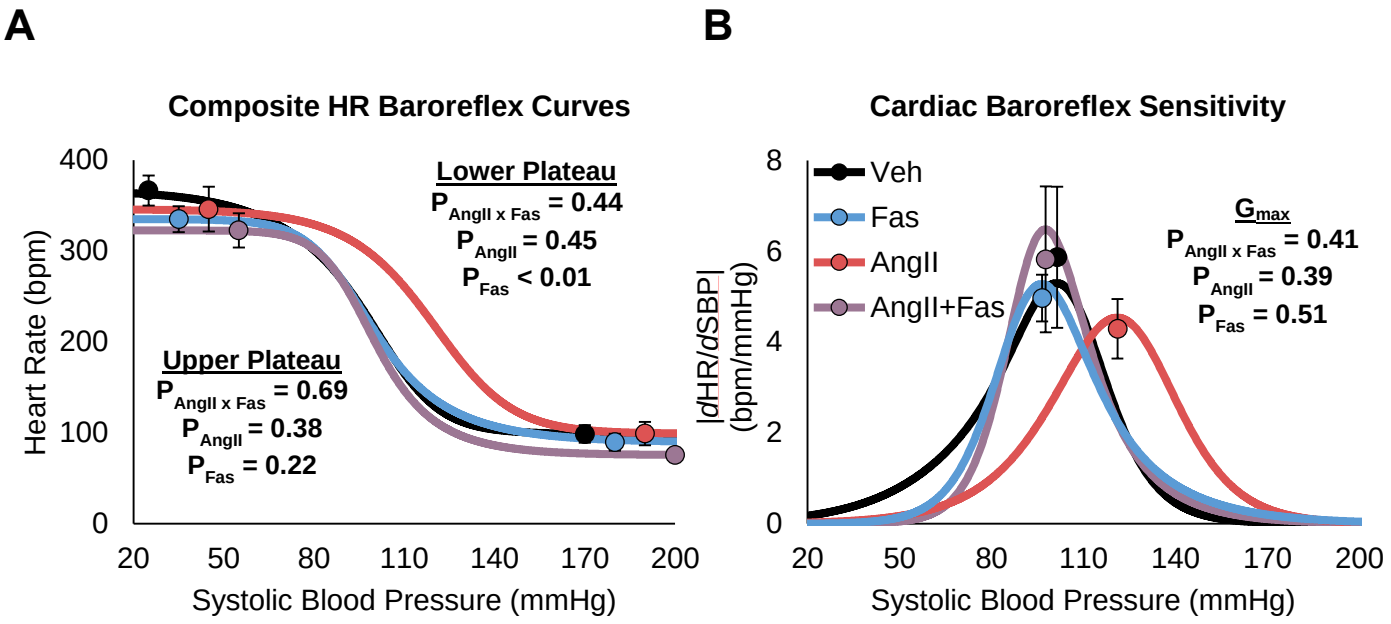

Figure 4 – Baroreflex Control of HR.

(A) Composite curves showing baroreflex control of HR for each treatment as well as the upper and lower plateaus of the 5-parameter logistic curves. (B) Composite baroreflex gain curves showing HR baroreflex sensitivity for each treatment as well as the average maximal gain for each treatment. G_{max}, maximal gain of 5-parameter logistic curve

Table 4 – Additional parameters from logistic equations of baroreflex control of HR

	Veh	Fas	AngII	AngII+Fas	$P_{AngII \times Veh}$	P_{AngII}	P_{Fas}
P2, Range (bpm)	268 ± 19	245 ± 17	267 ± 37	247 ± 23	0.27	0.54	0.63
P3, Lower Curvature	-0.06 ± 0.01	-0.11 ± 0.02	-0.10 ± 0.02	-0.14 ± 0.06	0.53	0.20	0.34
P5, Upper Curvature	-0.10 ± 0.04	-0.05 ± 0.01	-0.03 ± 0.01	-0.06 ± 0.01	0.13	0.10	0.71
P4, BP_{50} (mmHg)	97 ± 3	100 ± 4	119 ± 7	100 ± 5	0.09	< 0.05	0.07
Asymmetry	0.02 ± 0.51	0.74 ± 0.07	1.18 ± 0.27	0.61 ± 0.17	0.06	0.19	0.54
Curvature	0.05 ± 0.01	0.07 ± 0.01	0.04 ± 0.01	0.08 ± 0.02	0.10	0.97	0.09

P2, the range parameter; P3, the lower curvature parameter; P5, the upper curvature parameter; P4, the systolic blood pressure at which half of the range in heart rate was attained from the fitted 5-parameter logistic function, n = 6 for each treatment.

Assessment of baroreflex function with vasoactive drugs showed that ICV AngII caused a right-shift of the cardiac baroreflex curve in these rabbits without significantly affecting any other indexes of cardiac baroreflex function like gain or range (Figure 4 and Table 4). Fas decreased the lower HR plateau independent of AngII, consistent with Fas-mediated augmentation of maximal vagal outflow.

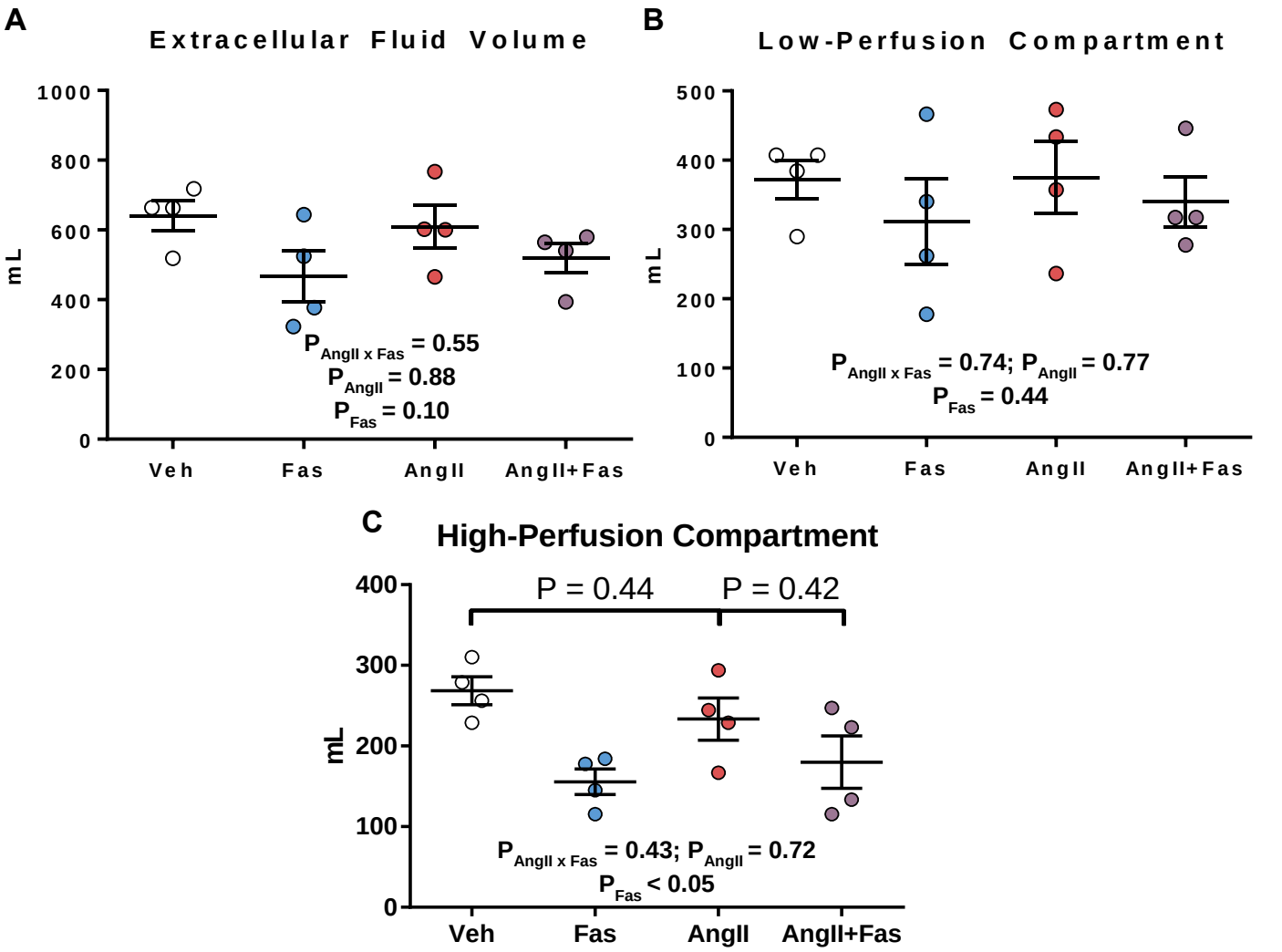

Figure 5 –Assessment of Volume Status by FITC-Sinistrin Distribution.

(A) Extracellular fluid volume. (B) Volume of the Low-Perfusion Compartment. (C) Volume of the High-Perfusion Compartment, n = 4 per treatment.

Table 5 – Additional Parameters from Two-compartment FITC-Sinistrin Pharmacokinetics

	Veh	Fas	AngII	AngII+Fas	$P_{AngII \times Veh}$	P_{AngII}	P_{Fas}
Glomerular Filtration Rate (mL/min)	11.2 ± 0.6	11.2 ± 1.7	12.1 ± 1.2	10.0 ± 1.0	0.50	0.93	0.13
k_{elim} (min^{-1})	0.042 ± 0.002	0.073 ± 0.011	0.055 ± 0.012	0.060 ± 0.010	0.18	0.97	0.23
$k_{high \rightarrow low}$ (min^{-1})	0.079 ± 0.008	0.143 ± 0.033	0.138 ± 0.057	0.160 ± 0.039	0.09	< 0.05	0.07
$k_{low \rightarrow high}$ (min^{-1})	0.057 ± 0.004	0.076 ± 0.016	0.074 ± 0.017	0.075 ± 0.17	0.53	0.36	0.60

k_{elim}, plasma elimination kinetic constant; $k_{high \rightarrow low,}$ kinetic constant for flux from high-perfusion to low-perfusion compartment, $k_{low \rightarrow high}$, kinetic constant for flux from low-perfusion to low-perfusion compartment, n = 4 for each treatment

Assessments of volume homeostasis showed that, despite increases in MAP, extracellular fluid volume was not decreased in rabbits receiving ICV AngII, nor did AngII affect other two-compartment model parameters (Figure 5 and Table 5).

A

Group	Estimated Group Mean RSNA	Estimated Group Standard Deviation of RSNA
	(% nasopharyngeal reflex)	
Veh	7.0	4.6
Fas	18.4	12.0
AngII	7.0	4.6
AngII + Fas	7.0	4.6

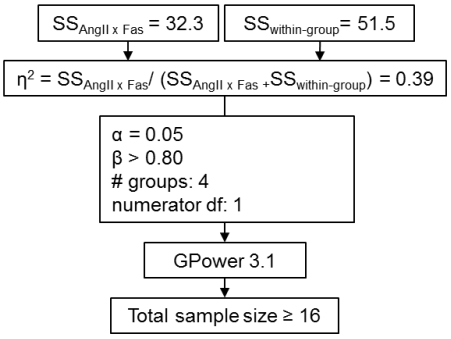

B

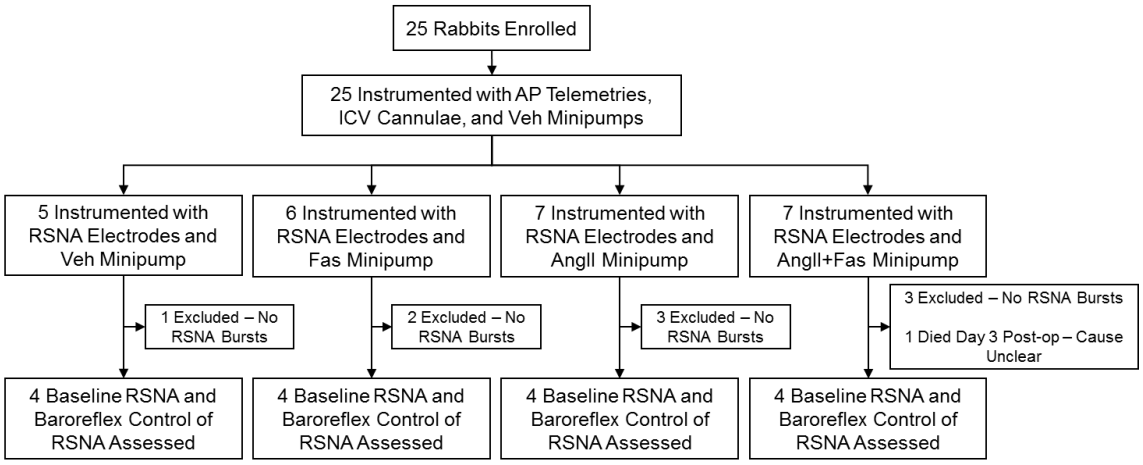

Figure 6 – Power Analysis and Flow Chart for Between-subjects Cohort.

Study Design and Flow Chart for the Between-Subjects Cohort. (A) Power analysis for baseline RSNA based on literature values. (B) Each rabbit received one ICV treatment, rabbits without RSNA bursts after a one-week recovery from RSNA surgery were excluded from analysis.

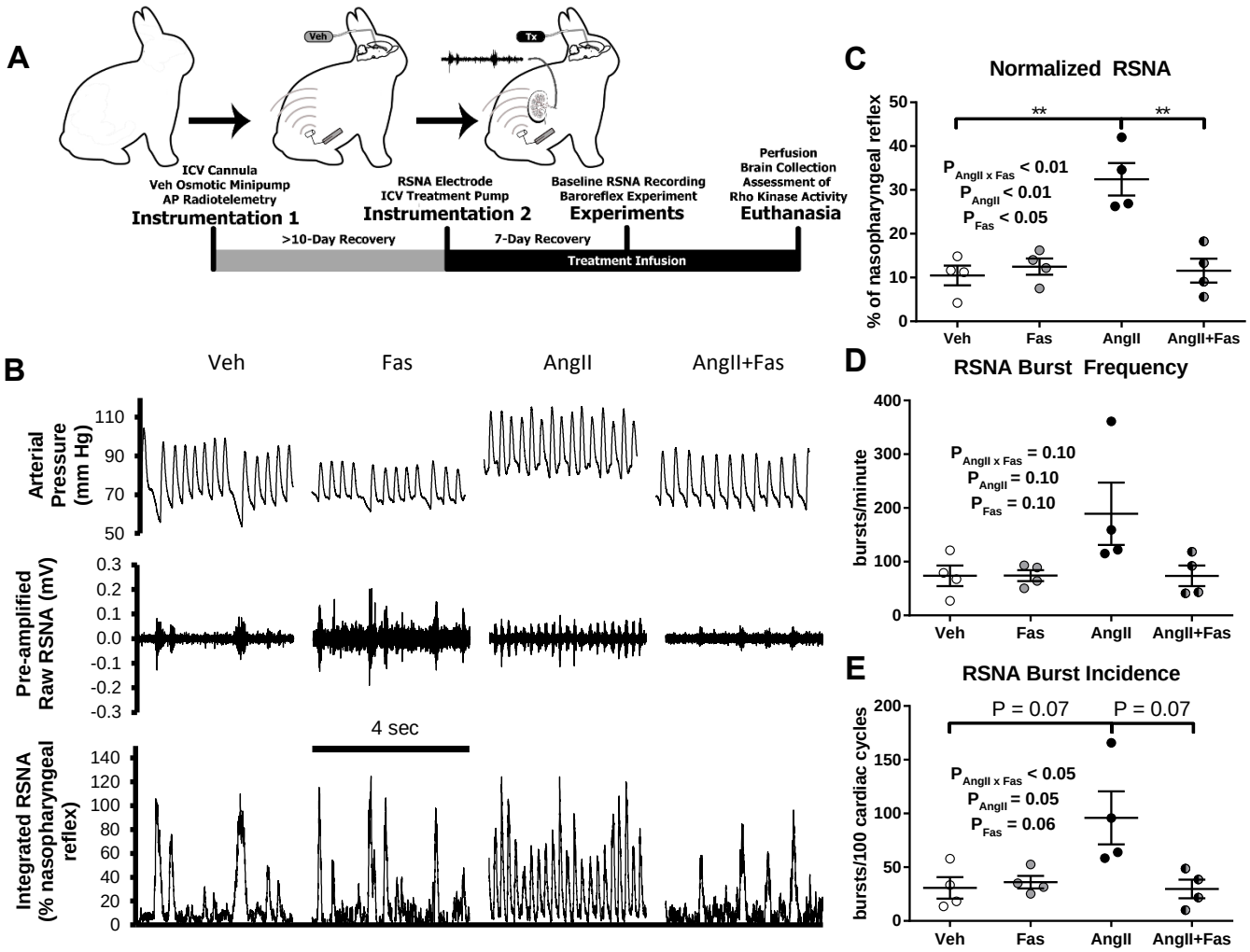

Figure 7 – Resting RSNA from Between-subjects Cohort.

(A) Between-subjects cohort study design illustrating basic experimental paradigm. (B) Representative tracings of pulsatile arterial pressure, raw RSNA, and integrated RSNA for one rabbit receiving each ICV treatment. (C) RSNA normalized to the nasopharyngeal reflex. (D) Baseline RSNA quantified as burst frequency. (E) Baseline RSNA quantified as burst incidence. **, $P < 0.01$

Table 6 – Resting Hemodynamics for Between-subjects Study

	Veh	Fas	AngII	AngII+Fas	$P_{AngII \times Veh}$	P_{AngII}	P_{Fas}
MAP (mm Hg)	75 ± 3	78 ± 2	91 ± 4*	74 ± 3†	< 0.01	0.05	0.08
HR (bpm)	203 ± 5	205 ± 6	197 ± 10	205 ± 12	0.70	0.71	0.54

Resting mean arterial pressure (MAP) and heart rate (HR) 7 days after RSNA electrode implantation. *, $P < 0.025$ vs AngII; †, $P < 0.025$ vs. AngII+Fas, n = 4 for each treatment.

Table 7 – RSNA Spectral Distribution

	Veh	Fas	AngII	AngII+Fas	$P_{AngII \times Veh}$	P_{AngII}	P_{Fas}
VLF (% total)	14 ± 3	11 ± 6	20 ± 5	16 ± 3	0.26	0.35	0.41
LF (% total)	22 ± 5	27 ± 6	19 ± 4	18 ± 5	0.11	0.31	0.32
HF (% total)	33 ± 5	32 ± 7	45 ± 9	38 ±7	0.81	0.10	0.63

RSNA spectral distribution 7 days after RSNA electrode implantation. n = 4 for each treatment. VLF, very low-frequency power (0-0.20 Hz); LF, low-frequency (0.20-0.46 Hz); HF = high-frequency (0.76-1.5 Hz); % total, percentage of power from 0-1.5 Hz

Resting RSNA

We set out to directly measure RSNA in conscious rabbits using. The power analysis and flow diagram for this cohort is shown in Figure 6, and the experimental paradigm is shown in Figure 7. Resting hemodynamics are shown in Table 6; notably, AngII-treated rabbits in this cohort were hypertensive while HR did not significantly differ between treatment groups.

Rabbits receiving ICV AngII had significantly increased baseline RSNA when quantified as a percent of the nasopharyngeal reflex (Figure 7B and C) and tended to exhibit increased RSNA burst frequency and burst incidence (Figure 7D and E). Again, Fas alone had little effect, and the statistically significant interaction between AngII and Fas with regard to normalized RSNA and RSNA burst incidence indicates that AngII-mediated renal sympatho-excitation depends on Rho kinase activation. Despite this difference in burst frequency, the spectral distribution of RSNA was not significantly affected by any ICV treatment although there was a trend for AngII treatment to increase RSNA HF power (Table 7).

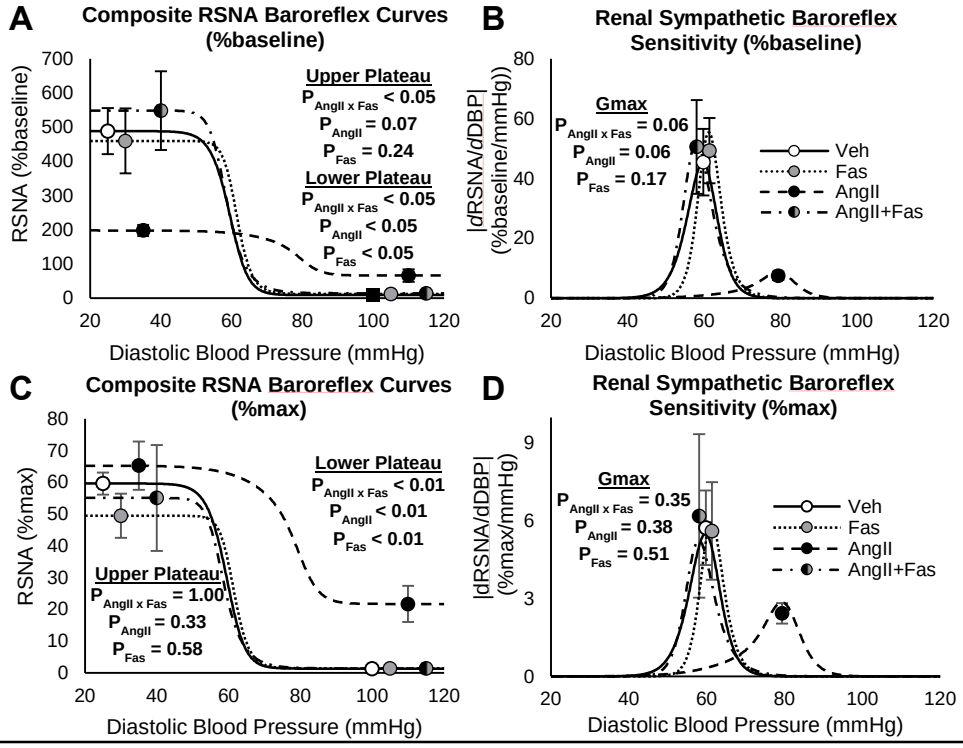

Figure 8 –Baroreflex Control of RSNA

(A) Composite RSNA baroreflex curves normalized to baseline RSNA. (B) Composite RSNA baroreflex gain curves normalized to baseline RSNA. (C) Composite RSNA baroreflex curves normalized to the nasopharyngeal reflex. (D) Composite RSNA baroreflex gain curves normalized to the nasopharyngeal reflex.

Table 8 – Additional parameters from logistic equations of baroreflex control of RSNA

	Veh	Fas	AngII	AngII+Fas	$P_{AngII \times Veh}$	P_{AngII}	P_{Fas}
P2, Range (%baseline)	479 ± 72	447 ± 93	132 ± 27*	533 ± 111†	< 0.05	< 0.05	0.14
P2, Range (%max)	58.3 ± 4.1	48.0 ± 7.0	43.5 ± 9.5	53.7 ± 16.4	0.34	1.00	0.67
P3, Lower Curvature	-0.35 ± 0.20	-0.56 ± 0.14	-0.15 ± 0.08	-0.56 ± 0.11	0.33	0.09	0.34
P5, Upper Curvature	-0.40 ± 0.23	-0.43 ± 0.23	-0.34 ± 0.17	-0.21 ± 0.08	0.69	0.79	0.46
P4, BP_{50} (mmHg)	56.4 ± 2.6	61.5 ± 3.2	77.6 ± 5.3*	58.7 ± 1.5†	< 0.05	0.05	< 0.05
Asymmetry	0.24 ± 0.46	0.50 ± 0.58	-0.70 ± 0.88	1.08 ± 0.31	0.22	0.11	0.77
Curvature	0.30 ± 0.06	0.34 ± 0.10	0.11 ± 0.08	0.29 ± 0.11	0.45	0.22	0.20

P2, the range parameter; P3, the lower curvature parameter; P5, the upper curvature parameter; P4, the systolic blood pressure at which half of the range in RSNA was attained from the fitted 5-parameter logistic function. *, $P < 0.025$ vs. Veh, †, $P < 0.025$ vs. AngII.

Baroreflex Control of Renal Sympathetic Nerve Activity

ICV AngII impaired baroreflex control of RSNA compared to Veh treatment, and Fas co-administration prevented this baroreflex dysfunction (Figure 8 and Table 8). When RSNA was expressed relative to basal RSNA, rabbits receiving AngII showed decreased RSNA baroreflex range, with the upper plateau significantly lower ($P < 0.025$ vs. Veh) and the lower plateau significantly higher ($P < 0.025$ vs. Veh). These effects depended on Rho kinase activation ($P_{AngII \times Fas} < 0.05$). Similarly, AngII treatment lowered baroreflex gain when expressed as a percentage of basal RSNA ($P < 0.025$ vs. Veh) only in the absence of Fas coadministration.

We also analyzed baroreflex curves with RSNA normalized to the nasopharyngeal reflex to account for the aforementioned differences in baseline RSNA (Figure 8C and D). When RSNA was normalized in this manner, the gain and the range of the RSNA baroreflex curves tended to be decreased by AngII infusion, but these trends did not reach statistical significance, indicating that these effects are at least partially related to the differences in basal RSNA. Even after normalization to the nasopharyngeal reflex, the lower plateau was significantly higher in AngII-infused rabbits compared to the Veh group ($P < 0.025$), and this increase depended on Rho kinase activation ($P_{AngII \times Fas} < 0.01$). Thus, central AngII acts via Rho kinase activation to cause deficits in the capacity for baroreflex-induced sympatho-inhibition regardless of how RSNA was normalized.

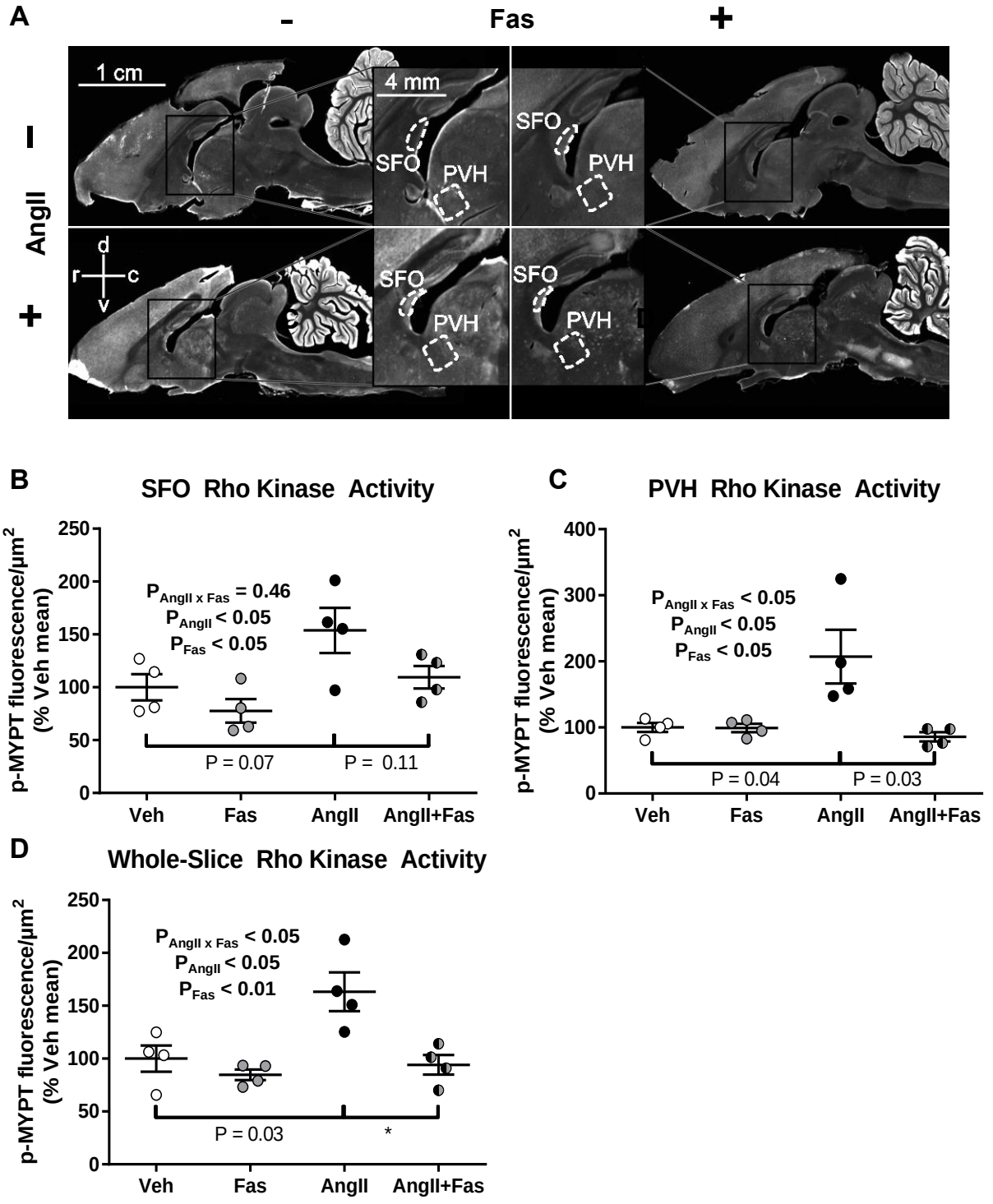

Figure 9 – Assessment of Rho Kinase Activity

(A) Representative saggital brain slices stained with antibodies for the Rho kinase target p-MYPT from rabbits infused with each ICV treatment. (B) Mean SFO p-MYPT fluorescence. (C) Mean PVH p-MYPT fluorescence. (D) Mean whole-slice p-MYPT fluorescence.
d, dorsal direction; v, ventral direction; r, rostral direction; c, caudal direction; *, $P < 0.025$.

Assessment of Rho Kinase Activity

Rho kinase phosphorylates MYPT in the brain[59], and this phosphorylation was used as a marker for Rho kinase activity. AngII treatment increased Rho kinase activity in the SFO, PVH, as well as the entire slice (Figure 9). Interestingly, in the SFO, AngII treatment increased Rho kinase in a Fas-independent manner, and Fas decreased Rho kinase activity in an AngII-independent manner, whereas in the PVH and diffusely, AngII and Fas showed a statistically significant interaction.

Discussion

In the present study we show that central infusion of AngII increases blood pressure, elevates sympathetic outflow, and blunts baroreflex function by downstream activation of Rho kinase. This study builds upon a previous study from our laboratory performed in the rabbit pacing model of chronic heart failure which showed that central infusion of Fas improved baroreflex function and cardiac autonomic balance in the setting of heart failure[46]. These data are also consistent with other studies in hypertensive rat models which have described central activation of Rho kinase and shown benefits from central Rho kinase inhibition[48–51]. Ito et al. showed that transfection of the nucleus tractus solitarius (NTS) of both spontaneously hypertensive and Wistar-Kyoto rats with a dominant-negative Rho kinase results in decreases in MAP, HR, and urinary norepinephrine excretion[48]. These effects were greater in the spontaneously hypertensive rats, which also had greater Rho kinase activity in the NTS compared to Wistar-Kyoto control rats. Our study also corroborates one of these studies, which found that subchronic central administration of the Rho kinase inhibitor Y27632 prevented the pressor effect of central AngII in Sprague-Dawley rats[51]. This rat study did not include rats receiving the Rho kinase inhibitor alone and thus was unable to address the central hypothesis of the current study, nor were direct measurements of sympathetic nerve activity or baroreflex function performed.

Baroreflex function, sympathetic outflow, and AP interact in complex ways which merit further discussion. Studies of baroreceptor unloading and stimulation implicate the baroreflex as an important controller of chronic sympathetic outflow and arterial pressure[60–66]. This gives weight to the possibility that Rho kinase activation mediates sympathetic baroreflex dysfunction which underlies the sympatho-excitation and hypertension caused by central AngII. In particular, elevated RSNA is crucial to the development of hypertension because of its ability to impair the powerful homeostatic mechanism of pressure-natriuresis[67–69]. In the within-subjects cohort, neither extracellular fluid volume nor the high-perfusion compartment volume, which is a surrogate for intravascular blood volume, were decreased by AngII treatment despite a 19 mmHg increase in AP, implicating a deficit in pressure-natriuresis with central AngII. This departure from expected pressure-mediated volume regulation corroborates the idea that elevated RSNA facilitates chronic elevations in AP during central AngII.

Because of the inherent difficulties in the normalization of RSNA, it is unclear whether the reported sympathetic baroreflex dysfunction in AngII-treated rabbits leads to elevated RSNA or if it is the increased RSNA which causes the sympathetic baroreflex to appear perturbed. Clearly, normalizing the RSNA baroreflex by the nasopharyngeal reflex instead of the baseline RSNA greatly attenuates the AngII-mediated decrease in sympathetic baroreflex sensitivity and range. But any further interpretation is prone to a classic chicken-and-egg dilemma as it is just as reasonable that the AngII-mediated baroreflex dysfunction underlies the observed increases in RSNA as it is that the AngII-mediated increase in baseline RSNA results in apparent baroreflex dysfunction. Regardless of how RSNA is quantified, AngII causes a deficit in the maximal pressor-mediated sympathoinhibition, perhaps indicating that baroreflex dysfunction is the primary disturbance. Of course, elevations in AP *per se* affect baroreflex function[70,71], further complicating the process of parsing cause from effect in this truly integrative system.

The activity of Rho kinase in the brains of these rabbits showed interesting differential patterns. In the SFO, which is a primary sensor and essential mediator of the effects of central and

peripheral AngII[34,72], AngII and Fas significantly affected Rho kinase activity independently, with no evidence for interaction ($P_{AngII \times Fas} = 0.46$). Conversely, in the PVH, which is an important preautonomic integration center, and in the whole saggital slice, AngII and Fas interacted in their effect on Rho kinase activity. The additive nature of the effects of AngII and Fas on Rho kinase activity in the SFO may indicate that both are acting at this site, with AngII activating RhoA via AT1R signaling while Fas directly inhibits Rho kinase. In the absence of Fas, AngII increases Rho kinase activity and drives downstream activation of the PVH and global sympatho-excitation[37]; when both AngII and Fas are present, Rho kinase activity in the SFO is relatively normal and these untoward downstream effects are blocked.

While solid evidence indicates that central AngII stimulates Rho kinase via AT1R activation[51], the intermediaries between AT1R and RhoA/Rho kinase in the brain remain to be elucidated. In the periphery, AT1R signaling stimulates the RhoGEFs Arhgef1[23] and p63RhoGEF[24], which activate RhoA/Rho kinase, and inhibits the RhoGAP p190A[25] which, in turn, inhibits RhoA/Rho kinase. It is likely that these same mediators are important in the transduction between AT1R and RhoA in the brain, but other factors may play an important role and this area merits further study.

The downstream molecular mechanisms by which Rho kinase mediates its effects are likely multiple. Rho kinase is a crucial part of feedforward AngII-mediated oxidative signaling in the endothelium and may play a similar role in sympatho-excitatory superoxide signaling in the preautonomic centers of the brain[21,36]. Closely intertwined is the effect of Rho kinase to decrease the production of sympatho-inhibitory nitric oxide, which rapidly reacts with superoxide[73]. These free radicals affect neuronal excitability by altering K^+ and Ca^{2+} currents[34,74]. Additionally, Rho kinase is known to play a fundamental role in neurotransmitter release and dendritic spine formation[48], and thus Rho kinase inhibition might prevent the release of sympatho-excitatory neurotransmitters and impair neuroplastic conversion to a sympatho-excitatory phenotype.

The two Rho kinase isoforms (ROCK1 and ROCK2) share approximately 90% homology in their kinase domains but despite this structural similarity, they are differentially distributed and perform distinct functions[75]. Of note, ROCK1 in the hypothalamus has been shown to play an important role in metabolic regulation, which is closely related to sympathetic outflow[76]. ROCK2 is more highly expressed in the brain, and induction of heart failure in rabbits by rapid ventricular pacing increases ROCK2 levels in the rostral ventrolateral medulla, an important brainstem autonomic center[46]. Fasudil inhibits both isoforms with approximately equal affinity[77], and thus this study is unable to address the contributions of each isoform to AngII-mediated sympatho-excitation.

At present, Fas is used clinically in Japan after acute ischemic stroke and for the prevention of vasospasm after surgery for subarachnoid hemorrhage[78,79]. Another Rho kinase inhibitor, ripasudil, is also approved in Japan for the treatment of glaucoma and ocular hypertension[80]. Other clinical trials have investigated or are currently investigating Rho kinase inhibitor therapy in psoriasis, diabetic retinopathy, pulmonary arterial hypertension, erectile dysfunction, amyotrophic lateral sclerosis, spinal cord injury, atherosclerosis, and chronic kidney disease[75].

While the clinical use of specific Rho kinase inhibitors is limited, over 30 million Americans take statins for their cholesterol- and cardiovascular risk-reducing effects. Statins inhibit HMG-CoA reductase, which is crucial in the synthesis of not only cholesterol but also isoprenoid intermediates. Post-translational isoprenylation of RhoA is necessary for RhoA trafficking and activation[81], and thus, statins not only lower cholesterol but also reduce RhoA/Rho kinase activity. Indeed, therapeutic doses of statins decrease Rho kinase activity in patients with atherosclerosis in an LDL-independent manner[82]. Our lab has similarly found that statin treatment improves autonomic function in experimental and clinical heart failure independent of LDL-lowering effects[83–87], and clinical studies in patients with hypertension and chronic kidney disease support the sympatholytic effect of statins in humans regardless of the presence of hyperlipidemia[88–91]. Given the strong associative[92–94] and experimental[95,96] data linking autonomic function and

mortality in cardiovascular disease, the sympatholytic effects of statins through Rho kinase inhibition may be an important mechanism by which these drugs reduce cardiovascular risk.

We acknowledge that the present study has several limitations. First, it is unclear if the dose of AngII falls within the limits of pathophysiology or if this is a strictly pharmacological dose. Similarly, we do not know if brain tissue levels of Fas are achievable by systemic administration of Fas in humans. Moreover, treatments were administered ICV and thus the exact location of their action in the brain cannot be truly known, although it is likely that concentrations of all agents would be higher near structures close to the ventricular system (e.g. SFO). Finally, the precise mechanisms by which Rho kinase is activated by AngII and the downstream mechanisms by which Rho kinase induces sympatho-excitation remain to be elucidated.

Activation of the RAAS and autonomic dysfunction are pathophysiological hallmarks of cardiovascular disease. The present study shows that the pro-hypertensive, sympatho-excitatory, and baroreflex-perturbing effects of AngII in the brain are mediated by the Rho kinase activation. These data indicate that inhibition of the central Rho kinase pathway may act as a therapeutic brake on the positive feedback between central RAAS activation and sympathetic outflow in many diseases characterized by sympatho-excitation.

Chapter II: Validation of Pulse Rate Variability as a Surrogate for Heart Rate Variability in Chronically Instrumented Rabbits

Introduction

Heart rate variability (HRV) is a function of cardiac autonomic balance that is predictive of mortality in conditions ranging from chronic heart failure to traumatic injury[97,98]. While clinical standards dictate that heart rate variability must be computed from an electrocardiogram (ECG) signal[99], dozens of human studies have investigated the acceptability of pulse wave recording, by photoplethysmography as a surrogate for heart rate variability in various physiological and disease states[100]. The differences between HRV indices obtained by these two methods have led some authors to conclude that pulse wave monitoring does not provide an acceptable signal for HRV analysis[101].

Because of its prognostic value and widespread use in clinical literature, measures of HRV have become prevalent in animal studies, which lack the unified guidelines like those established for humans. Frequently, so-called HRV analysis in animals is performed on data derived not from an ECG signal but from the arterial pulse waveform obtained by a radiotelemetry implanted into a main artery[102–104]. This is a much different pulse wave monitoring technique than has been investigated in clinical studies, and it is thus important to understand how well measures of pulse rate variability (PRV) obtained via chronically implanted radiotelemetry agree with measures of heart rate variability (HRV) obtained via ECG. The acceptability of PRV as a surrogate for HRV has never been systematically investigated in animals.

Measures of HRV are stratified into three categories: time-domain, frequency-domain, and non-linear statistics. The standard deviation of normal-to-normal intervals (SDNN) is the most widely used time domain measure and has powerful predictive value in many diseases[97,105] In the frequency domain, the low-frequency (LF) band comprises both sympathetic and parasympathetic oscillations while the high-frequency (HF) band is specifically modulated by parasympathetic outflow. The low-frequency to high-frequency ratio (LF/HF), while somewhat controversial[106], remains widely used as an index of cardiac sympathovagal balance[99]. Non-linear measures

encompass a heterogeneous group of statistics, several of which quantify the entropy or complexity of the signal. Multiscale sample entropy is one such statistic which has been used to distinguish patients with cardiovascular pathologies from healthy subjects[107–109] and is predictive of mortality in trauma and heart failure patients[110–113].

In the present study, we investigated the use of PRV as a surrogate for HRV using rabbits chronically instrumented with both intracardiac leads and arterial pressure radiotelemeters. We report the correlation and agreement of time domain, frequency domain, and non-linear measures of HRV and PRV in the resting state. We also report the effect on PRV when HRV is driven to zero by ventricular pacing. Finally, since many studies use HRV measures as an index of cardiac autonomic status, it was important to examine the autonomic underpinnings of these two signals. By performing cardiac autonomic blockade experiments with atropine and metoprolol, we examined the effects of cardiac autonomic blockade on PRV and HRV.

Materials and Methods

Animals

Experiments were carried out on male New Zealand White rabbits ranging in weight from 3.3 - 4.2 kg (Charles River Laboratories, International, Wilmington, MA). All experiments were reviewed and approved by the University of Nebraska Medical Center Institutional Animal Care and Use Committee.

Surgical Instrumentation

All rabbits were instrumented with an implantable radiotelemeter and epicardial pacing leads as previously described [114]. In brief, the tip of the telemetry catheter (model PA-C40, Data Sciences International, New Brighton, MN) was advanced into the abdominal aorta via the right femoral artery and secured, allowing chronic recording of pulsatile arterial pressure and providing the signal for PRV analysis. As part of the same surgery, a left thoracotomy was performed and a

platinum wire pacing electrode was placed on the left ventricle of the heart and a ground wire was secured to the left atrial appendage. The wires were tunneled beneath the skin and exited in the mid-scapular region, providing the ECG signal for HRV analysis. The chest was evacuated, and the thoracotomy was closed in layers. The rabbits were allowed to recover for at least two weeks before any experiments were conducted. During this time, the animals were acclimatized to the procedure room.

Baseline Recordings

To investigate the correlation and agreement of HRV and PRV measures in chronically instrumented animals, baseline measurements were conducted on eight rabbits. The rabbits rested in a plexiglass box in the dimly lit procedure room for at least 20 minutes. Pulsatile arterial pressure, calibrated by a Dataquest A.R.T. analog system (Data Sciences International, New Brighton, MN), and ECG were simultaneously digitized at a sampling frequency of 1 kHz via a 16-channel PowerLab system (ADInstruments, Inc., Colorado Springs, CO). Each rabbit was recorded on four separate days; however, due to an issue with the pressure telemeter in one animal, only 30 total recordings were analyzed. Five-minute, artifact-free sections of the recording were used for HRV and PRV analysis.

Ventricular Pacing

Ventricular pacing experiments were conducted on eight rabbits to examine PRV when HRV was driven to zero. For these experiments, the left chest, right chest, and right haunch of each rabbit were shaved, and ECG electrodes (TenderTrace Pediatric ECG electrodes, New Dimensions in Medicine, Dayton, Ohio) were applied to the shaved areas with conductive gel. This signal was differentially amplified to yield the skin ECG signal, and both the skin ECG signal and pulsatile arterial pressure were recorded for at least fifteen minutes. After this baseline recording, a pulse generator was connected to the rabbit's pacing leads and the heart rate was increased to 250 beats per minute, a rate higher than the maximum baseline heart rate, and held at this rate for ten to

fifteen minutes. Five-minute, artifact-free sections pre-pace and during pacing were used for analysis.

Cardiac Autonomic Blockade

Cardiovagal blockade with atropine, cardiac sympathetic blockade with metoprolol, and dual blockade with both atropine and metoprolol were performed to investigate the autonomic substrates of HRV and PRV. After local anesthesia with lidocaine, an intravenous (IV) catheter was inserted into a marginal ear vein to allow IV administration of cardiac autonomic blockers. Each rabbit was allowed to rest for ten minutes after the placement of the IV catheter, at which point a 1 mL bolus of saline was given and recording of pulsatile arterial pressure and ECG was initiated. Fifteen minutes later, a bolus of either atropine methyl bromide (0.2 mg/kg; Sigma-Aldrich Corp., St. Louis, MO), metoprolol bitartrate (1 mg/kg; Sigma-Aldrich Corp., St. Louis, MO), or both was given. We have used these doses previously to block cardiac parasympathetic and sympathetic outflow in normal and heart failure rabbits (16; 28). Five-minute, artifact-free sections pre- and at least three minutes post-bolus were used for HRV and PRV analysis, and the changes in time, frequency, and non-linear HRV and PRV statistics were analyzed for correlation and agreement. The fold change was used for the LF/HF ratio and the detrended fluctuation analysis scaling exponents.

Interval Detection and Time-Domain Indices

Both R wave and pulse wave detection was performed using the HRV module of LabChart 7 software (ADInstruments, Inc., Colorado Springs, CO). R wave detection was performed by finding the maximum of the ECG signal (Figure 10A). The first time derivative of the arterial pressure signal was calculated using a 3-point window and 45-Hz low-pass filtered for pulse wave detection (Figure 10C). Because of the large impact of pulse wave detection on resultant PRV measures, three different fiducial points were screened for their time-domain, frequency-domain, and non-linear fidelity to the R-R interval signal: (1) the relative maximum of

the dAP/dt signal, denoted max dAP/dt; (2) the zero of the dAP/dt signal prior to the maximum, corresponding to the diastolic minimum and denoted diastolic min; and (3) the zero of the dAP/dt signal after the maximum, corresponding the systolic maximum and denoted systolic max. Per the LabChart HRV module, the timing of the maxima of the dAP/dt and R-wave signals was computed via three-point quadratic interpolation and the timing of zero crossings were linearly interpolated, both with 1 μs precision. The resulting intervals were manually screened for artifacts and exported for subsequent time-domain analysis in Kubios HRV (Biosignal Analysis and Medical Imaging Group, University of Eastern Finland, Kuopio, Finland).

Frequency-Domain Indices

Frequency-domain analysis was carried out in Kubios HRV. Briefly, the tachogram was linearly interpolated at 8 Hz, 50% overlapped 1024-point windows were transformed into the frequency domain, and the resulting power spectra were averaged per Welch's periodogram method. Based on previously published studies in rabbits, the 0-0.0625 Hz band was considered very low frequency (VLF), 0.0625-0.1875 Hz was considered low frequency (LF), and 0.1875-2 Hz was considered high frequency (HF) [115,116].

Non-linear Indices

Multiscale entropy analysis used code publically available as part of PhysioNet with m=2, r=0.15 to compute all odd scale factors from one to 39 [117,118]. While many different parameters have been derived from multiscale entropy analysis [109,113], only two were used in this study. To assess the fidelity of the tachograms of different pulse detection methods to non-linear aspects of the R-R tachogram, the entropy difference (|HRV-PRV|) for each scale factor of was computed for each baseline recording. For the remainder of the study, we used the sum of the entropy over all the computed scales ($MSE_{\sum 1\text{-}39}$) to represent multiscale entropy because of its prognostic value in large patient studies[98,110–112]. All other non-linear indices were computed in Kubios HRV, including Shannon, approximate, and sample entropy. Detrended fluctuation analysis (DFA) was used to

calculate short-term (4-16 sample) and long-term (16-64 sample) scaling exponents denoted as α_1 and α_2 respectively.

Statistical Analysis

All group data are expressed as the mean ± SEM. All r^2 values denote the square of Pearson's correlation coefficient. As some correlations appeared to be driven by outliers, all points with a Cook's distance greater than 4/n were removed to give a corrected r^2, denoted $\dot{r}^2$, where applicable. Since Pearson's correlation coefficient quantifies linear correlation, not agreement, we have employed Bland-Altman plots to show accuracy and precision. To allow easier comparison between indices, all Bland-Altman plots are displayed with percent difference on the y-axis, and we have adopted a uniform terminology. A mean percent difference less than 5%, from 5-15%, and above 15% are considered high, moderate, and poor accuracy respectively. Precision, defined as 1.96 standard deviations, of less than 10%, from 10-20%, and above 20% are considered high, moderate, and poor respectively. The percent difference in parameter *X* is defined as:

$$\frac{X_{HRV} - X_{PRV}}{\frac{1}{2}(X_{HRV} + X_{PRV})} \times 100\%$$

Bias consistency was defined as the proportion of recordings that were biased in the same direction (i.e. $X_{PRV} < X_{HRV}$ or $X_{PRV} > X_{HRV}$) as the mean. The bias consistency was then tested against a uniform distribution using the Pearson chi-squared test with $p < 0.05$ considered significant. This statistical significance formed the basis for any parameters denoted as consistently biased (e.g. consistently overestimated or consistently underestimated).

Statistical differences between pulse detection methods and pre-and post-intervention were tested by repeated measure (RM) ANOVA with pulse detection method and, where relevant, frequency or scale factor as within-recording factors. Post-hoc tests were performed using the Holm-Sidak correction for multiple comparisons. Statistical differences

between pre- and post-intervention (i.e. autonomic blockade or pacing) were tested by paired t-tests or, where appropriate, RM ANOVA.

Other Analysis

The normalized cross-correlation, magnitude-squared coherence, and transfer function gain between HRV and PRV tachograms were calculated using MATLAB (The Mathworks, Inc., Natick, MA). The residual PRV power spectral density for each animal was calculated by subtracting the post-pace HRV power spectrum from the post-pace PRV power spectrum. The percent of PRV power that was independent of HRV was defined as

$$1 - \frac{G(f) * HRV(f)}{PRV(f)}$$

where G(f) is the transfer function gain and HRV(f) and PRV(f) denote the HRV and PRV autospectra. For all MATLAB frequency domain calculations, tachograms were linearly interpolated at 8 Hz, and the corresponding spectra were computed by Welch's periodogram method using 256-point Hamming-windowed segments with 50% overlap.

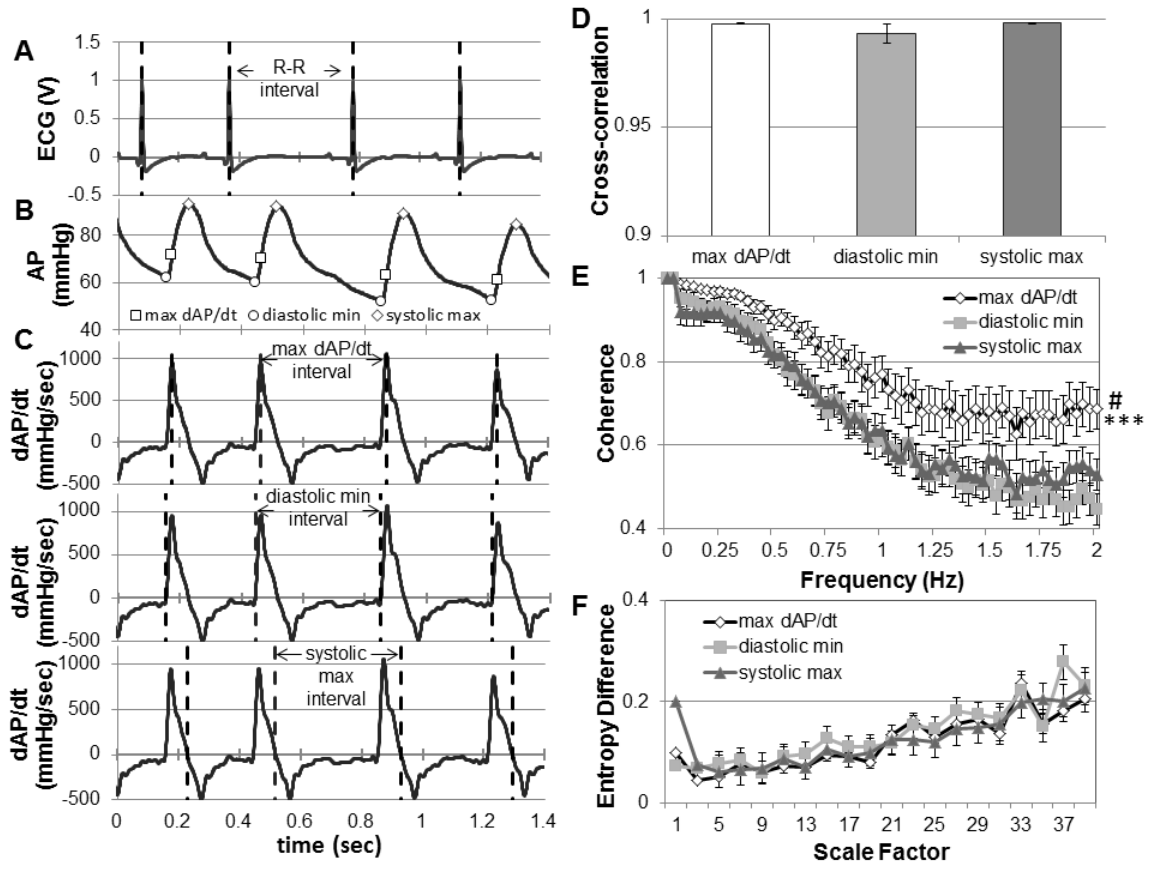

Figure 10 – Pulse Interval Detection Method Screening

Representative tracings of (A) the electrocardiogram signal, (B) the arterial pressure signal with different fiducial points, and (C) the first time derivative of the arterial pressure signal. The detected R waves and pulse waves are shown with dotted lines. (C) Pulse intervals for the three different arterial pulse fiducial points, (top) max dAP/dt, (middle) diastolic minimum, and (bottom) systolic maximum, are displayed. (D) Cross-correlation of the tachogram for each pulse detection method with the R-R interval tachogram. (E) Magnitude-squared coherence between the spectrogram for each pulse detection method and the R-R interval spectrogram. (F) Entropy difference between the R-R interval tachogram and the pulse interval tachogram over multiple scale factors. All values are displayed as mean ± SEM, n = 30. ***, $p < 0.001$ vs. diastolic minimum; #, $p < 0.05$ vs. systolic maximum by 2-way RMANOVA with post-hoc Holm-Sidak tests.

Results

Pulse Interval Detection Method

Three different fiducial points derived from the dAP/dt signal were screened using time-domain, frequency-domain, and non-linear measures to identify the best pulse interval detection method. In the time domain (Figure 10D), the normalized cross-correlation was very close to 1 for all methods, indicating that the pulse interval tachograms are largely a time-lagged function of the R-R tachogram, with no statistically significant effect of fiducial point on cross-correlation. In the frequency domain (Figure 10E), magnitude-squared coherence with the R-R spectra shows a similar trend for all methods, starting near 1 and falling as frequency increases. More important, the coherence was significantly higher for dAP/dt max than for the other two fiducial points. In the non-linear domain (Figure 10F), the pulse detection methods did not significantly affect the difference in entropy from that of the R-R tachogram over multiple scale factors. Thus, because of its superiority in the frequency domain, the maximum of the dAP/dt signal was used to calculate PRV for the remainder of the study. For completeness, tables of data for the systolic maximum and diastolic minimum fiducial points are included in Table 1 and Table 2, respectively, of Appendix A.

Table 9 – Indices of HRV and PRV for 30 baseline recordings

Category	Index	HRV	PRV	Bland-Altman Interval (%)	Bias Consistency	r^2 ($\dot{r}^2$)
Time Domain	Heart rate (bpm)	187 ± 4	187 ± 4	-0.0422 ± 0.0807	27/30***	1.00
	SDNN (ms)	26.8 ± 2.6	27.4 ± 2.7	-2.03 ± 2.98	29/30***	0.999 (0.999)
	RMSSD (ms)	25.1 ± 3.1	25.8 ± 3.3	-2.56 ± 5.70	18/30	0.996 (0.995)
Frequency Domain	Total Power (ms^2)	847 ± 165	883 ± 177	-3.32 ± 6.51	27/30***	0.999 (0.999)
	VLF Power (ms^2)	299 ± 55.7	302 ± 57	-0.48 ± 1.53	16/30	0.999 (1.00)
	LF Power (ms^2)	102 ± 18	105 ± 18	-3.06 ± 2.16	28/30***	0.999 (0.999)
	LF Power (nu)	25.8 ± 2.5	25.2 ± 2.4	2.33 ± 9.99	21/30*	0.989 (0.994)
	HF Power (ms^2)	444 ± 103	473 ± 112	-6.5 ± 15.2	26/30***	0.998 (0.997)
	HF Power (nu)	73.6 ± 2.5	74.3 ± 2.4	-1.07 ± 4.98	21/30*	0.988 (0.994)
	LF/HF Ratio	0.413 ± 0.062	0.396 ± 0.059	3.39 ± 14.33	21/30*	0.986 (0.996)
Non-linear	$MSE_{\sum 1\text{-}39}$	29.9 ± 0.7	30.0 ± 0.7	-0.59 ± 5.86	16/30	0.947 (0.970)
	Shannon Entropy	3.81 ± 0.09	3.79 ± 0.09	0.59 ± 3.38	20/30	0.989 (0.987)
	Approximate Entropy	1.24 ± 0.04	1.26 ± 0.03	-1.83 ± 7.44	19/30	0.953 (0.969)
	Sample Entropy	1.26 ± 0.06	1.28 ± 0.05	-2.3 ± 12.2	19/30	0.949 (0.964)
	DFA short-term (α_1)	0.949 ± 0.032	0.914 ± 0.030	3.7 ± 22.7	21/30*	0.654 (0.636)
	DFA long-term (α_2)	0.948 ± 0.034	0.935 ± 0.033	1.36 ± 6.97	24/30**	0.971 (0.986)

Values are displayed as mean ± SEM, Bland-Altman intervals (mean bias ± 95% limits of agreement), bias consistency, and pairwise coefficient of determination (r^2) between HRV and PRV values. Where applicable, the r^2 values after removal of points with a Cook's distance > 0.133 (denoted $\dot{r}^2$) are displayed in parentheses. * $p < 0.05$, ** $p < 0.01$, *** $p < 0.001$ by Pearson's χ^2 test.

Baseline Time-Domain Indices

As Figure 11A illustrates, tachograms obtained from ECG and arterial pulse signals are visually very similar. Figure 11B shows a very high correlation between PRV and HRV measures of SDNN. Bland-Altman plotting (Figure 11C) reveals that PRV consistently overestimates SDNN, but PRV SDNN is still highly accurate and precise. In the baseline condition, all time domain indices of PRV show a strong correlation with HRV measures as well as high precision and accuracy (Table 9).

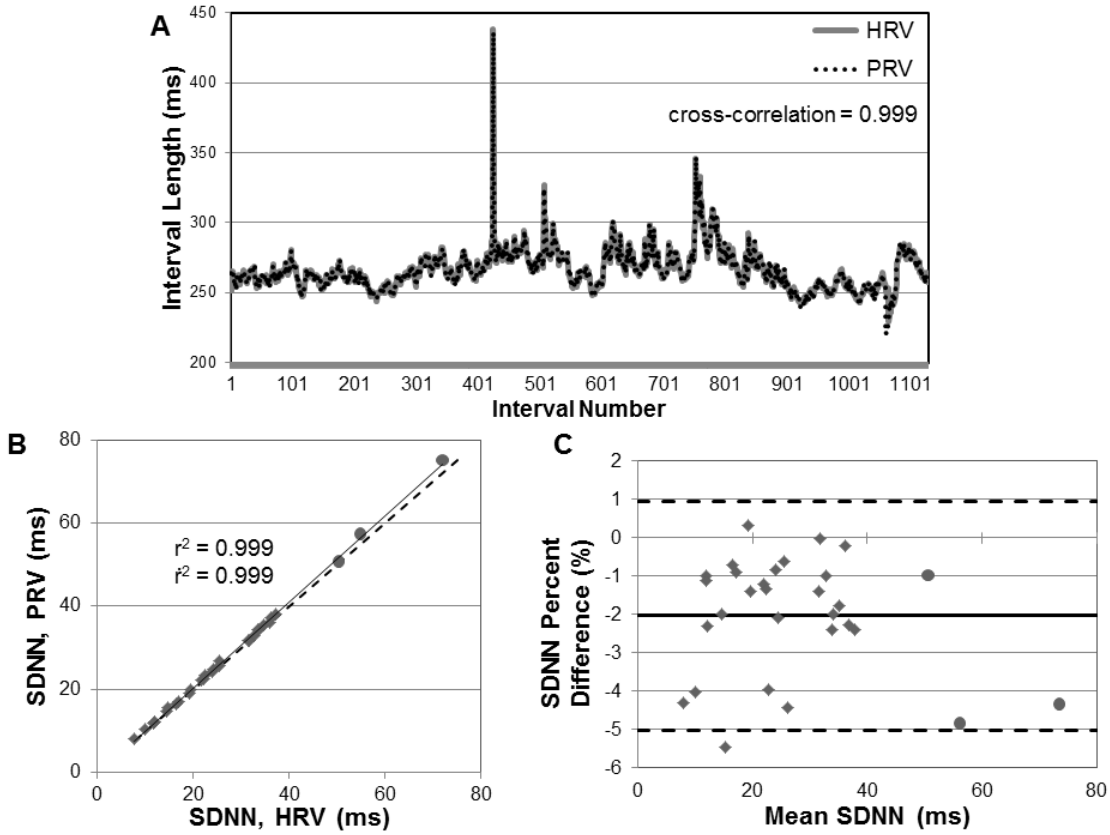

Figure 11 – Time Domain Statistics at Baseline

(A) Representative HRV (solid gray line) and PRV (dotted black line) tachograms. (B) Scatter plot of PRV SDNN versus HRV SDNN with line of best fit (solid gray) and line of equality (dotted black). Points with Cook's $d > 4/n$ are displayed as circles. (C) Bland-Altman plot showing the percent difference in SDNN (HRV-PRV) versus the pairwise mean SDNN with the mean bias (solid horizontal line) and the upper and lower 95% limits of agreement (dashed horizontal lines). r^2, Pearson's mean-squared pairwise coefficient of determination; $\dot{r}^2$, Pearson's mean-squared pairwise coefficient of determination excluding points with Cook's $d > 0.133$.

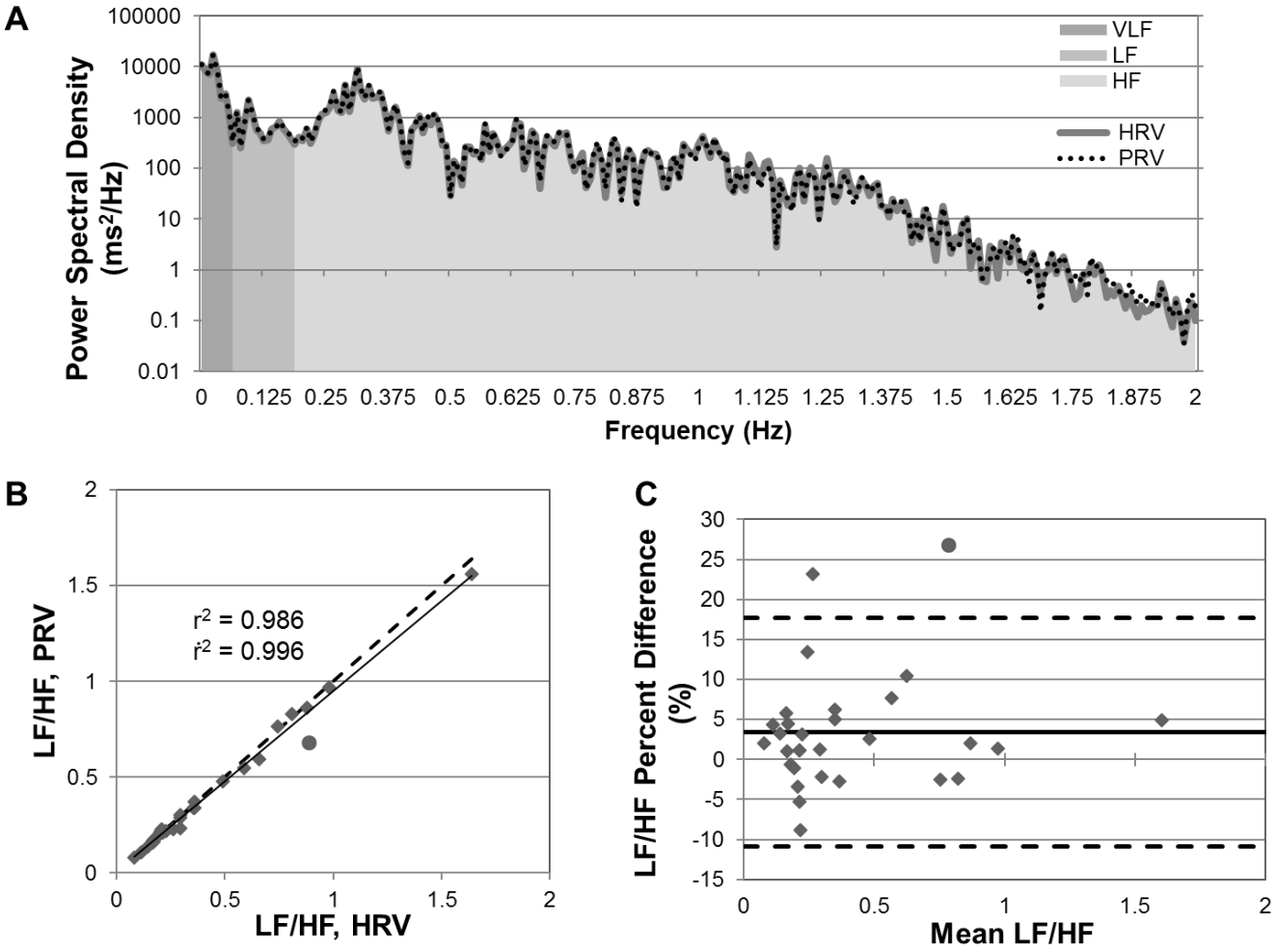

Figure 12 – Frequency Domain Statistics at Baseline

(A) Representative HRV (solid gray line) and PRV (dotted black line) spectra on a semilog plot with shading denoting VLF, LF, and HF frequencies. (B) Scatter plot of PRV LF/HF ratio versus HRV LF/HF ratio with line of best fit (solid gray) and line of equality (dotted black). (C) Bland-Altman plot showing the percent difference in LF/HF (HRV-PRV) versus the pairwise mean LF/HF with the mean bias (solid line) and the upper and lower 95% limits of agreement (dashed lines). r2, Pearson's mean-squared pairwise coefficient of determination; ṙ2, Pearson's mean-squared pairwise coefficient of determination excluding points with Cook's d > 0.133

Baseline Frequency-Domain Indices

Figure 12A illustrates the visual similarity between the HRV and PRV power spectra for one recording. As would be expected from the coherence plots (Figure 10E), the spectra are very similar at lower frequencies and become more disparate at higher frequencies. As Figure Figure 12B shows, the PRV LF/HF ratio correlates strongly with the HRV measure. Bland-Altman plotting (Figure 12C) illustrates that PRV consistently underestimates the LF/HF ratio but still shows high accuracy and precision. The underestimation of LF/HF results from the fact that, while PRV consistently exaggerates the power in all frequency measures except the very-low frequency range, this tendency is greatest for high frequency power. All other spectral measures of PRV show high accuracy and precision in resting rabbits except high frequency power, which is only moderately accurate and precise (Table 9).

4

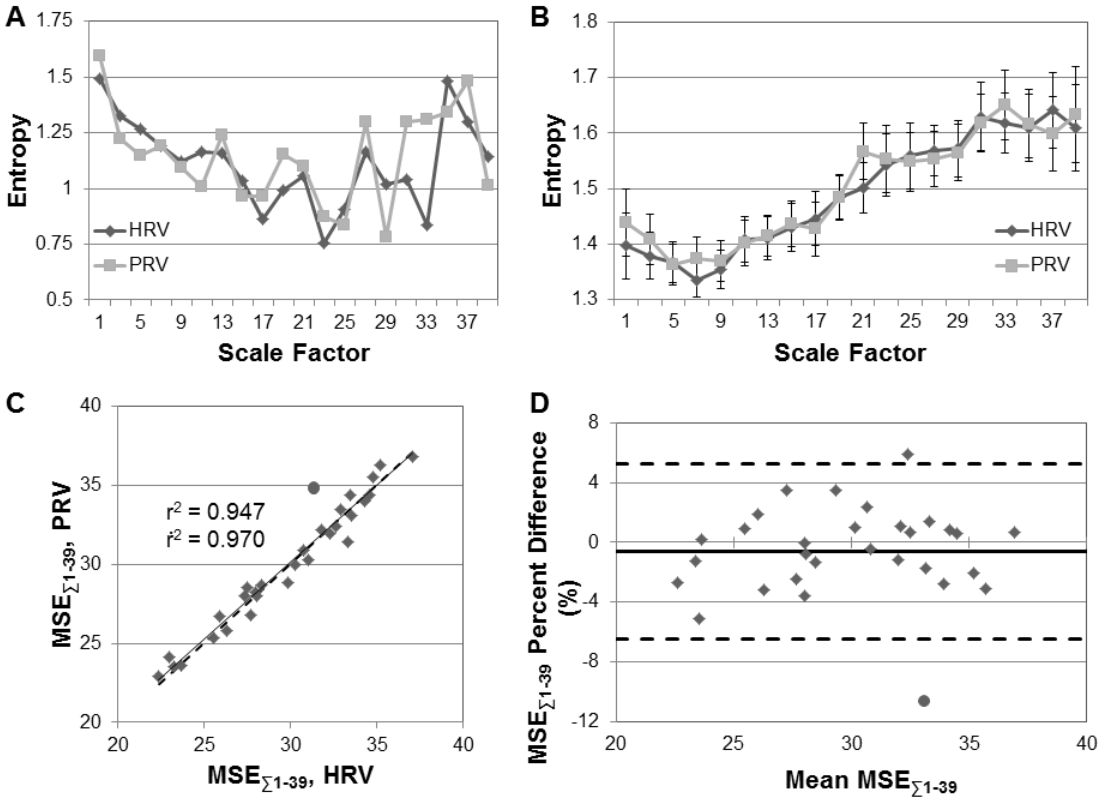

Figure 13 – Non-linear Statistics at Baseline

(A) PRV and HRV sample entropy at multiple scale factors for a single recording. (B) PRV and HRV sample entropy at multiple scale factors for all recordings displayed as mean ± SEM, n = 30. (C) Scatter plot of PRV multiscale entropy (the sum over odd scale factors from 1-39) versus HRV multiscale entropy with line of best fit (solid gray) and line of equality (dotted black). (D) Bland-Altman plot showing the percent difference in multiscale entropy (HRV-PRV) versus the pairwise mean multiscale entropy with the mean bias (solid line) and the upper and lower 95% limits of agreement (dashed lines). r^2, Pearson's mean-squared pairwise coefficient of determination; $ŕ^2$, Pearson's mean-squared pairwise coefficient of determination excluding points with Cook's d > 0.133.

Baseline Non-linear Indices

Figure 13A illustrates the visual difference between HRV and PRV sample entropy at different scale factors for a single recording. These differences are not apparent in the group data (Figure 13B). Although the correlation between HRV and PRV multiscale sample entropy is strong (Figure 13C), it is clearly not as robust as the correlations for time- and frequency-domain indices. Again contrasting from time- and frequency-domain measures, PRV multiscale entropy is not consistently biased (Figure 13D, (Table 9). The Bland-Altman plot also shows high accuracy and precision for multiscale entropy (Figure 13D). While most of the PRV non-linear indices show a strong correlation with corresponding HRV indices, these relationships tend to be notably weaker than those observed for time- and frequency-domain measures (Table 9). The short-term detrended fluctuation analysis scaling exponent (α_1) shows a particularly poor correlation. In the baseline condition, all non-linear measures have high accuracy, and all but α_1 and sample entropy also have high precision.

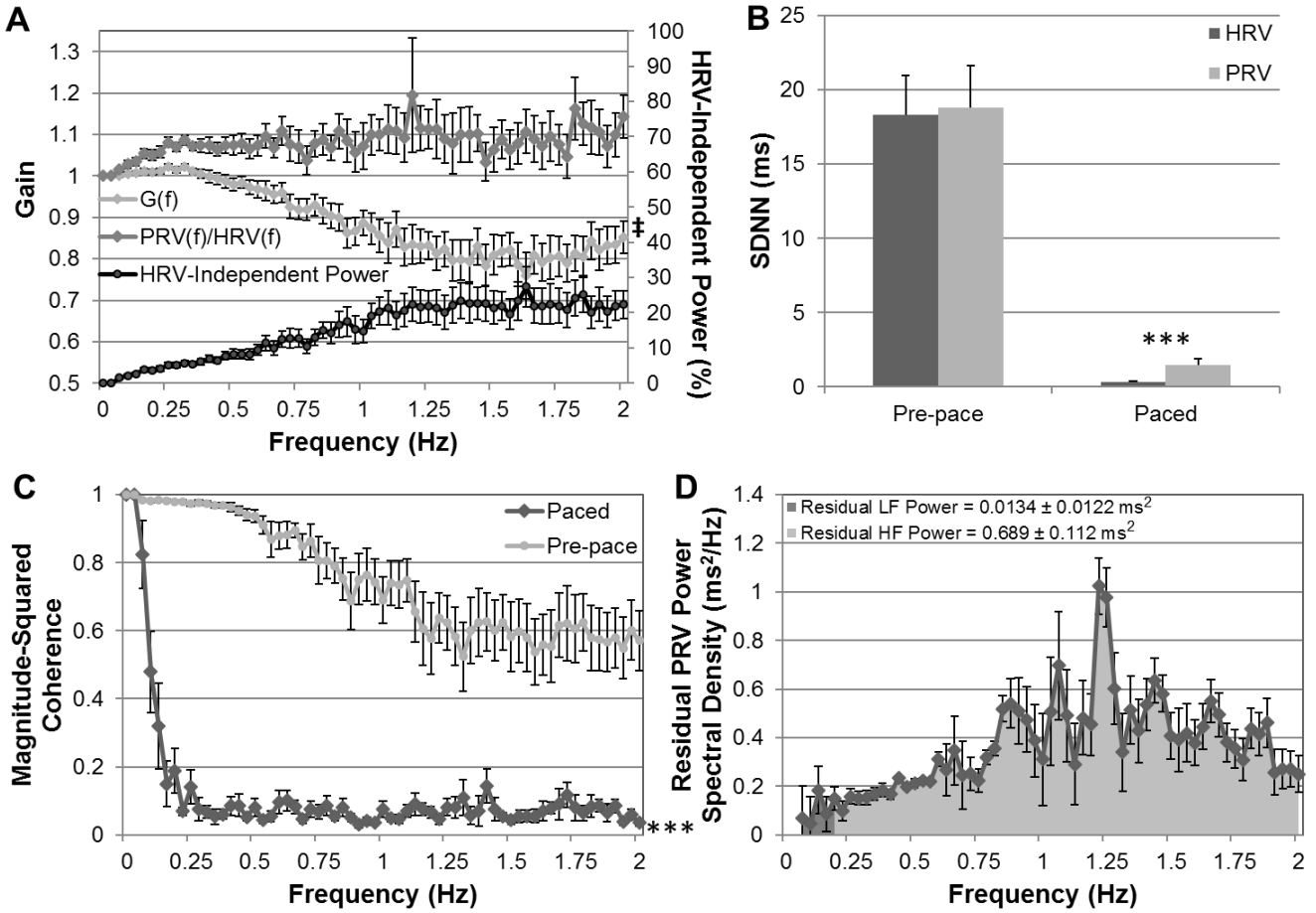

Figure 14 – Transfer Function Analysis and Ventricular Pacing Experiments

. (A) Transfer function gain, G(f), the PRV:HRV ratio, PRV(f)/HRV(f), and HRV-independent power as a function of frequency at baseline, n = 30. (B) The effect of pacing on HRV and PRV SDNN, n = 8. (C) The effect of ventricular pacing on the coherence between HRV and PRV as a function of frequency, n = 8. (D) The residual PRV power spectrum for paced rabbits, n = 8.

Ventricular Pacing

Because PRV consistently overestimated both time- and frequency-domain measures of HRV at baseline, we investigated if PRV was simply amplifying HRV or if other, HRV-independent rhythms accounted for this increased variability. Figure 14A shows that transfer function gain is greater than 1 from 0 Hz to 0.375 Hz, indicating that PRV does indeed amplify HRV, albeit modestly, over the frequency range containing the vast majority of the HRV power. Interestingly, however, the ratio of PRV power to HRV power demonstrates that this amplification does not completely explain the tendency of PRV to overestimate HRV, and the percent of PRV power that is independent of HRV increases with frequency until stabilizing at approximately 1.25 Hz.

Ventricular pacing experiments were conducted to assess the HRV-independent rhythms of PRV by driving HRV to zero. As Figure 14B shows, ventricular pacing almost completely eliminates HRV (post-pace SDNN = 0.32 ± 0.04 ms) and significantly attenuates PRV. Still, PRV remains non-negligible, indicating a minimum PRV SDNN of 1.47 ± 0.13 ms. Figure 14C displays the magnitude-squared coherence for pre-pace and paced conditions. As expected, the coherence equals 1 at 0 Hz, indicating the mean rate is the same for PRV and HRV. The coherence sharply declines until 0.25 Hz, beyond which point the coherence remains very low, indicating the absence of a relationship between paced PRV and HRV for these frequencies. Subtraction of the paced heart rate spectrogram from the pace pulse rate spectrogram yields the residual PRV spectrum, (Figure 14D) which showed a peak at 1.25 Hz. This HRV-independent rhythm could explain some of the tendency of PRV to specifically overestimate the high-frequency component of the HRV spectrum. It could also explain the trend of magnitude-squared coherence (Figure 10, Figure 14C) to fall as frequency increases and this HRV-independent variability constitutes a greater proportion of PRV power.

Table 10 – Changes in indices of HRV and PRV after cardiac autonomic blockade

		Atropine		Metoprolol		Double Blockade	
Category	Index	Bland-Altman Interval (%)	r^2 ($\dot{r}^2$)	Bland-Altman Interval (%)	r^2 ($\dot{r}^2$)	Bland-Altman Interval (%)	r^2 ($\dot{r}^2$)
Time Domain	ΔHR (bpm)	0.209 ± 0.476	1.00 (1.00)	0.460 ± 6.14	1.00 (1.00)	0.088 ± 0.255	1.00 (1.00)
	ΔSDNN (ms)	-2.03 ± 4.95	0.995 (0.999)	2.28 ± 7.50	0.999	-0.37 ± 3.88	0.997 (0.999)
	ΔRMSSD (ms)	-0.2 ± 10.4	0.981 (0.956)	-3.6 ± 19.7	0.992 (0.996)	3.6 ± 12.1	0.981 (0.992)
Frequency Domain	ΔTotal Power (ms^2)	-4.17 ± 9.12	0.993 (0.996)	-0.22 ± 8.37	1.00 (0.998)	-2.73 ± 4.68	1.00 (0.999)
	ΔVLF Power (ms^2)	-0.12 ± 3.26	0.998	-3.61 ± 13.2	0.999	-0.43 ± 2.52	0.999 (1.00)
	ΔLF Power (ms^2)	-3.71 ± 9.75	0.998 (0.998)	2.6 ± 18.9	0.999 (1.00)	-3.13 ± 2.90	1.00 (1.00)
	ΔLF Power (nu)	-49.5 ± 101.5	0.900	0.0 ± 17.2	0.990 (0.999)	-458 ± 2545	0.337 (0.065)
	ΔHF Power (ms^2)	-6.84 ± 13.97	0.996 (0.991)	-2.1 ± 10.9	1.00 (0.999)	-3.67 ± 6.78	1.00 (0.998)
	ΔHF Power (nu)	50.3 ± 202	0.901	-0.35 ± 18.5	0.998 (0.999)	2277 ± 1517	0.353 (0.040)
	LF/HF Fold Change	-55.5 ± 106.3	0.996 (0.734)	-4.6 ± 11.5	0.987 (0.971)	-95.7 ± 64.1	0.045 (0.015)
Non-linear	$\Delta MSE_{\sum 1\text{-}39}$	61 ± 211	0.760 (0.843)	-89 ± 1453	0.553 (0.618)	153 ± 412	0.761 (0.258)
	ΔShannon Entropy	-16 ± 291	0.776 (0.636)	-2.32 ± 21.8	0.997	-201 ± 600	0.691
	ΔApproximate Entropy	-34 ± 233	0.653 (0.631)	-81 ± 542	0.858 (0.581)	-100 ± 872	0.616
	ΔSample Entropy	-62 ± 279	0.613 (0.339)	-8 ± 155	0.914 (0.832)	-294 ± 2287	0.612
	DFA α_1 Fold Change	-3.3 ± 96.3	0.505 (0.673)	4.95 ± 4.90	0.905	38.4 ± 51.0	0.709
	DFA α_2 Fold Change	-4.8 ± 27.6	0.677 (0.542)	-0.44 ± 3.62	0.955 (0.980)	15.4 ± 27.3	0.802 (0.619)

Agreement and correlation of the changes in indices of HRV and PRV after autonomic blockade are displayed as Bland-Altman intervals (mean bias ± 95% limits of agreement) and pairwise coefficient of determination (r^2). Where applicable, the r^2 values after removal of points with a Cook's distance > 0.5 (denoted $\dot{r}^2$) are shown in parentheses.

Table 11 – Indices of HRV and PRV before and after cardiac autonomic blockade

		Before Atropine		After Atropine	
Category	Index	HRV	PRV	HRV	PRV
Time Domain	HR (bpm)	178 ± 6	178 ± 6	233 ± 8***	233 ± 8***
	SDNN (ms)	26.4 ± 2.4	27.2 ± 2.8	4.27 ± 0.70***	4.48 ± 0.62***
Frequency Domain	Total Power (ms^2)	767 ± 155	820 ± 188	13.3 ± 3.3**	14.3 ± 3.3**
	LF Power (ms^2)	113 ± 20	118 ± 21	2.3 ± 1.0**	2.5 ± 1.1**
	HF Power (ms^2)	396 ± 121	444 ± 154	1.04 ± 0.30*	1.80 ± 0.31*
Non-linear	$MSE_{\sum 1\text{-}39}$	36.4 ± 3.1	36.7 ± 4.1	28.4 ± 5.3	24.1 ± 2.7
		Before Metoprolol		After Metoprolol	
Time Domain	HR (bpm)	191 ± 6	191 ± 6	186 ± 4	186 ± 4
	SDNN (ms)	20.8 ± 3.0	21.0 ± 3.0	16.4 ± 2.6*	16.6 ± 2.6*
Frequency Domain	Total Power (ms^2)	477 ± 168	491 ± 175	272 ± 83	283 ± 89
	LF Power (ms^2)	50.1 ± 11.7	51.4 ± 12.1	56.5 ± 21.0	57.7 ± 21.6
	HF Power (ms^2)	252 ± 121	264 ± 128	121 ± 40	129 ± 44
Non-linear	$MSE_{\sum 1\text{-}39}$	39.1 ± 2.6	39.3 ± 2.8	45.6 ± 5.7	44.5 ± 4.66
		Before Double Blockade		After Double Blockade	
Time Domain	HR (bpm)	176 ± 5	177 ± 5	234 ± 7***	234 ± 7***
	SDNN (ms)	28.0 ± 2.6	28.4 ± 2.7	1.51 ± 0.12***	1.82 ± 0.15***
Frequency Domain	Total Power (ms^2)	994 ± 279	1031 ± 295	1.45 ± 0.14*	2.25 ± 0.26*
	LF Power (ms^2)	116 ± 29	121 ± 31	0.133 ± 0.027**	0.149 ±
	HF Power (ms^2)	603 ± 215	634 ± 227	0.445 ± 0.098*	1.22 ± 0.230*
Non-linear	$MSE_{\sum 1\text{-}39}$	39.0 ± 3.9	43.2 ± 4.5	34.3 ± 4.9	28.1 ± 3.5

Values are displayed as mean ± SEM. *, **, ***, $p < 0.05$, $p < 0.01$, $p < 0.001$ vs. before blockade

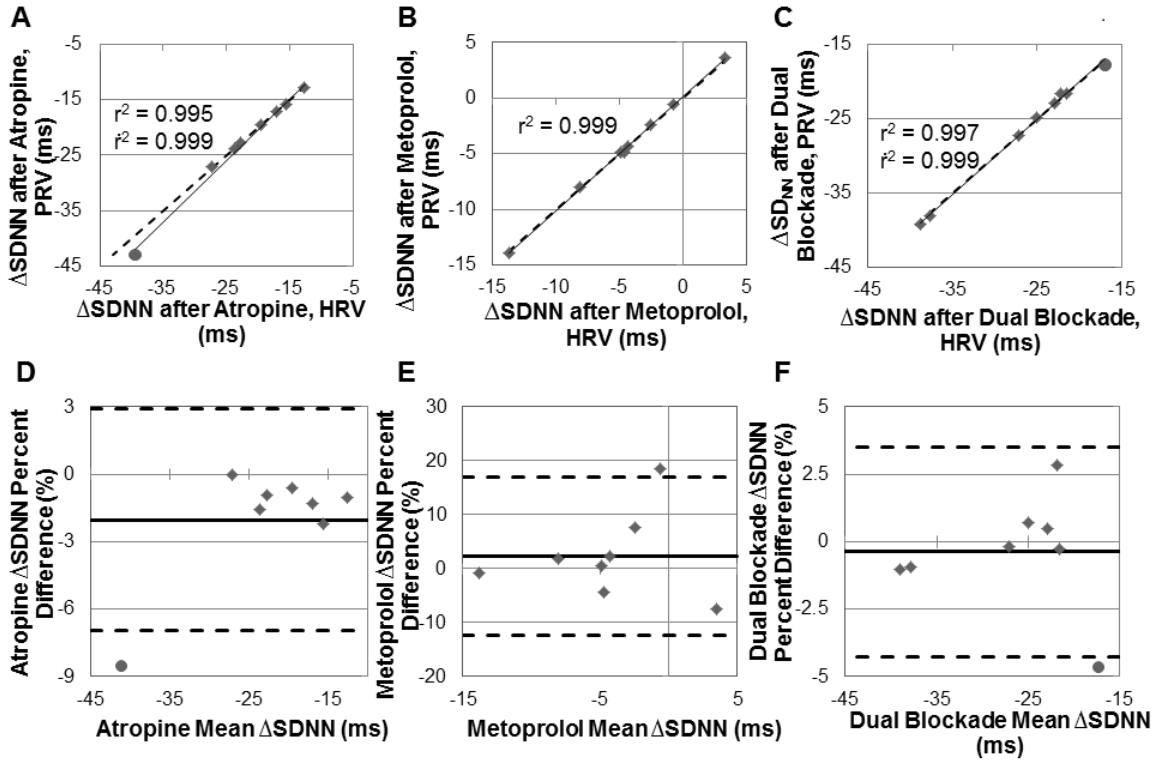

Figure 15 – Effects of Cardiac Autonomic Blockade on SDNN

Scatter plots of the change in PRV SDNN versus change in HRV SDNN after (A) atropine, (B) metoprolol, and (C) dual blockade with lines of best fit (solid gray) and lines of equality (dotted black). Bland-Altman plots showing the percent difference in HRV and PRV ΔSDNN (HRV-PRV) versus the pairwise mean ΔSDNN after (D) atropine, (E) metoprolol, and (F) dual blockade with the mean bias (solid lines) and the upper and lower 95% limits of agreement (dashed lines).

Cardiac Autonomic Blockade – Time Domain

Since many investigators use HRV as an index of cardiac autonomic balance, it is important that changes in cardiac autonomic tone are faithfully represented by PRV. Figure 15A-C shows the strong correlations between the changes in PRV SDNN and HRV SDNN after cardiovagal blockade with atropine, cardiac sympathetic blockade with metoprolol, and combined blockade respectively. Bland-Altman plots (Figure 15D-F) show a high accuracy of the change in PRV SDNN after autonomic blockade. The precision is also high for atropine- and dual blockade-effected changes in SDNN but only moderate for metoprolol, mainly due to one outlier. Also of note, PRV consistently ($p < 0.01$) overestimates the atropine-mediated change in SDNN. Changes in heart rate show high accuracy and precision whereas RMSSD shows high accuracy and moderate precision for each autonomic blockade intervention, and both show strong correlations (Table 10). Overall, PRV accurately reflects changes in HRV time-domain measures that result from acute changes in cardiac autonomic tone.

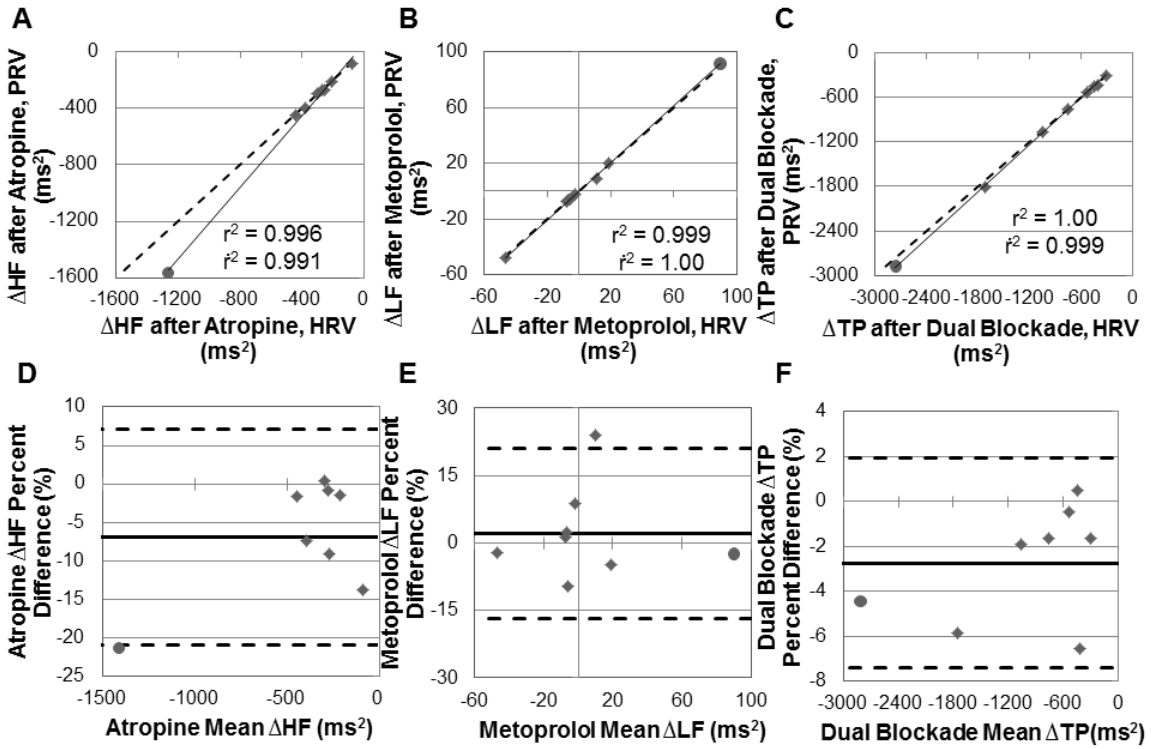

Figure 16 – Effects of Cardiac Autonomic Blockade on Spectral Indices

Scatter plots of (A) the change in PRV high-frequency power versus the change in HRV high-frequency power after atropine, (B) the change in PRV low-frequency power versus the change in HRV low-frequency power after metoprolol, and (C) the change in PRV total power versus the change in HRV total power after dual blockade with lines of best fit (solid gray) and lines of equality (dotted black). Bland-Altman plots showing the percent difference in (D) HRV and PRV ΔHF power (HRV-PRV) versus the pairwise mean ΔHF after atropine, (E) HRV and PRV ΔLF power (HRV-PRV) versus the pairwise mean ΔLF after metoprolol, and (F) HRV and PRV change in total power (HRV-PRV) versus the pairwise mean ΔTP after dual blockade with the mean bias (solid lines) and the upper and lower 95% limits of agreement (dashed lines). r2, Pearson's mean-squared pairwise coefficient of determination; ṙ2, Pearson's mean-squared pairwise coefficient of determination excluding points with Cook's d > 0.5.

Cardiac Autonomic Blockade – Frequency Domain

Atropine administration nearly eliminates high-frequency power, and, as Figure 16A shows, the change in HRV and PRV high-frequency power after atropine is very strongly correlated, but the slope of this relationship is greater than that of the line of equality. The Bland-Altman plot (Figure 16D) shows that the change in PRV high-frequency power is a moderately accurate and precise surrogate for the change in HRV high-frequency power after atropine. More specifically, PRV consistently ($p < 0.05$) exaggerates the change in high-frequency power, likely due to the increased PRV high-frequency power at baseline. Similarly, the correlation between atropine-mediated changes in the absolute power of frequency domain measures of HRV and PRV is very robust and these measures show high accuracy and precision. However, PRV high-frequency power remains higher than HRV high-frequency power (Table 11), likely due to the presence of intrinsic PRV as revealed by our ventricular pacing experiment. While the magnitude of this intrinsic PRV is small, it now constitutes a large proportion of the greatly attenuated total power and exerts negative effects on the normalized powers and LF/HF ratio. As a result, the correlations and agreements of the change in normalized powers and LF/HF ratio fold change are very poor (Table 10).

Metoprolol administration did not have a robust, consistent effect on low-frequency power in all animals; however, PRV reflected the changes in HRV low-frequency power after metoprolol for each rabbit in a highly accurate and moderately precise manner (Figure 16E). Here, the correlation between the PRV and HRV spectral changes was strong for both normalized and absolute measures (Figure 16B, Table 10). In addition, the changes in other HRV and PRV spectral measures after metoprolol showed moderate to high accuracy and precision (Table 10).

Combined autonomic blockade attenuates total power, and the decrease in PRV total power correlates very well with the change in HRV power (Figure 16C). Bland-Altman plotting shows the change in PRV power to be a highly accurate, highly precise estimate of the change in HRV

power (Figure 16D). It is also clear that PRV consistently ($p < 0.05$) exaggerates the decrease in power, likely due to the elevated PRV total power at baseline. Changes in other HRV and PRV frequency-domain statistics demonstrated robust correlations and high accuracy and precision with the notable exception of normalized measures and the LF/HF ratio. These measures showed very poor accuracy and precision; as with atropine, this is likely due to the exaggerated influence of intrinsic PRV when HRV is dramatically decreased by autonomic blockade.

Cardiac Autonomic Blockade – Non-linear Measures

Autonomic blockade-mediated changes in the non-linear measure multiscale entropy differed considerably between PRV and HRV. As Figure 17A-C show, the correlations between the change in PRV multiscale entropy and the change in HRV multiscale entropy are very modest for all three of the autonomic blockade conditions. Moreover, the slopes of the best-fit lines are visibly much less than those of the lines of equality. The Bland-Altman plots (Figure 17D-F) show very poor accuracy and very poor precision for each of the conditions. Similarly disappointing performance was observed with changes in other measures of entropy, which were plagued by poor precision after all interventions (Table 10). The fold changes in the DFA scaling exponents showed mixed strength of agreement, with the long-term statistic α_2 performing the best of the non-linear measures with high accuracy and moderate to high precision after single blockade. Correlations for all non-linear measures varied widely between conditions but were clearly much lower than the time- and non-normalized frequency-domain measures (Table 10).

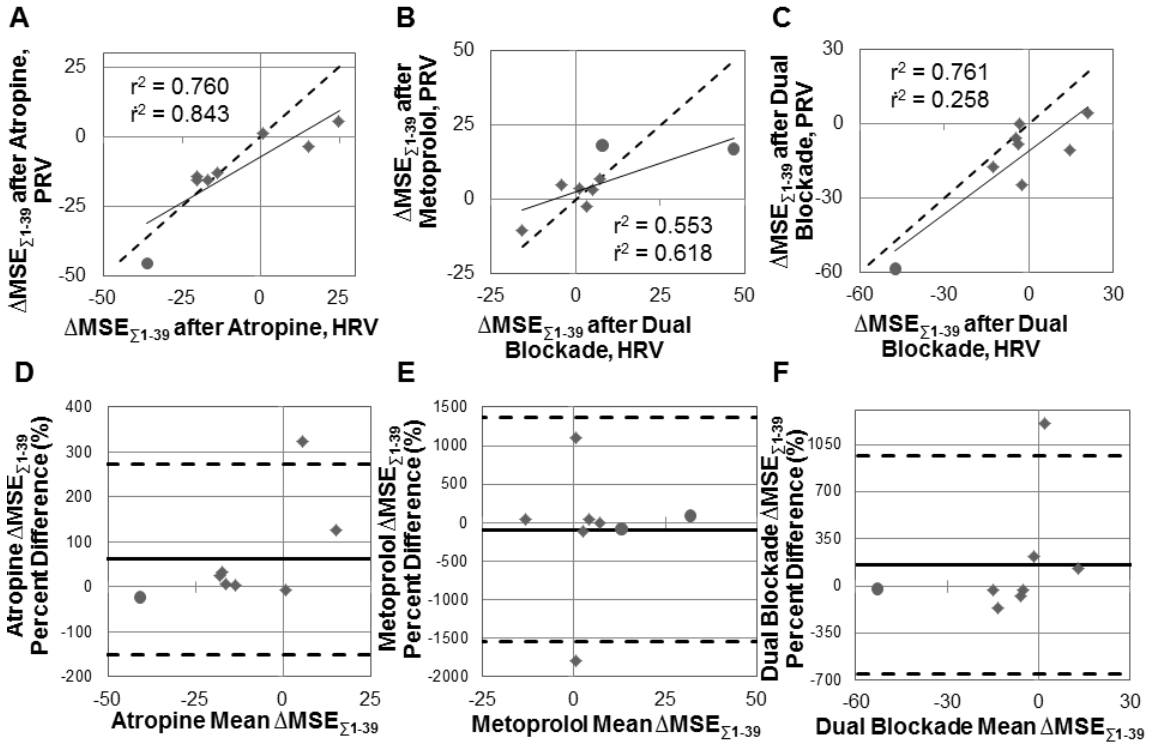

Figure 17 – Effects of Cardiac Autonomic Blockade on Multiscale Entropy

Scatter plots of the change in PRV multiscale entropy versus change in HRV multiscale entropy after (A) atropine, (B) metoprolol, and (C) dual blockade with lines of best fit (solid gray) and lines of equality (dotted black). Bland-Altman plots showing the percent difference in HRV and PRV change in multiscale entropy (HRV-PRV) versus the pairwise mean change in multiscale entropy after (D) atropine, (E) metoprolol, and (F) dual blockade with the mean bias (solid lines) and the upper and lower 95% limits of agreement (dashed lines). r2, Pearson's mean-squared pairwise coefficient of determination; ŕ2, Pearson's mean-squared pairwise coefficient of determination excluding points with Cook's d > 0.5.

Discussion

In general, we found that invasively acquired PRV overestimates corresponding HRV parameters in both the time and frequency domains in resting rabbits. Moreover, while PRV exaggerates HRV power in all frequencies, this effect is most pronounced in the high-frequency range, and interrelated measures like normalized LF and the LF/HF ratio are accordingly decreased when assessed by PRV. While we have shown by transfer function analysis that some of this overestimation is due to amplification of HRV spectral components, we have also shown that HRV-independent oscillations are important as well. This additional variability must come from variations in either pre-ejection time (i.e. the time after ventricular depolarization but before opening of the aortic valve) or pulse transit time (i.e. the time required for the arterial pulse to propagate from the aortic valve to the telemetry catheter). Pre-ejection time is largely a function of contractility, preload, and afterload while pulse transit time is affected by pulse pressure and arterial elasticity [119]. The cyclic effects of respiration on venous return, preload, stroke volume, and thus pulse pressure are believed to account for much of the variability in pre-ejection time and pulse transit time. This is supported by studies that observed peaks in the spectrum of the difference between pulse intervals and R-R intervals in the respiratory frequency range [101,120] as well as the aforementioned tendency for PRV to overestimate HRV specifically in the high frequency range. Although respiration was not measured in this study, a spontaneous respiratory frequency of 1.25 Hz is reasonable for resting rabbits and is the most likely explanation for the residual PRV peak observed during ventricular pacing.

These findings agree with studies using non-invasive methods to calculate time and frequency measures of PRV in resting human subjects [100]. Compared to previous studies using similar pulse detection algorithms, our invasively acquired PRV data show better correlations and better agreement with HRV measures than PRV sampled by non-invasive methods[120–122]. This is

likely due to the more proximal location of the pulse wave sensor (i.e. aorta versus finger), which in turn decreases the variability in pulse transit time.

A previous study performed by Bhatia et al showed that low sampling rates negatively impact the accuracy of indices of heart rate and blood pressure variability in rats and mice but that accuracy can be restored by interpolation of the downsampled signal[123]. This is particularly relevant to our study as the DSI PA-C40 pressure telemetry has an internal sampling rate of 500 Hz whereas the ECG was digitized at 1 kHz. As the signal used for pulse interval detection was resampled with 1 μs (i.e. 1 MHz) precision, we do not believe this was a confounding factor in our study. Interestingly, these authors also recorded simultaneous ECG and arterial pressure in the rats in this study and found that the SDNN, RMSSD, triangular index, and low-frequency power, but not high-frequency power, could be estimated from the arterial pulse signal with less than 10% difference from the HRV measures. In our study, the ability of PRV to estimate HRV high-frequency power was better (7.01% difference using the same formula). This may be due to species differences or due to the poorer coherence of the diastolic minimum fiducial point used in this study.

The effect of pulse detection on the correlation and agreement of non-invasive PRV and HRV measures in humans has been investigated previously [124]. These authors found that a tangent method based on the timing of the max dAP/dt was superior to both the diastolic minimum and max d^2AP/dt. Our results similarly show the frequency-domain superiority of the max dAP/dt to the diastolic minimum and systolic maximum as a fiducial point, although we have employed more accessible and computationally simpler techniques than these authors.

While, at baseline, non-linear PRV measures showed high accuracy but mixed precision in approximating corresponding HRV measures, none showed the highly robust correlations ($r^2 > 0.99$) like those observed for time- and non-normalized frequency-domain measures. Our attempts to augment the linearity of the relationship by plotting the log of PRV parameters vs. the log of HRV parameters did not substantially improve these correlations (data not shown). Moreover,

changes in most non-linear measures of PRV after autonomic blockade were shown to be a very poor surrogate for changes in HRV non-linear measures, suffering from poor accuracy, precision, and weak correlations. We thus do not recommend the use of PRV as a surrogate for HRV if non-linear measures are a primary endpoint, especially in studies that manipulate autonomic tone.

One unexpected finding in our study was the lack of a strong change in low-frequency power after beta-blockade, which differs from previous studies in rabbits[104]. While this dose of metoprolol results in a profound bradycardia in rabbits with chronic heart failure(16), it did not significantly decrease heart rate ($p = 0.180$) in this group of animals. Others have also reported the absence of a frequency domain change after beta-blockade in normal animals[102]. We believe the lack of a clear bradycardia and spectral effect after metoprolol reflects low sympathetic tone in these healthy, resting rabbits.

It is important to point out that the criteria for high, moderate, and low accuracy and precision were fixed prior to analysis in an arbitrary manner. How much two methods can differ without becoming problematic depends on the intended application and is not a question that statistical methods can answer[125]. Thus, it is important that investigators wishing to use PRV as a surrogate for HRV in chronically instrumented animals look critically at the data presented here and decide for themselves whether or not the demonstrated agreements and correlations are sufficient for their purposes.

For investigators interested in using invasively acquired PRV measures as an index of cardiac autonomic balance, these data also pose an important question of the necessity for agreement versus correlation. Clearly, changes in time-domain and absolute spectral power measures of PRV explain autonomic blockade-mediated changes in corresponding HRV measures in a very robust manner (i.e. coefficient of determination greater than 0.99). For studies in which the principal purpose of PRV analysis is the assessment of cardiac autonomic state, these robust linear relationships may be sufficient to justify the use of PRV. We advise special attention for using PRV in conditions in which HRV is very low, as residual PRV may constitute an

unacceptably high proportion of total PRV, and in conditions or maneuvers that modify vagal tone, as PRV appears to amplify these changes.

Finally, we would like to point out some of the limitations of our study. Using pharmacological autonomic blockade is a convenient, acute method to manipulate cardiac sympathovagal balance, but these findings do not address the ability of PRV to reflect chronic changes in HRV. Similarly, it is difficult to generalize these findings in healthy animals to disease models, including those with autonomic dysfunction and cardiorespiratory disorders. Moreover, given the species-specific nature of HRV rhythms, it is unclear how the observed trends translate to other animal models like mice, rats, and dogs. Monitoring respiratory frequency would also have provided important insight into the source of intrinsic PRV.

In summary, invasively acquired PRV is generally an accurate and precise surrogate for time, frequency, and some non-linear measures of HRV at baseline. The tendency for PRV to slightly overestimate HRV parameters in the time and frequency domains can be explained both by amplification of HRV oscillations as well as its composition by HRV-independent rhythms. Furthermore, while robust correlations and moderate to high agreement exist between the changes in time- and absolute frequency-domain PRV and HRV parameters after autonomic blockade, most non-linear parameters show very poor agreement after administration of autonomic blockers. Thus, invasively acquired PRV is likely an acceptable surrogate for HRV except when non-linear measures are a primary endpoint or when HRV is greatly reduced such that HRV-independent oscillations predominate. These findings are relevant to investigators who wish to use PRV to compute HRV measures as well as to the interpretation of countless studies that have already been published based on the assumption that PRV is an acceptable surrogate for HRV.

Chapter III: Physiological Renal Sympathetic Vasomotion

Introduction

The maintenance of renal blood flow (RBF) is crucial for renal function, and the kidney is accordingly endowed with two powerful autoregulatory mechanisms, tubuloglomerular feedback (TGF) and the myogenic response (MR), which are widely appreciated as important controllers of RBF[126]. TGF is a mechanism that is unique to the kidney whereby changes in RBF-dependent NaCl flux at the end of the thick ascending limb are sensed by macula densa cells and transduced to modulate the diameter of the anatomically juxtaposed afferent arteriole. The MR, observed in other vascular beds but particularly strong in the kidney, senses changes in transmural pressure and responds by adjusting afferent arteriolar diameter to preserve constant RBF. Together these mechanisms maintain RBF and glomerular filtration rate over a wide range of perfusion pressures by modulating renal vascular conductance (RVC).

Conversely, the classic dogma maintains that the renal nerves are quiescent in the control of RBF in a normal, healthy state, causing vasoconstriction and a reduction in RBF only in response to experimental stimuli or in the setting of disease. This dogma, based mainly on steady-state measurements of mean RBF over minutes persists despite the fact that dynamic approaches have revealed the involvement of the renal nerves in the beat-to-beat dynamic regulation of RBF.

Steady-State Studies

The dogma that the renal nerves do not play a role in the physiological regulation of RBF developed over many decades. These studies made important contributions to our understanding of sympathetic neural control of renal function, but erred in assuming that steady-state (i.e. static or mean) measures of RBF could fully capture what we know today to be a dynamic process. To be fair, many of these studies preceded modern technologies for the assessment of RBF and relied on a much less complete understanding of renal autoregulation, and they should be viewed in this context. Today, the dogma rests primarily on findings from two sets of studies. We will briefly present the main findings of these studies.

One set of studies involves electrical stimulation of the renal nerves, which showed that low stimulation frequencies were sufficient to cause renin release, intermediate stimulation frequencies stimulated sodium reabsorption, and high stimulation frequencies were necessary to decrease RBF[127–130]. This data was interpreted to mean that the renal nerves play a role in basal renin release and sodium reabsorption, but not RBF control. We raise two problems with this line of thinking. The first problem is that steady-state electrical stimulation of the renal nerve does not reflect physiological control of RSNA in any way. Thus, such a paradigm, while powerful for addressing whether or not a parameter can be affected by RSNA, is ill-suited for addressing how the parameter is normally regulated by physiological sympathetic outflow. The second problem is that all of these studies looked at mean RBF averaged over minutes. As described previously, renal perfusion is also controlled by powerful autoregulatory mechanisms which are very effective in buffering changes in RBF over such a time span. Indeed, one study cited in support of this dogma reported that renal nerve stimulation results in an immediate drop in RBF, presumably the rapid effect of renal sympathetic vasoconstriction, which then recovers to pre-stimulation levels, presumably due to the compensatory vasodilatation effected by slower autoregulatory mechanisms[127]. Thus, these stimulation intensities do not correspond to the minimum threshold required to initiate renal vasoconstriction; instead, they represent the stimulation threshold at which the autoregulatory mechanisms fail.

The second set of studies supporting this dogma comes from some studies in chronically denervated dogs and rabbits that failed to detect a statistically significant difference between innervated and denervated kidneys[131–133]. We again raise two issues. The first is statistical; the second is physiological.

It is a fundamental aspect of statistical hypothesis testing to understand that the result obtained from an unpowered inference test is of little value. In the case that the null hypothesis is rejected, one does not know if no difference exists or if the test was simply underpowered, and it is wrong to simply assume the former. In this application: does removal of the renal nerves truly

not affect RBF or have previous tests simply been underpowered? Because of the high variability in RBF between kidneys, the latter is the case. A previous study of interest showed that the innervated (INV) kidney of a conscious dog has a mean PAH clearance of 187 mL/min with a standard deviation of 28 mL/min (n = 6)[133] while a decent-sized (n = 10) study showed that INV kidneys of conscious rabbits have a resting RBF with a mean of 50 mL/min and standard deviation of 15.8 mL/min[134]. If one considers a physiological difference in RBF to be a difference of 15% (i.e. the renal nerves decrease RVC by 15%), then one would need to perform a study with 64 dogs or 71 rabbits per group in order to have 80% power to detect a 15% change in mean RBF by two-tailed t-test with $\alpha = 0.05$ given the high degree of variability in basal RBF. No study of this size has ever been attempted, and the vast majority are not even within one order of magnitude of the requisite sample sizes. This critique also applies to the numerous studies where RBF was increased in denervated animals as underpowered studies are also prone to Type I (false positive) errors as well as Type II (false negative) errors.

The physiological argument is that, again, mean RBF is autoregulated, so the effect of removing the renal nerves does not reflect the sympathetic contribution to mean RBF as the powerful autoregulatory mechanisms exist to buffer such disturbances in mean RBF. Such an interpretation neglects not only the role of the renal nerves but also the strength of autoregulatory mechanisms. Since autoregulatory mechanisms can modulate RVC over two-fold[126], even a large sympathetic contribution to basal RVC could be completely masked by compensation by TGF and MR. Indeed, we regard findings from both electrical stimulation and chronic denervation studies as a testament to the power of renal autoregulation, rather than as evidence for the absence of physiological renal sympathetic control of RBF.

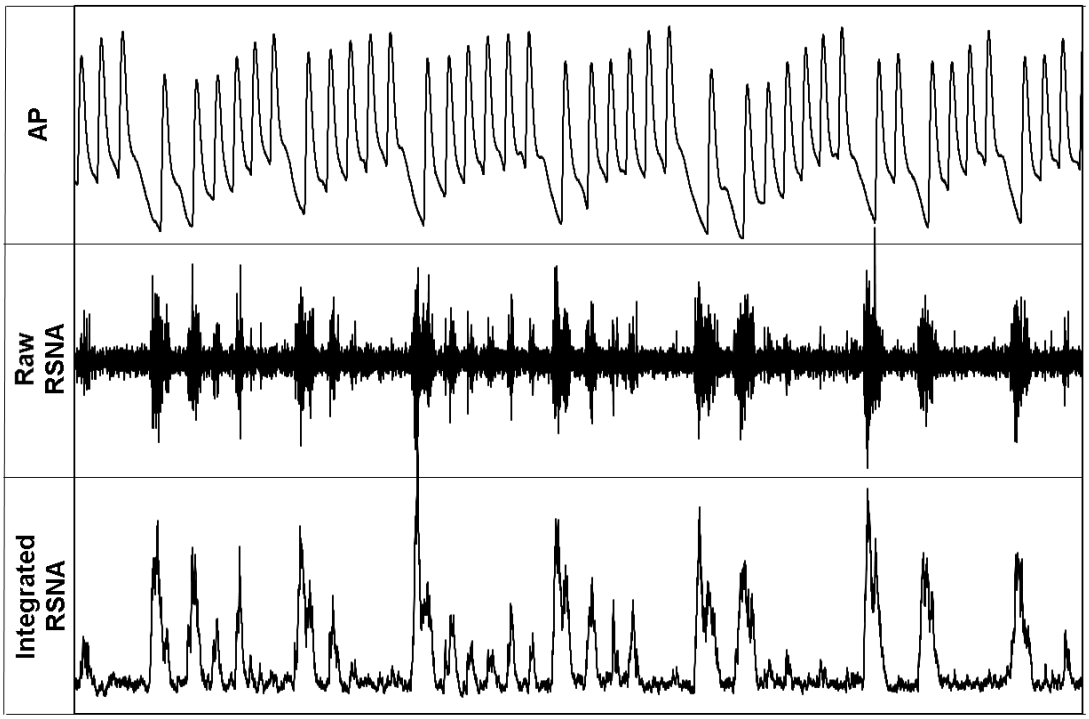

Figure 18 – RSNA is Dynamically Controlled

14-second recording of AP, raw RSNA, and integrated RSNA in a healthy, calmly resting rabbit one-week after RSNA electrode implantation. Note the dynamic nature of RSNA and the strong baroreflex control of RSNA, with the amplitude and incidence of RSNA bursts strongly corresponding to DBP.

Dynamic Approaches for a Dynamic Phenomenon

Following the diffusion of techniques allowing for chronic, conscious recordings of RSNA, the dynamic nature of RSNA became impossible to ignore. Figure 18 shows a 14-second sample of a recording from a conscious rabbit instrumented with RSNA electrodes that plainly demonstrates rhythmicity, beat-to-beat variability, and baroreflex control of RSNA, with lower diastolic pressures followed by large RSNA bursts. The inarguably dynamic nature of RSNA has inspired investigators to use dynamic approaches to study the neural control of renal function.

One common dynamic method of analysis for studying rhythmic physiological time series data is frequency analysis. This decomposes a physiologic signal occurring in time into its multiple frequencies, allowing quantification of the power of each rhythm. Figure 19 shows how a seemingly complex signal occurring in time can arise from a few simple rhythms and how frequency analysis facilitates the identification and quantification of these rhythms. Frequency analysis is a powerful tool for studying the control of physiological parameters as different physiological control mechanisms operate at different frequencies. By separating physiological mechanisms based on their operating frequencies, frequency analysis allows for their individual assessment as they regulate the physiological parameter of interest in vivo. Contrast this with classic, steady-state measures such as heart rate or renal vascular resistance which have no ability to assess the contributions of individual physiological mechanisms working together to regulate the parameter of interest. For example, if heart rate increases, one does not know if this is due to vagal withdrawal or cardiac sympatho-excitation or both; if renal vascular resistance increases, one does not know if this is mediated by sympathetic vasoconstriction, MR, or TGF. Frequency analysis offers us a window into the participation of individual physiological control mechanisms – although it is not without limitations.

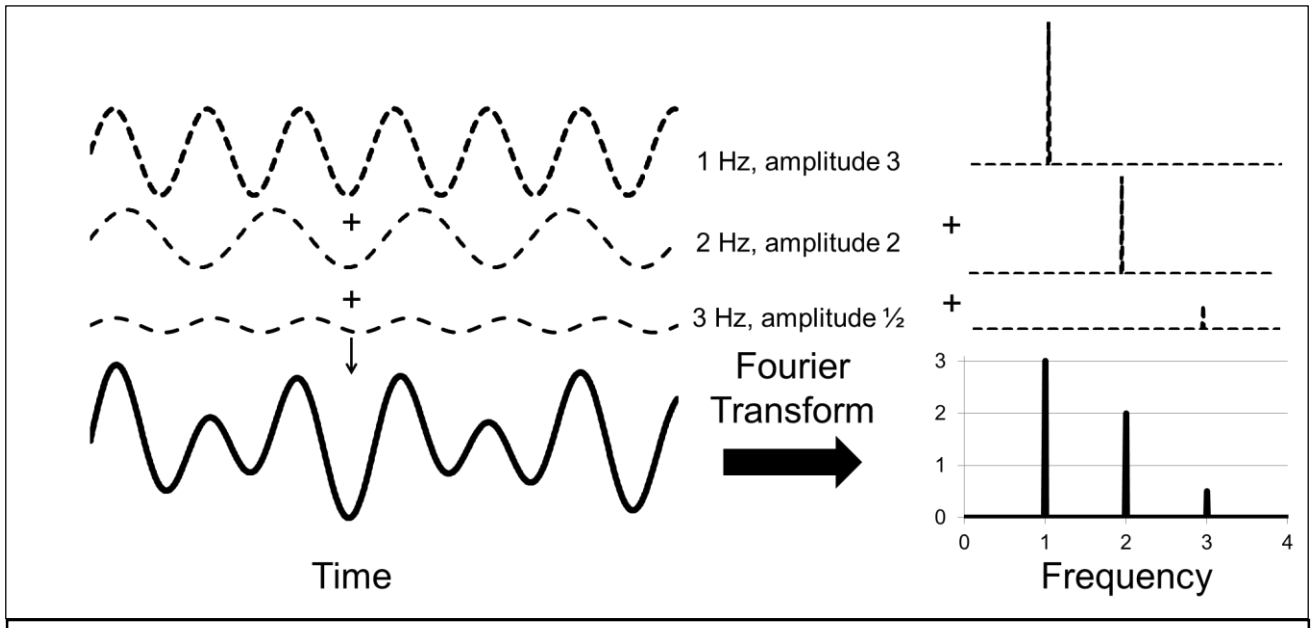

Figure 19 – Classic Frequency Analysis

A rhythmic signal which appears complex when viewed in time can be better understood after its transformation to the frequency domain. The composite waveform on the left is the simple addition of three other oscillations of different frequencies and amplitudes. When viewed in the frequency domain, the amplitude spectrum (right) reveals very clearly the frequencies of the underlying rhythms and their relative contributions (amplitudes). The phase spectrum (not shown) gives information about when each oscillation occurs (i.e. is at 0°).

One of these limitations is that the frequencies of different physiological mechanisms may overlap. Such is the case with heart rate: both parasympathetic and sympathetic inputs to the sinoatrial node contribute to low-frequency (LF) oscillations in heart rate variability. Fortunately, in the rabbit, rat, and mouse, the important dynamic controllers of the renal vasculature operate at distinct frequencies. The important autoregulatory mechanism of TGF operates between 0.02-0.08 Hz while MR operates between 0.08-0.20 Hz[126]. In the rabbit, LF sympathetic vasomotion occurs between 0.20 Hz to 0.46 Hz, and HF respiratory modulation occurs between 0.76 to 1.5 Hz[135]. If some aspects of this terminology are confusing (e.g., the fact that the so-called LF range is the second-highest frequency range), this is because we have united terminology from two different fields, renal autoregulation and autonomic neurophysiology. The frequency ranges for TGF and MR come from dynamic autoregulation studies, constituting what autonomic researchers (particularly in the field of heart rate variability) nebulously call the very-low frequency range[99]. The frequency ranges where LF sympathetic vasomotion and HF respiratory modulation occur come from autonomic studies and are frequently ignored or combined in studies of renal autoregulation.

Poiseuille's Law tells us that the steady-state flow through a rigid tube is equal to the perfusion pressure divided by the resistance of the tube. Thus, while the dynamic controllers of renal vascular resistance are important, so, too, is renal perfusion pressure. In healthy animals, the venous pressure is negligible, and thus AP can be used as a surrogate for perfusion pressure. This powerful physical relationship between AP and RBF allows for the study of the dynamic control of the renal vasculature.

Transfer Function Analysis of Renal Pressure-Flow

One way that the physical relationship between pressure and flow can be leveraged is by using a classic system identification approach called transfer function analysis. Transfer function analysis allows for the quantification of a dynamic input-output relationship, that is, an input-output

relationship as a function of frequency. This introduction focuses on studies in which transfer function analysis was used to identify the input-output relationship between AP and RBF for INV and denervated (DNx) kidneys.

Multiple approaches exist for transfer function analysis, but the most common method, and the one employed in all the studies reviewed here, is based on the Welch method of frequency analysis. The basics of this method are important to understanding the results and avoiding the pitfalls of this approach. The original arterial pressure and renal blood flow signals are divided into several, overlapping time windows. Each time window is multiplied by a window function, which reduces spurious edge effects caused by dividing the original signal into smaller time windows. The Fast Fourier Transform (FFT) of each contemporaneous AP and RBF time window is computed, converting the signals from the time domain to the frequency domain, where they are referred to as spectra and have both real and imaginary components. The RBF spectrum and the complex conjugate of the AP spectrum are multiplied to yield the cross-spectrum, which is then normalized by the AP power spectrum (i.e. magnitude squared of the FFT). This is averaged across all time windows to yield the final transfer function. Gain is calculated as the magnitude of the transfer function as a function of frequency. Phase shift is calculated as the inverse tangent of the imaginary and real parts of the transfer function for every frequency. Coherence is calculated by squaring the magnitude of the transfer function and normalizing by the RBF power spectrum.

The Welch method of transfer function analysis is widely employed for several reasons. First, averaging over multiple time windows greatly improves the signal-to-noise ratio; however, there is an important tradeoff between signal-to-noise and frequency resolution. Increasing the number of time windows accordingly decreases the length of each time window (e.g., deciding to chop a 600-second recording into 6 non-overlapped 100-second windows instead of 3 non-overlapped 200-second windows). This sacrifices frequency resolution as the frequency resolution of the Welch method equals the reciprocal of the time window length (e.g., 0.01 Hz for a 100-second window, 0.005 Hz for a 200-second window). As we show below, this tradeoff is important

in resolving physiology. Second, calculating the transfer function over multiple time windows allows one to assess the consistency of the linear input-output relationship over time, which is quantified as coherence. Methods that do not use multiple time windows cannot compute this physiologically significant measure.

When calculated carefully, the gain, phase shift, and coherence of the renal pressure-flow relationship have distinct physiological meanings and show a clear role for the renal nerves in the physiological control of RBF. However, it is important to understand that a one-size-fits-all approach to the Welch method is inappropriate; the parameters of the analysis must be chosen thoughtfully based on the physiological question at hand. We discuss herein the physiological meanings of gain, phase shift, and coherence in the context of the renal pressure-flow relationship and present what the contribution of the renal nerves to these three transfer function parameters tells us about their role in normal physiological control of RBF. At the same time, we touch on some signal processing issues which may explain discrepancies in the literature.

The data presented in the introduction come from rabbits that underwent either bilateral renal denervation (DDNx) or a sham procedure (INV)[53]. These rabbits were chronically instrumented with an AP telemeter and a RBF probe on the left renal artery. After a two-week recovery and acclimation to the procedure room, AP and RBF were recorded, and AP-RBF transfer function analysis was performed. We observed a clear sympathetic signature in the LF range where sympathetic vasomotion is prominent. The specific phase shift, gain, and coherence of this LF signature demonstrate how the renal nerves contribute to the physiological control of RBF.

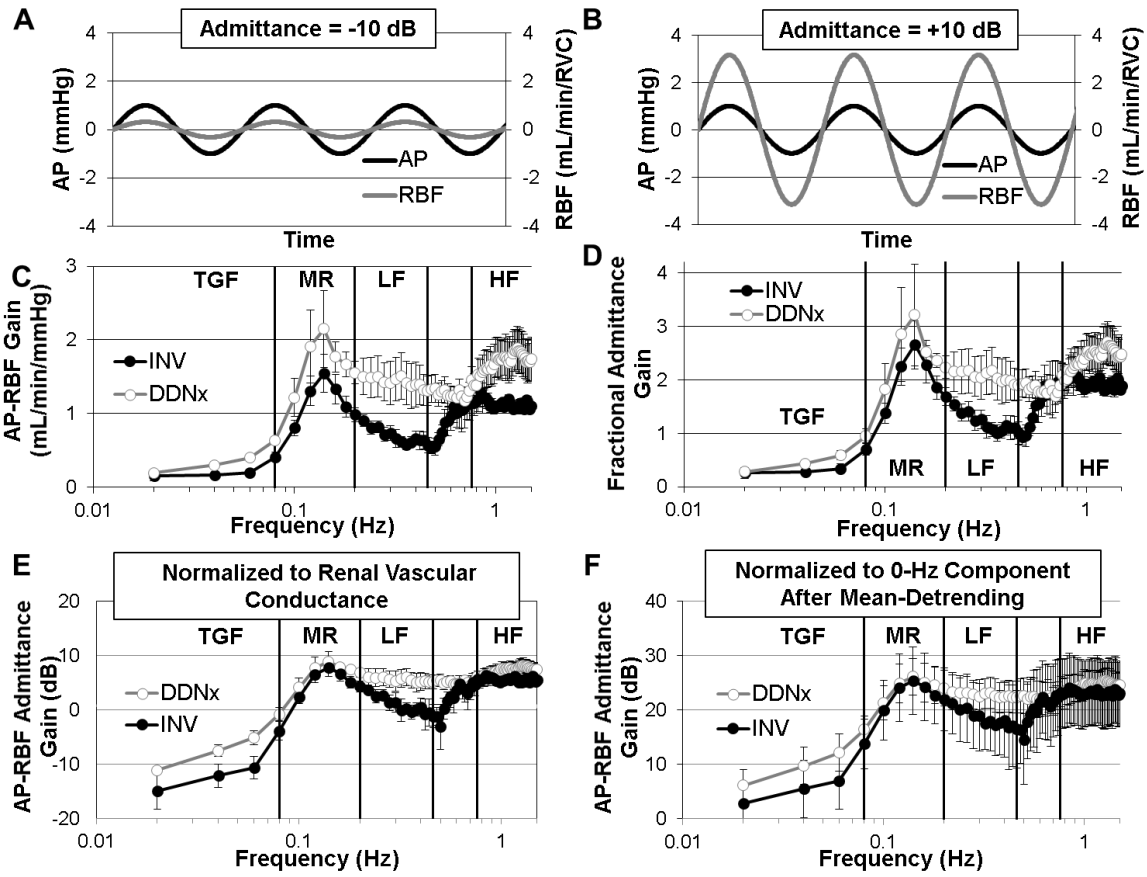

Figure 20 – Time-Invariant Renal Pressure-Flow Gain

Representative AP and RBF oscillations depicting (A) buffering of AP oscillations by active renal vascular control mechanisms resulting in negative admittance gain and (B) amplification of AP oscillations by passive renal arterial elastance resulting in positive admittance gain. INV kidneys show lower LF gain whether quantified as (C) raw gain, (D) fractional admittance gain, or (E) admittance gain. (F) Erroneous normalization abolishes the ability of transfer function analysis to demonstrate physiology, be it autoregulation or the contribution of the renal nerves.

Renal Pressure-Flow Gain

Transfer function gain quantifies *how much* an AP oscillation at a given frequency affects RBF. This is often normalized to the RVC, in which case it is called admittance gain and expressed as a unitless quantity (often specified as fractional gain) or in decibels (dB). The idea of this normalization is that it accounts for passive differences in the renal vasculature, thereby emphasizing the dynamic contributions of the physiological control mechanisms. An admittance gain less than 0 dB indicates that renal vascular control mechanisms are buffering the AP oscillations relative to what would be expected from Poiseuille's Law. Admittance gains greater than 0 dB, indicative of amplified transduction of pressure into flow, are believed to result due to the elastic nature of the renal artery.

From Figure 20B and C, one can appreciate that transfer function gain shows the strong autoregulatory capacity of the kidney. Renal autoregulation results in low gain below the operating frequencies of the autoregulatory mechanisms, highlighting the ability of these mechanisms to effectively buffer slow AP oscillations.

Measures of AP-RBF gain reveal that the renal nerves buffer the transduction of LF AP oscillations into RBF, whether calculated as raw gain, fractional admittance gain, or admittance gain in dB (Figure 20C-E). Other studies in the chronically denervated, conscious rabbit and acutely denervated, anesthetized rat have similarly shown that renal denervation increases raw gain and admittance gain, respectively, beyond the autoregulatory frequency range[116,136]. Thus, in both rats and rabbits, sympathetic control of RVC attenuates the effect of LF AP oscillations on RBF, consistent with a dynamic vasoconstrictive influence.

One notable study, however, failed to find an increase in admittance gain after acute renal denervation of healthy, anesthetized rats[137]. This may be due to how the admittance gain was normalized in this study. The authors performed mean subtraction, which eliminates the 0-Hz component, and then proceeded to normalize transfer function gain for all frequencies by the

calculated transfer function gain at 0 Hz. This is analogous to dividing by zero. Figure 20F shows the effect of such a procedure on our data. The erroneous normalization yields implausible data (e.g., admittance gain > 0 dB for all frequencies), and the effect of renal denervation on gain is completely abolished. This demonstrates an important point: *valid signal processing is important for accurate descriptions of physiology*.

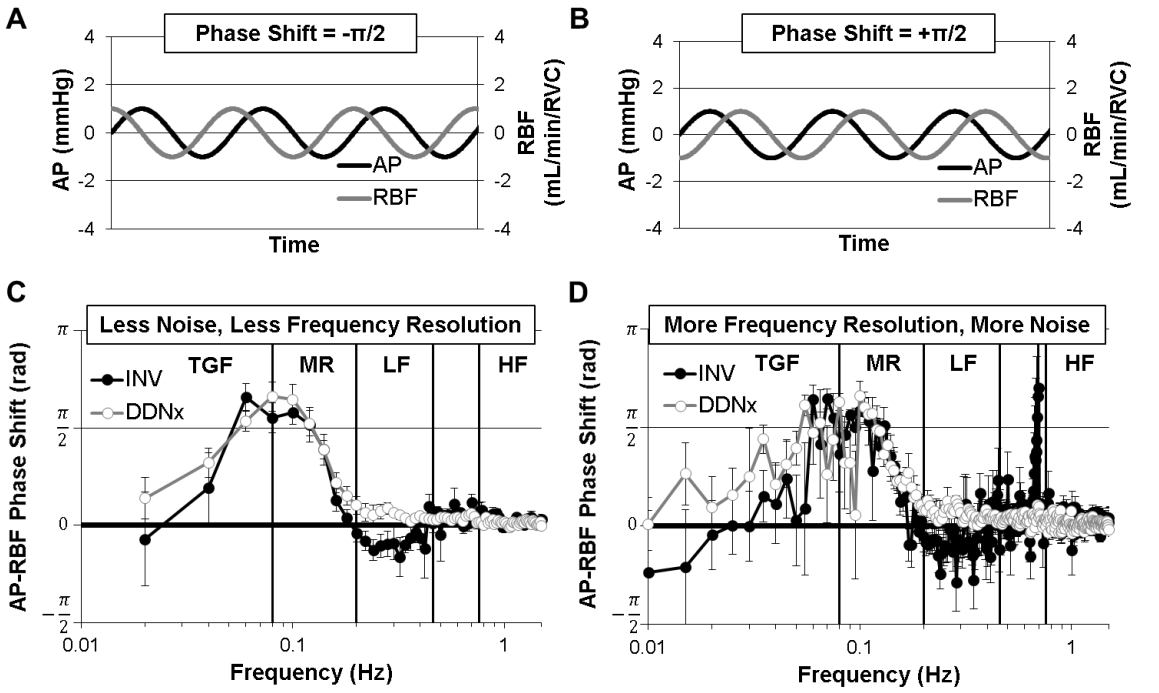

Figure 21 – Time-Invariant Renal Pressure-Flow Phase Shift

Representative depictions of (A) AP oscillations leading RBF oscillations as would be expected for an active control system sensing AP and modulating RVC (e.g., baroreflex) and (B) RBF oscillations leading AP oscillations as would be expected for an active control system sensing RBF and modulating RVC (e.g., autoregulation). (C) INV kidneys show a negative phase shift in the LF range which is abolished by renal denervation. (D) This difference is masked when longer time windows, which result in greater frequency resolution but poorer signal-to-noise, are used.

Renal Pressure-Flow Phase Shift

The AP-RBF transfer function phase shift quantifies *when* RBF oscillations relative to AP oscillations. If an AP oscillation occurs after an RBF oscillation, the phase shift is negative (Figure 21A). If an AP oscillation occurs before an RBF oscillation, the phase shift is positive (Figure 21B). Phase shift may be expressed as radians, in which case it is bounded between $-\pi$ and $+\pi$, or degrees, in which case it is bounded between -180 and 180, as one cannot distinguish between oscillations leading or lagging by more than one half-phase. The time lag between AP and RBF oscillations can be calculated as the product of the phase shift and the period of the oscillation of interest. If AP and RBF are synchronized (as depicted in Figure 20A and B), the phase shift is zero; this is the case for passive pressure-flow. When non-zero, phase shift also conveys important information about *causality* in a Granger sense (i.e. the cause occurs before the effect). Thus, when AP-RBF phase shift is positive, RBF oscillations precede AP oscillations, indicating the presence of an active control system which modulates RVC in response to RBF oscillations. Conversely, when AP-RBF phase shift is negative, AP oscillations precede RBF oscillations, indicating the presence of an active control system which modulates RVC in response to AP oscillations. While zero phase shift is characteristic of passive, Poiseuille flow, it can also arise from an AP-independent active control system (e.g., RSNA not under baroreflex control) which will contribute phase asynchrony, decreasing AP-RBF coherence despite the zero phase shift.

The contribution of sympathetic control to the renal pressure-flow phase shift can be appreciated in Figure 21. INV rabbits show a negative phase shift in the LF range, characteristic of baroreflex control of RVC. Renal denervation abolishes this negative phase shift, and instead the DDNx phase shift simply decays to zero, characteristic of passive pressure-flow. This matches well with the previous observation that resting RSNA is under strong baroreflex control (Figure 18). Interestingly, while our study was the first to report this effect as statistically significant, a clear trend for renal denervation to increase LF phase shift can be seen in studies in the conscious rabbit

and acutely denervated anesthetized rat[116,136]. The difference may arise from the signal processing parameters used in these studies, which were targeted at resolving autoregulatory frequency ranges. When we use similar parameters, increasing window length to 200 seconds and thereby decreasing the number of time windows, the noise in the LF range increases greatly and the effect of renal denervation is masked (Figure 21D).

Of course, variations in underlying RSNA are also undoubtedly important as RSNA which is not under baroreflex control may contribute to phase asynchrony instead of a negative phase shift. Further emphasizing this idea are reports that a negative AP-RBF phase shift is frequently observed but only in a subset of recordings (~1 in 7) from INV rats[138]. Because of the importance of the murine model, it is worth noting that a negative phase shift is also seen in the LF range of conscious, INV mice[139]. The fact that the renal vasculature is under sympathetic baroreflex control indicates that the renal nerves modulate RVC as part of a concerted systemic mechanism for modulating total peripheral resistance to maintain AP, not a local reflex which autoregulates RBF.

Renal Pressure-Flow Coherence

Strictly speaking, coherence measures the proportion of the variance in AP oscillations that is explained by a linear relationship with AP oscillations for all the time windows in the recording. Thus, coherence is a measure of the strength of the linear, time-invariant relationship between AP and RBF at a given frequency. Put more plainly, coherence is a quantification of *how consistently linear* the pressure-flow relationship is over time; it's the transfer function analog of the correlation coefficient and similarly ranges from zero to one. Figure 22A depicts an example of high coherence; the RBF oscillation follows the AP oscillation perfectly, amplifying the AP oscillation by 20% and lagging by a quarter phase. Figure 22B depicts low coherence; in this case, the RBF oscillation is a time-varying, nonlinear function of the AP oscillation.

Frequently, coherence is used as a quality control method, with a cut-off of 0.5 applied to determine whether the physiological control mechanism (e.g., TGF, MR) is effectively characterized by the estimated transfer function. Unfortunately, this is not an appropriate interpretation of coherence as the calculated coherence is not a characteristic, invariant quantity of the AP-RBF system or even of the individual recording; instead, it depends highly on the parameters used for the Welch method. To illustrate this point, we have calculated coherence for AP and RBF from INV rabbits, varying only the parameters of the Welch method. Specifically, 50%-overlapping windows of 50, 100, 200, 300, 400, and 600 seconds were used to yield 23, 11, 5, 3, 2, and 1 window for analysis. As one can see in Figure 22C and D, as the number of windows decreases, the coherence in the presence of active control mechanisms (i.e. in TGF, MR, and LF range) increases greatly. Obviously, the underlying physiological system has not changed, nor has the quality of the data, and, in a statistical sense, the lower coherence values with greater window number are offset by the increase in the degrees of freedom. It should be noted that although coherence can be calculated using less than three independent (i.e. non-overlapping) windows, calculations of coherence performed in this way are invalid.

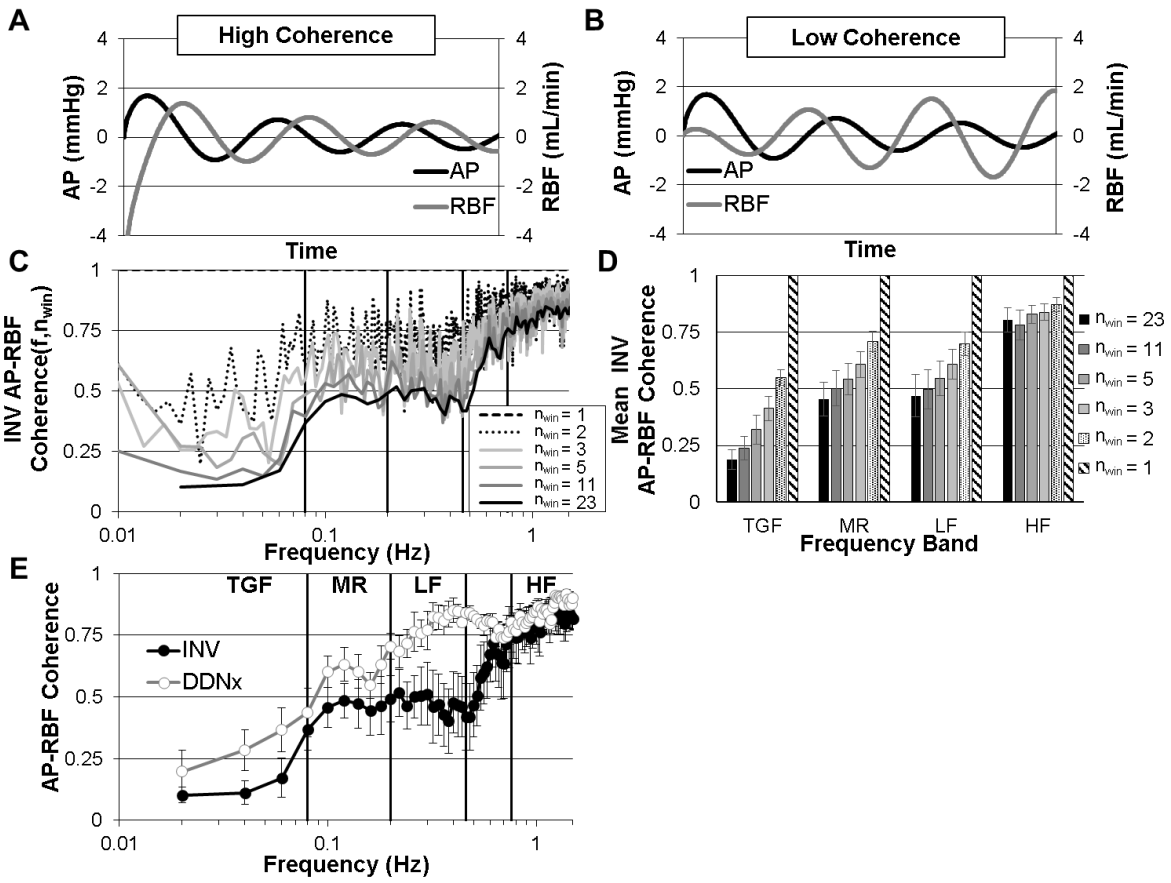

Figure 22 – Time-Invariant Renal Pressure-Flow Coherence

Representative depictions of (A) a RBF oscillation with high coherence to the AP oscillation and (B) a RBF oscillation with low coherence to the AP oscillation. (C) Coherence depends on signal processing parameters and decreases with increasing number of windows. (D) Mean coherence over frequency bands for TGF, MR, LF, and HF, demonstrating the sensitivity of coherence to signal processing parameters. (E) Renal denervation selectively increases AP-RBF coherence in the LF range.
n_{win}, number of 50% overlapping windows used for Welch method

Despite this misunderstanding, coherence provides immensely important insight into the renal-pressure flow relationship. In the absence of active modulation of RVC, the conditions for Poiseuille flow are well-met below the cardiac frequency, ensuring a linear pressure-flow relationship. Thus, any departures from the linear relationship between pressure and flow are indicative of active modulation of RVC. In other words, pressure-flow coherence is low in the presence of active control mechanisms (i.e. where pressure is not the only determinant of flow) and high where a passive pressure-flow relationship predominates. Accordingly, we urge the reader to consider AP-RBF coherence as accurate only when the calculated coherence is low in the autoregulatory frequency range and high in the high frequency (respiratory) range. In the absence of interventions which inhibit autoregulation, high coherence in the autoregulatory frequencies is highly indicative of incorrectly calculated coherence; low coherence in the respiratory frequency range may indicate poor data quality. The literature is unfortunately full of such examples.

With this understanding of coherence, the fact that the renal nerves contribute to the active control of RBF can be appreciated from Figure Figure 22E. In INV kidneys, AP-RBF coherence is low for the TGF, MR, and LF ranges, increasing rapidly to a passive maximum in the HF range. Renal denervation eliminates this LF active controller, and the coherence instead increases to the passive maximum over the LF range. This indicates that the renal nerves mediate active control of renal pressure-flow in the LF range. The other study which reports AP-RBF coherence similarly found that renal denervation increases coherence beyond the autoregulatory frequencies, again emphasizing that the renal nerves are an important contributor to the rapid control of RBF[116].

Summary of the Sympathetic Regulation of Renal Pressure-Flow

In summary, the renal sympathetic control buffers the transduction of LF AP oscillations to RBF, exerts LF baroreflex control over RVC, and decreases LF renal-pressure flow coherence. The integration of these three findings is important to fully understand renal sympathetic vascular control. It may seem counterintuitive that a baroreflex controller of pressure-flow would decrease

pressure-flow gain; indeed, some have stated that a baroreflex controller would increase pressure-flow gain (although all experimental evidence has shown the opposite to be true). Consider the case where AP rises above the set point, initiating a baroreflex-mediated decrease in total vascular conductance. A decrease in RVC in response to increased AP would result in amplification of AP oscillations and thus high AP-RBF gain.

In reality, this is not what happens because the sympathetic nervous system relies predominantly on α_1-adrenergic-mediated vasoconstriction to modulate total peripheral conductance and RVC. Thus, to be able to respond to both increases and decreases in AP, the sympathetic nervous system must provide some basal level of systemic vasoconstriction. This rhythmic sympathetic vasoconstriction gives rise to LF AP oscillations known as the Mayer waves, which are minor and variable in an unstressed, healthy animal but increase manifold when strong hemodynamic stimuli like hemorrhage and hypoxia drive global LF sympathetic synchronization[140]. It is this rhythmic vasoconstriction which explains the decreased AP-RBF LF gain in INV kidneys. In response to an increase in pressure, this rhythmic vasoconstriction is withdrawn, contributing to the baroreflex-mediated increase in total vascular conductance and resulting in a relative elevation in AP-RBF gain. In the case that the nerves are completely silenced by the increase in AP, the AP-RBF gain in the LF range will reach passive AP-RBF gain.

This same variability in the underlying RSNA explains the decreased LF coherence observed in INV rabbits that is restored by renal denervation. The sympathetic rhythms generating renal sympathetic vasomotion, sometimes participating in the generation of LF AP oscillations and other times responding to them, sometimes exerting strong vasoconstriction in response to decreased AP and going quiescent in response to increased AP, decrease the consistency of the AP-RBF relationship. Moreover, the fact that RSNA can be entrained by other reflexes including the central/peripheral chemoreceptor reflexes, cardiopulmonary baroreflex, and the cardiac sympathetic afferent reflex, further contributes to the variability in the AP-RBF relationship.

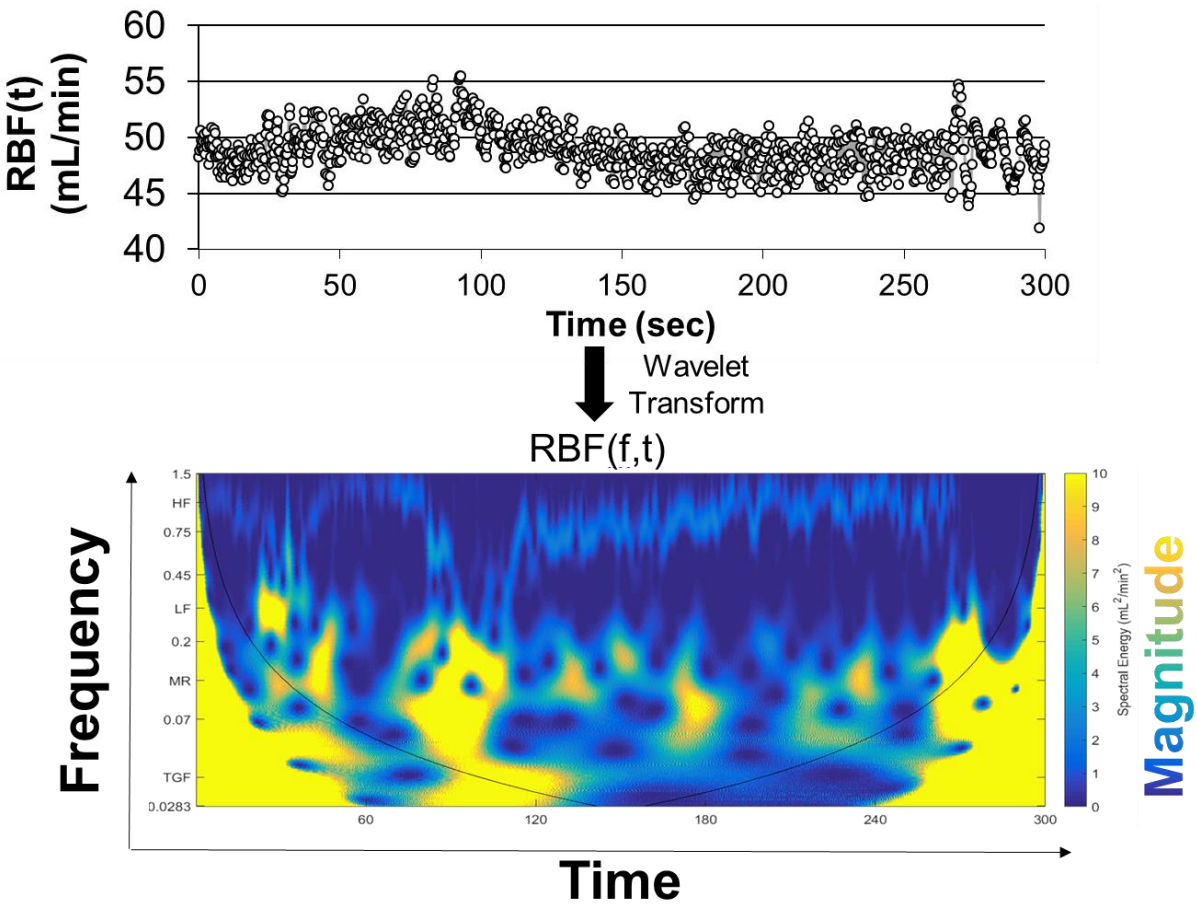

Figure 23 – Time-Frequency Analysis

Time-frequency analysis allows for the estimation of spectral energy localized in time. Performing a wavelet transform with multiple scales results in a three-dimensional plot with the square-magnitude of the spectral energy for each frequency encoded as color, with yellow being high energy and blue being low energy. The black lines indicate the border of the edge-affected time points; everything outside these lines is affected by edges because the time series isn't infinite and should be ignored.

Time-Varying Transfer Function Analysis of Renal Pressure-Flow

We have shown that optimal signal processing is crucial in order to accurately characterize the underlying physiology of the renal pressure-flow system, and, while the Welch method has several advantages in terms of signal-to-noise ratio, it also has a marked disadvantage: all information on when oscillations occur is lost. Time-frequency analysis allows for the variance (i.e. power) of a signal to be localized in both time and frequency. This results in a three-dimensional (3D) plot in which the distribution of the signal variance is displayed as spectral energy in time-frequency space (Figure 23). As the previous section describes, different entrainment of underlying RSNA may explain disparate results in previous studies of renal pressure-flow. For example, LF baroreflex behavior may be visible in an INV kidney but only for a portion of the recording, which will be lost as multiple windows are averaged together. Thus, using time-frequency analysis to create a time-varying renal pressure-flow transfer function may allow for characterization not only of the predominant behavior at each frequency but also the distribution of the pressure-flow transfer function behavior over time.

While one can find many examples of time-frequency analysis applied to cardiovascular variability in the literature, one reason why it the technique remains much less popular than frequency analysis is because it is difficult to leverage the additional data for across-time comparisons. For example, during a baseline recording, there is little rationale to compare a 0.3 Hz oscillation occurring 2.5 minutes after the beginning of one recording to a 0.3 Hz oscillation occurring 2.5 minutes after the beginning of a different recording. Thus, when time-frequency analysis is performed, the measures are often simply averaged over time, largely defeating the purpose of time-frequency analysis and yielding a result very similar to that obtained by the Welch method.

One approach to this issue is to leverage the fact that there are two kidneys by denervating one and leaving the nerves in-tact contralaterally. Now, both time and perfusion pressure are

directly comparable for an INV and a DNx kidney, facilitating powerful comparisons and eliminating many potential confounds. Between-subjects comparisons can also be facilitated using occurrence histograms, with time that the INV and DNx kidney spend between certain values of admittance gain, phase shift, and coherence values calculated and compared.

Hypothesis

We hypothesized that time-varying transfer function analysis of unilaterally denervated rabbits instrumented with bilateral renal flow probes would elegantly demonstrate LF renal sympathetic vasomotion in the INV kidney and passive pressure-flow in the DNx kidney.

Methods

Animals

Experiments were carried out on male New Zealand White rabbits ranging in weight from 3.2 to 4.5 kg (Charles River Laboratories, International, Wilmington, MA). All experiments were reviewed and approved by the University of Nebraska Medical Center Institutional Animal Care and Use Committee and carried out in accordance with the Guide for the Care and Use of Laboratory Animals of the National Institutes of Health. Rabbits were housed in individual cages in a temperature-controlled room (23º C) with a 12:12 hour light-dark cycle (lights on at 07:00, lights off at 19:00). Rabbits were given ad libitum access to reverse-osmosis purified water and high-fiber rabbit chow (Teklad 2031, Envigo RMS, Indianapolis, IN).

Instrumentation

Each rabbit was instrumented with an AP telemetry and bilateral renal flow probes. After induction with ketamine and xylazine and under isoflurane anesthesia and positive pressure ventilation, a radiotelemetry device was implanted in the right femoral artery in order to record AP. This was done by performing a femoral cut-down and threading a catheter attached to a

radiotelemetry transducer (PA-C40, Data Sciences International, St. Paul, MN) into the abdominal aorta. Rabbits then underwent bilateral renal flow probe instrumentation with unilateral renal denervation. The kidney to be denervated was randomized (randomization seed #19423 from randomization.com was used). During this surgery, bilateral flank incisions were made, and the renal arteries and veins were carefully dissected using glass rods. The kidney randomized to be denervated had its artery stripped of all visible neural tissue. A 2-mm renal flow probe (Transonics Systems, Inc., Ithaca, NY) was secured around both renal arteries using a piece of Silastic sheeting and 4-0 silk suture. The probe cable was tunneled beneath the skin and exited in the midscapular region of the rabbit. After each surgery, rabbits received a single dose of buprenorphine (0.02 mg/kg subcutaneously), a three-day course of antibiotics (Baytril, 22.7 mg/day subcutaneously, Bayer Health Care, Shawnee Mission, KS) and three days of pain control via a transdermal patch (fentanyl, 25µg/hr, Mylan Pharmaceuticals, Morgantown, WV). Prior to data collection, rabbits recovered for at least 14 days.

Acclimation

Prior to data collection, rabbits were acclimated to the experimental procedure room and Plexiglass experiment box. The rabbits were handled daily until signs of stress were absent and rabbits were accustomed to resting calmly in the experiment box in the procedure room. This involved a minimum of five, 1-hour procedure room acclimation sessions.

Baseline Recordings

After this acclimation period, rabbits underwent data collection for subsequent analysis. AP and bilateral RBF were digitized at 1 kHz via a PowerLab system (AD Instruments, Colorado Springs, CO) for at least 1 hour. This recording was used to validate that the rabbit's instrumentation is functioning properly. Rabbits were to be excluded if their baseline hemodynamics assessed by their instrumentation failed to meet basic inclusion criteria. These criteria were pre-defined in an Open Science Framework pre-registration which will be released from embargo when the study is

published in manuscript form. In one case, a rabbit was excluded as he had chewed off one of his flow probes.

Nasopharyngeal Reflex

At the end of this data collection, the nasopharyngeal reflex was invoked. Cigarette smoke was drawn through its filter into a 60 mL syringe so that the entire syringe is opaque with smoke. The smoke was then gently delivered to the rabbit's face over 10 seconds, resulting in near maximal autonomic activation. This renal vasoconstrictive response was used to validate completeness of denervation and to ensure that the intact kidney is indeed innervated. Rabbits were excluded if the RVC of the DNx kidney decreases >30% or if the RBF of the INV kidney remained >1 mL/min. The INV kidney of one rabbit failed to decrease below 15 mL/min, indicating significant partial denervation during renal flow probe implantation, and this rabbit was excluded from analysis. These exclusion criteria were pre-defined in an Open Science Framework pre-registration which will be released from embargo when the study is published in manuscript form.

Euthanasia

Before sacrifice and tissue collection, the rabbits were anesthetized with ketamine (35 mg/kg) and xylazine (5.8 mg/kg) intramuscular injection. After local infiltrations of bupivicaine, a right femoral cutdown was performed, and the left femoral artery was cannulated with a Millar pressure transducer. The difference between the chronically implanted telemetry and the acutely introduced transducer was used to calibrate AP from the previously collected conscious data. Kidneys were collected for molecular validation of denervation.

Analysis

Artifact-free, 10-minute segments from these recordings were used to perform all subsequent analysis. All sections of data were relatively stationary with regard to AP, right and left RBF, and HR. Prior to data analysis by Peter Ricci Pellegrino, the data was blinded by Alicia Marie

Schiller. This was accomplished by saving a de-identified data file without the data segment containing the nasopharyngeal reflex. Data analysis was performed as follows.

In order to eliminate time delays, the bilateral RBF signals were synchronized to AP using the maximum of the cross-correlation. Pulse onsets were detected using the maximum of the 2nd derivative of the AP signal and manually screened for artifacts. Pulsatile AP and bilateral RBF signals were averaged over each pulse, yielding beat-to-beat data used for analysis. Mean hemodynamic parameters, including HR, mean AP, left and right mean RBF, and left and right mean RVC were calculated from this beat-to-beat data.

Time-varying transfer function analysis was performed using MATLAB (MathWorks, Inc., Natick, MA). The beat-to-beat data were linearly interpolated at 5.12 Hz. Time-frequency analysis of each signal was performed using a continuous complex Morlet wavelet with scales calculated to yield 251 pseudofrequencies ranging from 0.02 Hz and 1.5 Hz that are linearly spaced when plotted logarithmically. Pseudofrequencies were grouped into bands based on previous studies in rabbits which have shown that TGF operates between 0.02-0.08 Hz, the myogenic response operates between 0.08-0.20 Hz, the LF band where sympathetic vasomotion gives rise to the so-called Mayer waves ranges from 0.20-0.45 Hz, and the HF band encompassing the respiratory frequency ranges from 0.75-1.5 Hz. The linear, time-varying transfer function was calculated for each kidney by computing the AP-RBF cross-spectrum and normalizing by the square of the AP spectral energy for every pseudofrequency and every time point. Gain is the amplitude of this time-varying transfer function; phase shift is the angle of the real and imaginary components (i.e. the inverse tangent of the quotient of the imaginary component divided by the real component of the time-varying transfer function). Admittance gain in decibels was calculated by normalizing the gain by RVC, computing the base-10 logarithm of this normalized gain, and multiplying this logarithm by 20. Standard time-varying coherence will use smoothing window lengths that yield three independent oscillations for each pseudofrequency (i.e. three divided by the pseudofrequency). Points in the time-pseudofrequency space influenced by edge effects were

excluded from analysis. Phase shift, admittance gain, and coherence time variability were calculated as both the standard deviation and interquartile range for each pseudofrequency over the course of the recording. Occurrence plots of phase shift, admittance gain, and coherence were calculated.

These parameters were calculated for each recording and visualized by Peter Ricci Pellegrino before unblinding of the data by Alicia Marie Schiller.

Null hypothesis testing will be performed after unblinding of the second group of rabbits which has not yet been completed. This will be performed by RM-ANOVA with Greenhouse-Geisser corrections for sphericity with P values < 0.05 considered statistically significant. Because much of the occurrence data described is best visualized as a heat map (3D plot), the data is presented as mean data for innervated and denervated kidneys with t-statistics and P values computed for each point in the x-y space in order to convey directionality, magnitude, and consistency of innervated/denervated renal pressure-flow differences. These P values are descriptive only and are not intended to convey statistical significance per se.

Additional testing will be performed for data averaged across frequency bands. When the RM-ANOVA for data averaged across frequency bands shows a statistically significant effect of renal innervation, paired t-tests will be performed between INV and DNx for each frequency band. These paired t-tests will be one-tailed (H0: DNx < INV for measures of variability, H0: DNx > INV for measures of coherence), and a Sidak correction for multiple comparisons will be applied to the standard alpha = 0.05 (i.e., with 4 frequency bands, the critical P value = 0.01274). Even when the RM-ANOVA for data averaged across frequency bands does not show a significant effect of renal innervation, the LF band, where sympathetic vasomotion is prominent, will be tested for differences using a paired, two-tailed t-test between INV and DNx with alpha = 0.05.

Table 12 – Mean Measures of Basal Hemodynamics for Unilaterally Denervated Rabbits

Hemodynamic Measure	
AP (mm Hg)	80.1 ± 3.3
INV RBF (mL/min)	39.8 ± 5.3
DNx RBF (mL/min	47.3 ± 3.0
HR	212 ± 9

Values are displayed as mean ± SEM.
n = 5

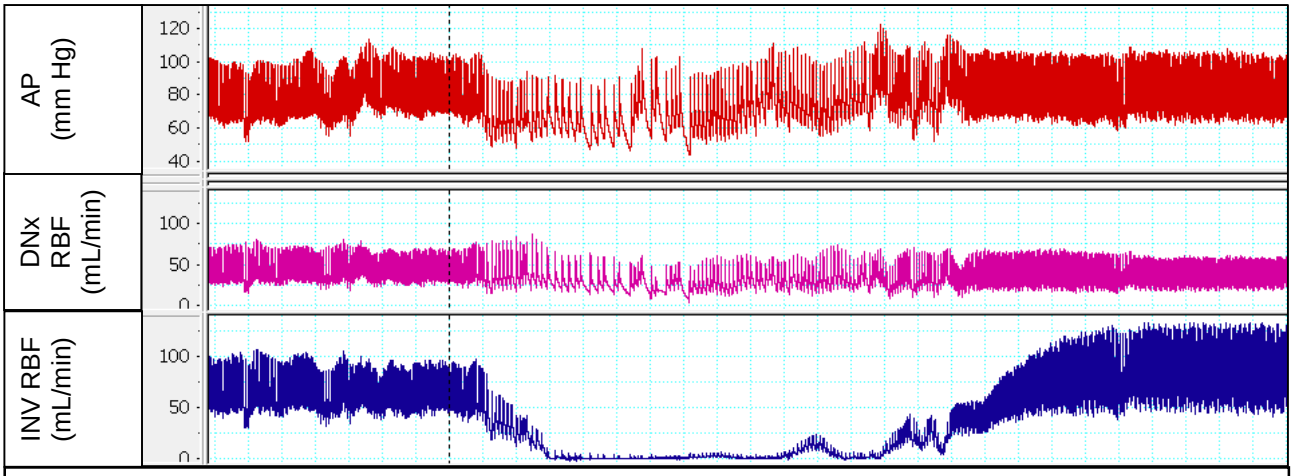

Figure 24 – Representative Tracing of the Nasopharyngeal Reflex

The robust autonomic activation elicited by the nasopharyngeal reflex (dotted line) results in a robust bradycardia (visible best in AP and DNx RBF) and near-maximal renal sympathetic vasoconstriction. DNx RBF is unchanged while INV RBF goes to zero.

Results

Mean Measures of Baseline Hemodynamics

Baseline means for AP, RBF to the INV kidney, RBF to the DNx kidney, and HR are shown in Table 12. Importantly, the difference between INV and DNx RBF was not statistically significant ($P_{Sx} = 0.30$).

Nasopharyngeal Reflex

Elicitation of the nasopharyngeal reflex results in a large parasympathetic and sympathetic activation. This sympathetic activation drives RBF in the INV kidney below 1 mL/min while the RBF to the DNx kidney remains relatively unchanged (Figure 23). This response was used to functionally validate innervation status of the kidney. The RBF of the INV kidney of one rabbit failed to fall below 15 mL/min despite multiple attempts on different days, indicating partial denervation of the kidney during RBF probe implant. Per the pre-registered exclusion criteria, this rabbit was excluded from all subsequent analysis.

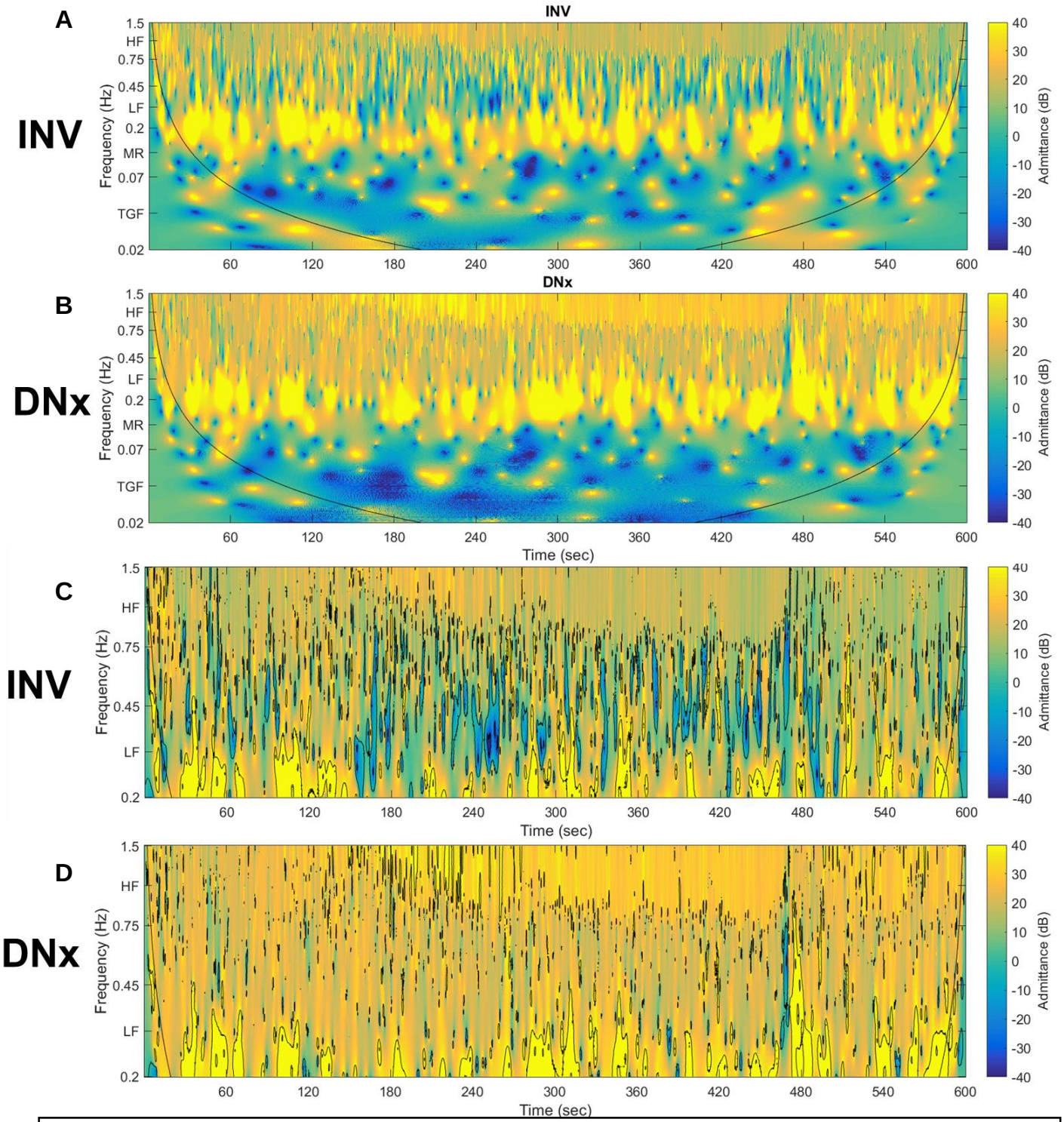

Figure 25 – Representative Time-Varying AP-RBF Admittance Gain Plots

Representative time-varying admittance gain plots are shown for the pressure-flow to an (A) INV kidney and (B) DNx kidney in the same rabbit. Focusing on the LF and HF ranges, the (C) INV kidney shows blue LF vasoconstriction which is absent in the (D) DNx kidney. Black contour lines were added to emphasize the LF variability (i.e. vasomotion) effected by the renal nerves and absent after denervation. Also appreciate the exquisite similarity in the HF range by virtue of their identical perfusion pressure and predominance of passive pressure-flow in this frequency range.

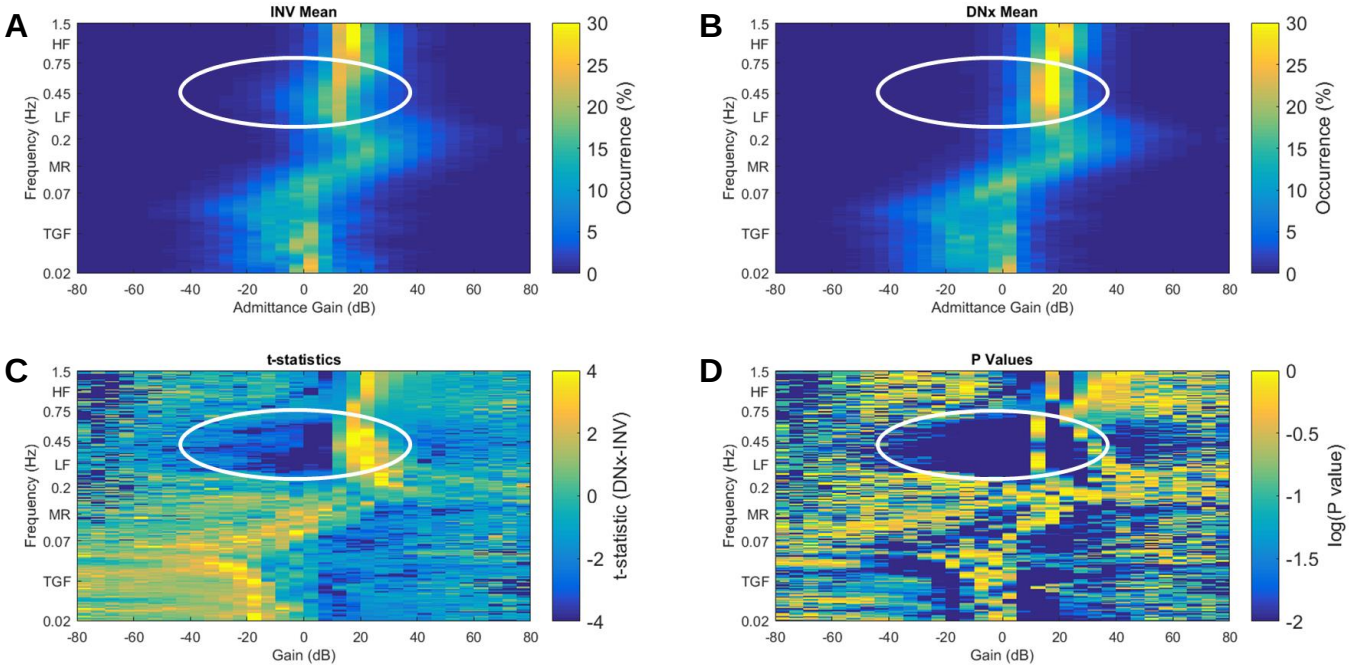

Figure 26 – Sympathetic Signature in AP-RBF Admittance Gain Behavior

Mean AP-RBF admittance gain occurrence for bins of with 5 dB for (A) INV and (B) DNx kidneys. (C) T-statistics and (D) P values indicate a specific sympathetic signature resulting in low gain occurrence in the LF range, consistent with a rapid, vasoconstrictive influence which is eliminated by denervation. n = 5

Time-Varying Renal Pressure-Flow Admittance Gain

A representative tracing of the admittance gain reveals a time-varying, vasoconstrictive influence in the LF range of the INV kidney that is absent in the DNx kidney (Figure 25). A similar effect was seen in all INV kidneys but never in DNx kidneys (Figure 26). Thus, this fast vasoconstriction is a part of a specific renal sympathetic pressure-flow signature. Moreover, the increased LF variability over time, while visible in Figure 25 and Figure 26, is explicitly quantified in Figure 27. Whether quantified as the standard deviation or interquartile range for each frequency over time, INV kidneys have higher LF admittance gain variability than their DNx counterparts despite the exact same perfusion pressure. In summary, time-varying renal pressure-flow admittance shows clearly that the renal nerves exert a time-varying rhythmic vasoconstrictive influence in healthy, conscious rabbits. This provides strong evidence that renal sympathetic vasomotion is a physiological phenomenon.

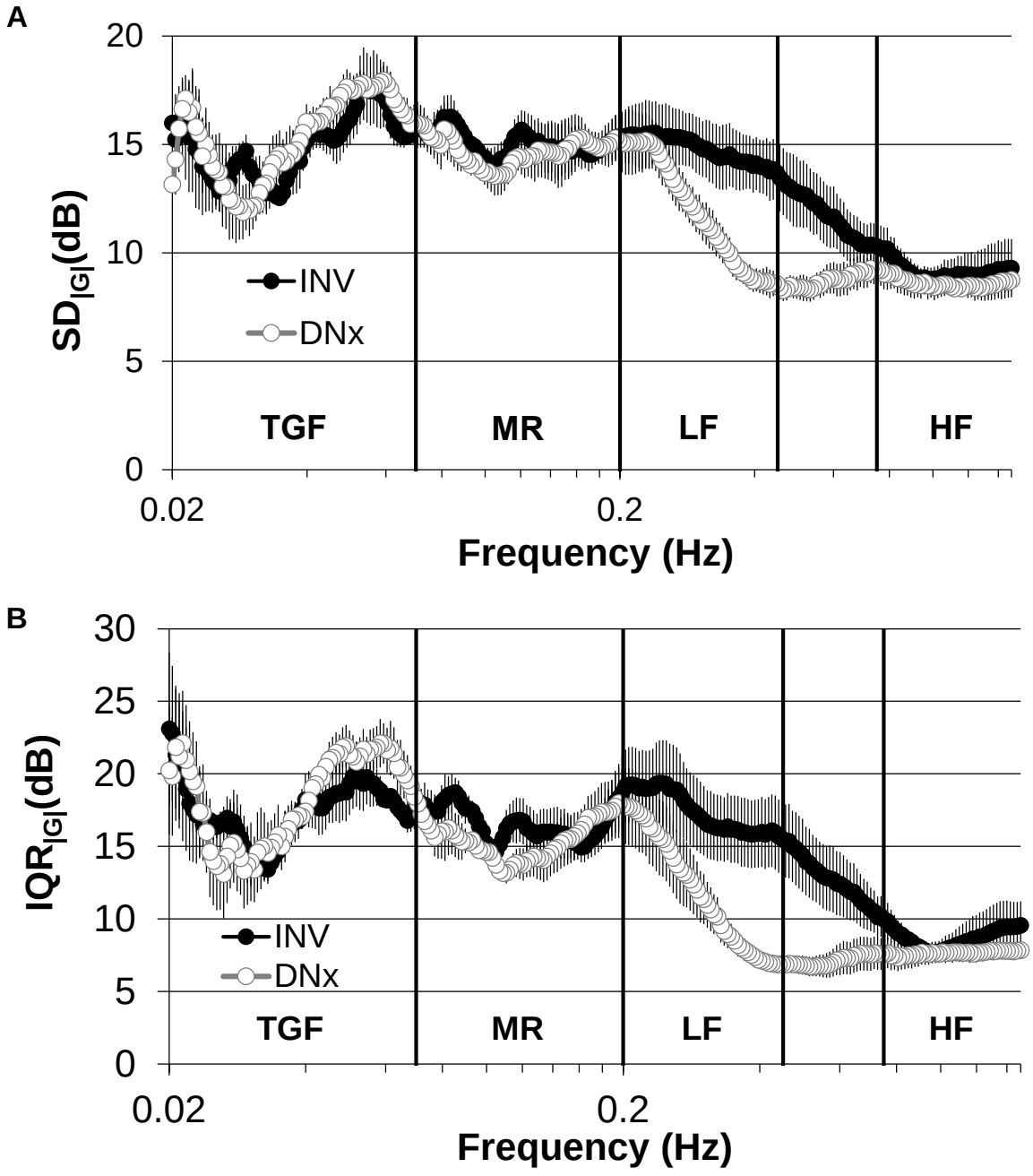

Figure 27 – Renal Pressure-Flow Admittance Gain Time-Variability

Whether calculated as (A) standard deviation or (B) interquartile range, admittance gain time-variability is higher for INV kidneys compared to DNx kidneys, indicating that the renal nerves exert time-varying modulation of renal vascular tone. SD, standard deviation; IQR, interquartile range; |G|, admittance gain

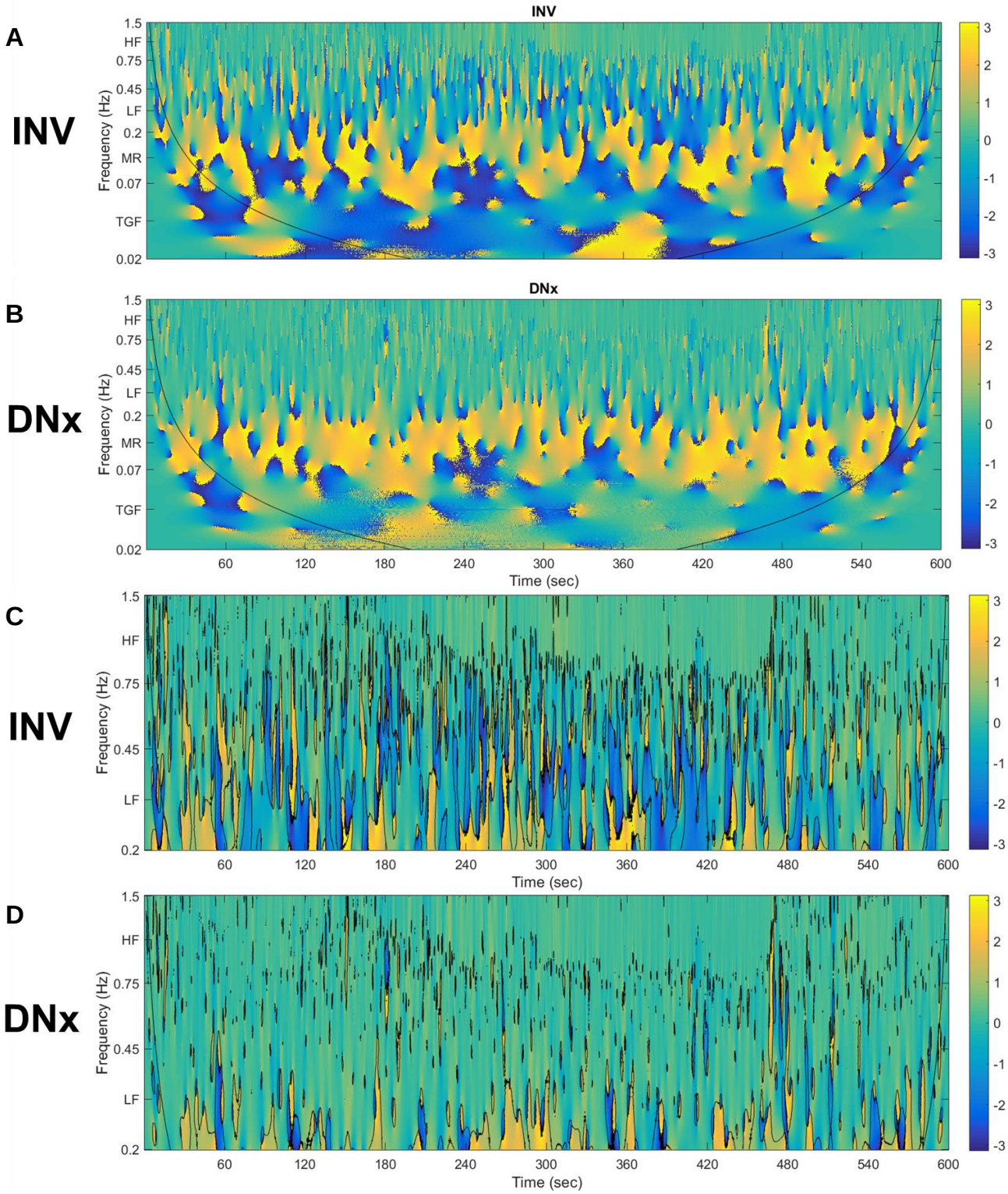

Figure 28 – Representative Time-Varying AP-RBF Phase Shift Plots

Representative time-varying phase shift plots are shown for the pressure-flow to an (A) INV kidney and (B) DNx kidney in the same rabbit. Focusing on the LF and HF ranges, the (C) INV kidney shows blue baroreflex control which is absent in the (D) DNx kidney. Black contour lines were added to emphasize the LF variability (i.e. vasomotion) effected by the renal nerves and absent after denervation. Also appreciate the exquisite similarity in the HF range by virtue of their identical perfusion pressure and the predominance of passive pressure-flow in this frequency range.

Time-Varying Renal Pressure-Flow Phase Shift

A representative tracing of the pressure-flow phase shift reveals a time-varying, baroreflex influence in the LF range of the INV kidney which is absent in the DNx kidney (Figure 28). Interestingly, all INV kidneys showed increased phase asynchrony (i.e. phase shift $\neq 0$) but not all showed a clear baroreflex predominance as was shown in the prior data set from unilaterally instrumented INV rabbits (Figure 29). This indicates that, while there is a strong role for the arterial baroreflex in sympathetic control of RBF, other AP-independent sympathetic rhythms are also important effectors of renal sympathetic vasomotion. As for admittance gain, measures of pressure-flow phase shift time-variability are elevated for the INV kidney compared to the DNx kidney, providing further evidence for the importance of the time-varying approach to pressure-flow analysis when attempting to understand inherently time-varying physiological phenomena (Figure 30).

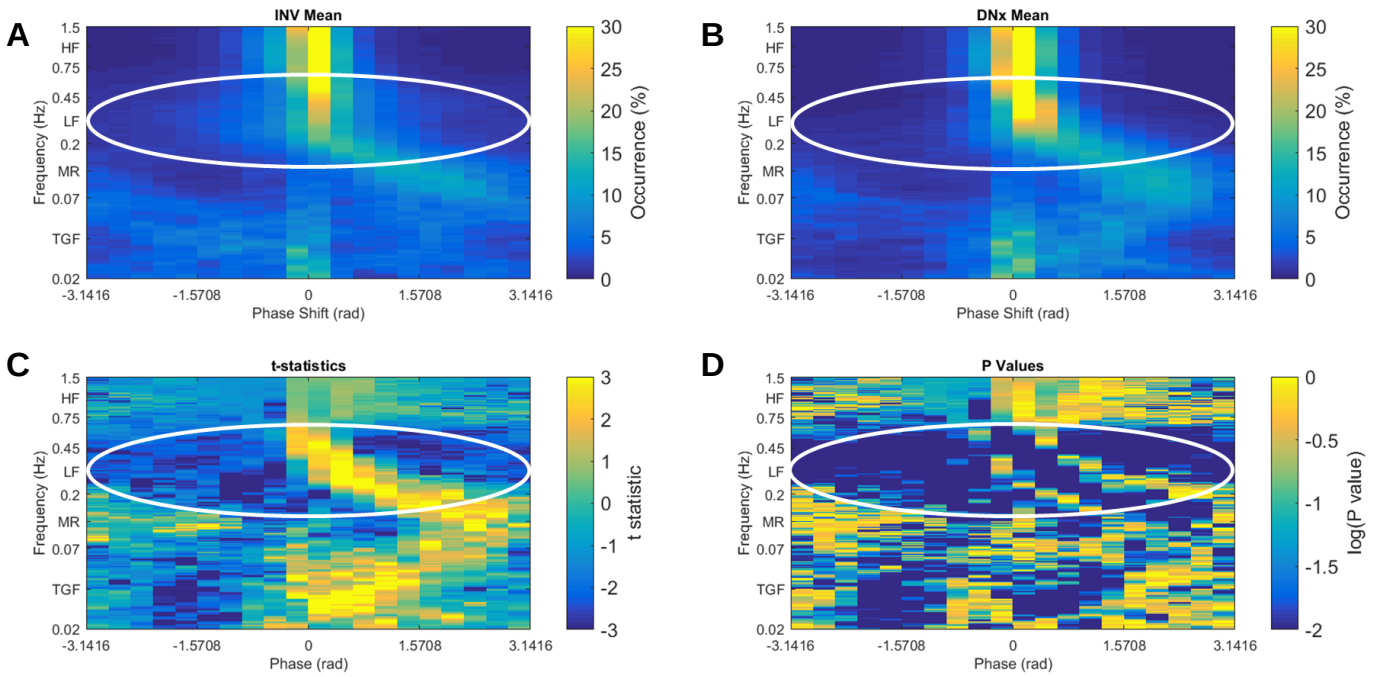

Figure 29 – Sympathetic Signature in AP-RBF Phase Shift Behavior

Mean AP-RBF phase shift occurrence for bins of width π/10 for (A) INV and (B) DNx kidneys. (C) T-statistics and (D) P values indicate a specific sympathetic signature resulting in phase asynchrony in the LF range, consistent with an active, asynchronous vascular control mechanism which is eliminated by denervation. n = 5

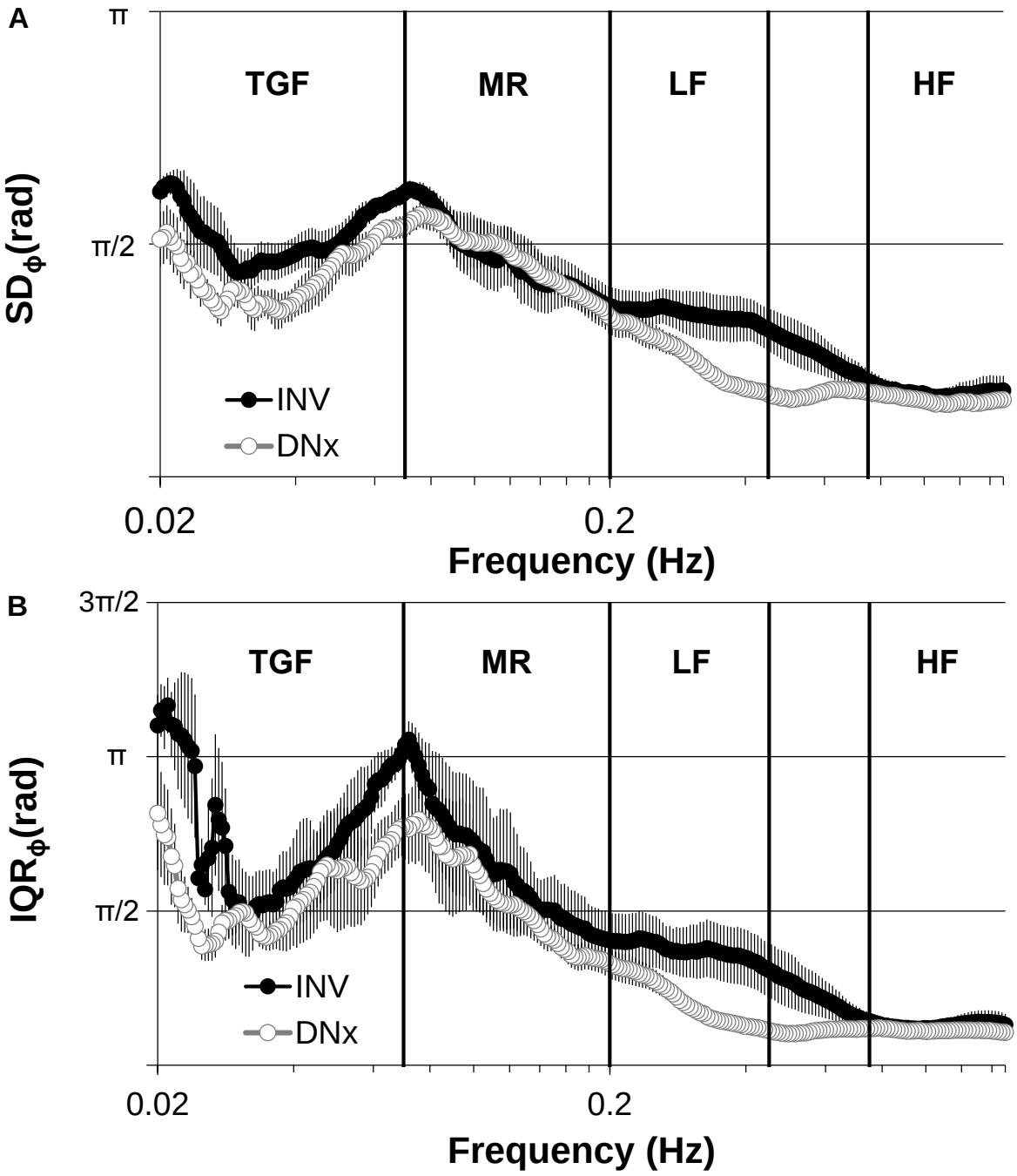

Figure 30 – Renal Pressure-Flow Phase Shift Time-Variability

Whether calculated as (A) standard deviation or (B) interquartile range, pressure-flow phase shift time-variability is higher for INV kidneys compared to DNx kidneys, indicating that the renal nerves exert time-varying modulation of renal vascular tone. SD, standard deviation; IQR, interquartile range; ϕ, admittance gain

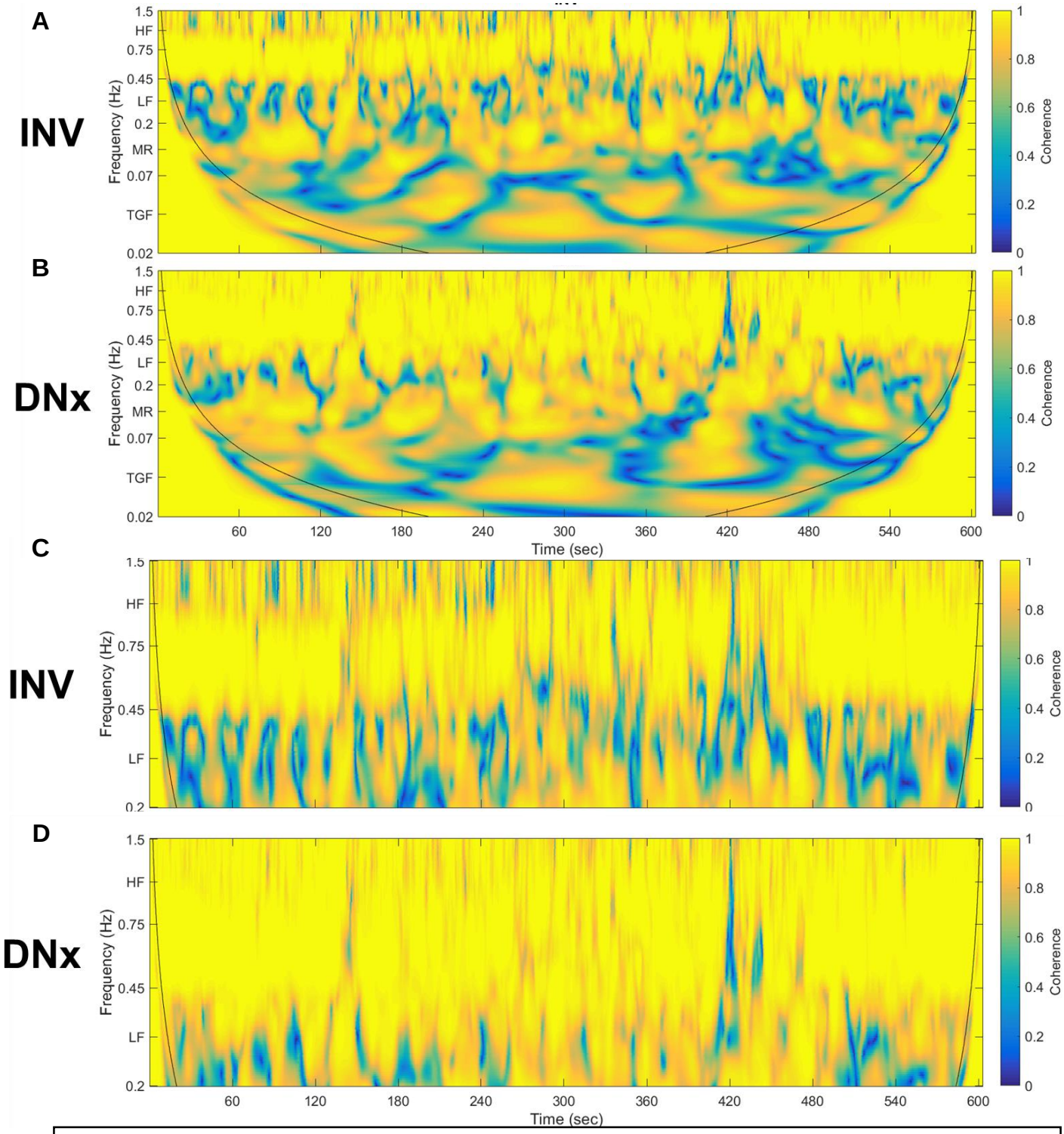

Figure 31 – Representative Time-Varying AP-RBF Coherence Plots

Representative time-varying coherence plots are shown for the pressure-flow to an (A) INV kidney and (B) DNx kidney in the same rabbit. Focusing on the LF and HF ranges, the (C) INV kidney shows green-blue vasomotion which is absent in the (D) DNx kidney, which exhibits blinding yellow passive pressure-flow.

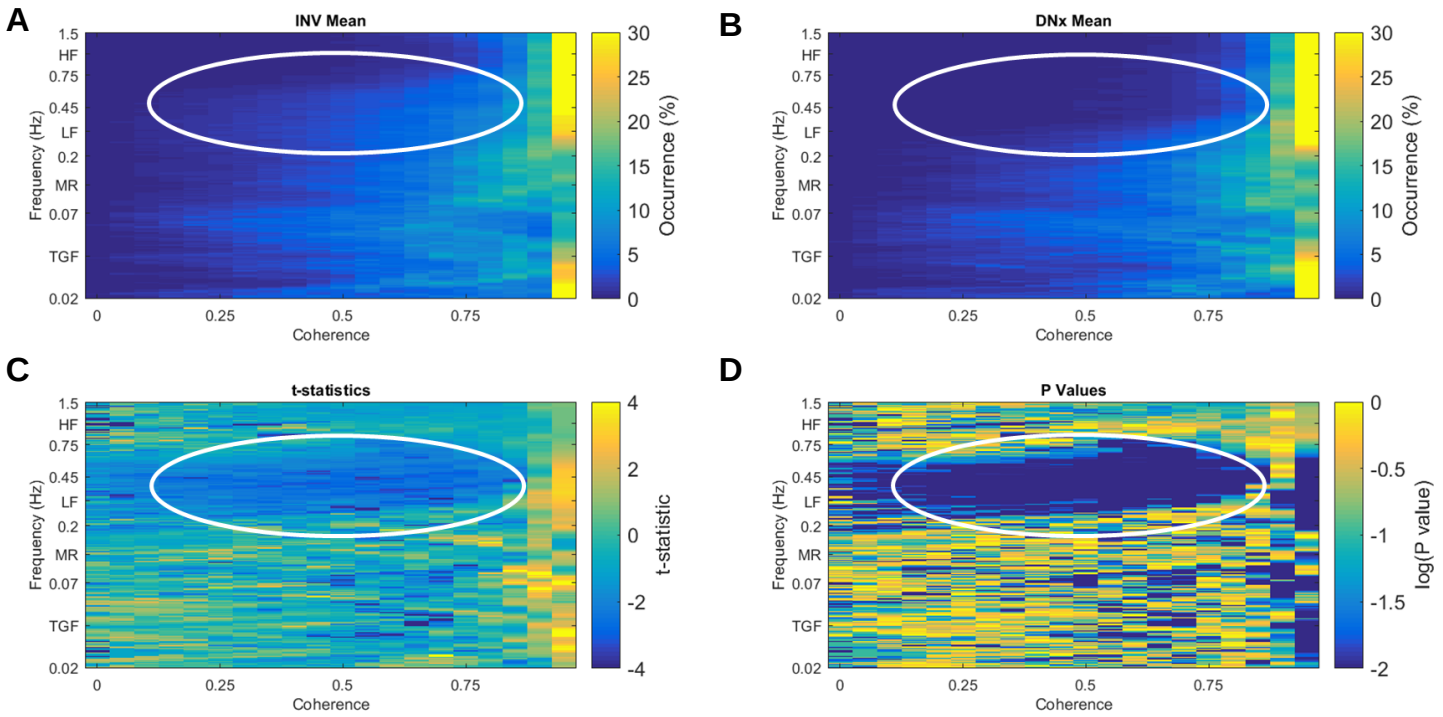

Figure 32 – Sympathetic Signature in AP-RBF Coherence Behavior

Mean AP-RBF coherence occurrence for bins of width 0.05 for (A) INV and (B) DNx kidneys. (C) T-statistics and (D) P values indicate a specific sympathetic signature resulting in low coherence in the LF range, consistent with a fast, active control mechanism which is eliminated by denervation. n = 5

Time-Varying Renal Pressure-Flow Coherence

A representative tracing of the pressure-flow coherence reveals low coherence in the LF range of the INV kidney which is absent in the DNx kidney, indicating the action of a vascular control mechanism in INV kidneys which is eliminated by renal denervation (Figure 31). Low LF pressure-flow coherence was seen in all INV kidneys but absent in DNx kidneys (Figure 32), indicating that LF renal sympathetic vasomotion is a fundamental part of physiological renal vascular control.

Occurrence in 3D Pressure-Flow Space

While it is meaningful to look at renal pressure-flow admittance gain, phase shift, and coherence in isolation because of their distinct physiological meanings, it is important to remember that each point in time has a gain, phase shift, and coherence value. This multidimensional system is difficult to visualize, but one method for visualization of this system for 0.3 Hz oscillations, located firmly in the LF range, is shown in Figure 33. This shows the ratio of DNx occurrence to INV occurrence for 0.3 Hz oscillations in pressure-flow in a 3D space of admittance gain, phase shift, and coherence. The opacity of the points represents the sum of the mean occurrence for both INV and DNx, so points with little to no occurrence are transparent. When visualized this way, one can appreciate the wide ranging behavior of the INV kidney, whose pressure-flow relationship is driven across this space by renal sympathetic vasomotion. This contrasts to the focal, passive behavior of the DNx kidney, which exclusively shows high-gain, synchronous, and high-coherence pressure-flow at 0.3 Hz.

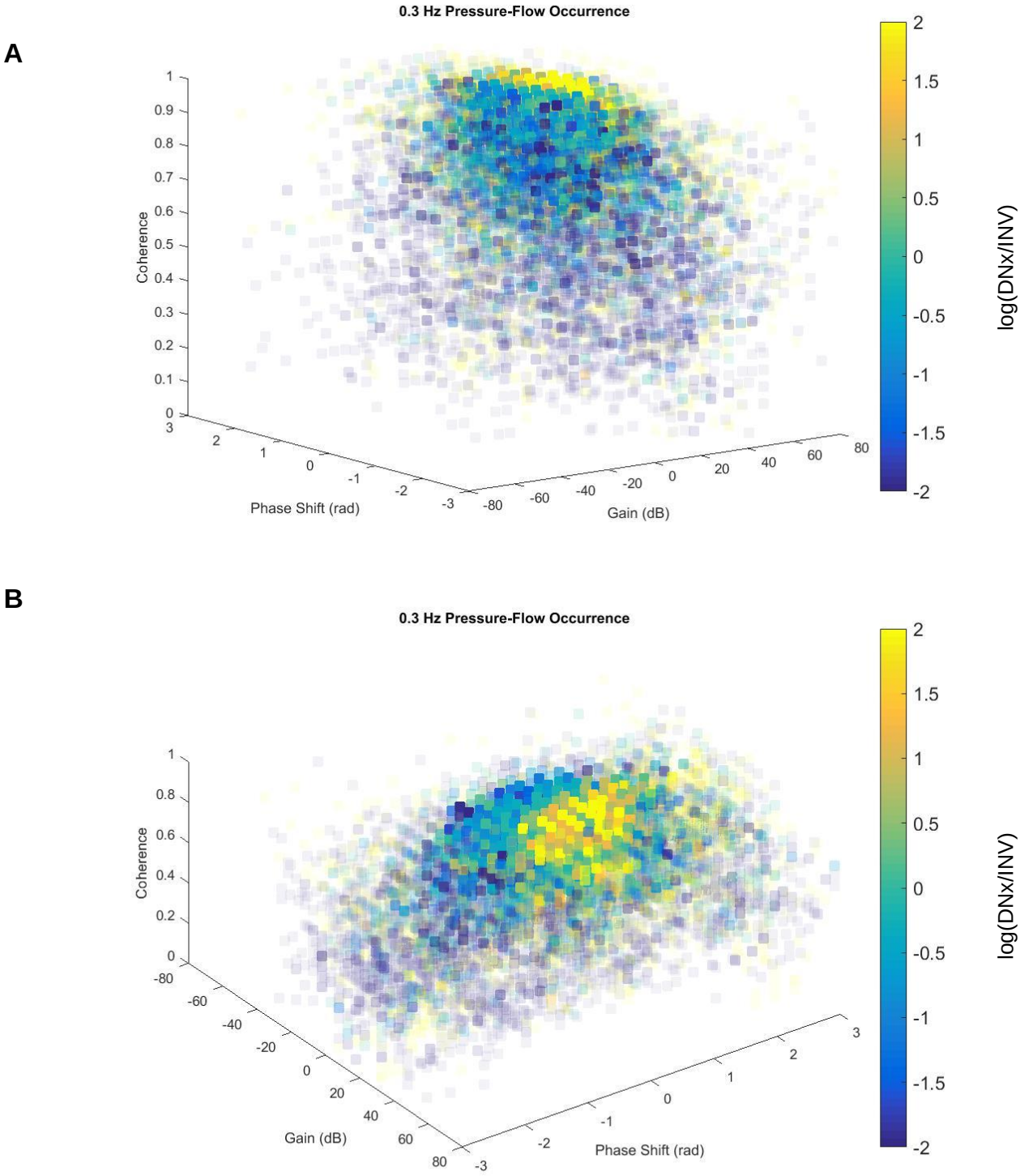

Figure 33 – INV and DNx 0.3 Hz Occurrence in 3D Pressure-Flow Transfer Function Space

The ratio of the mean DNx occurrence in a 3D transfer function space relative to the mean INV occurrence for 0.3 Hz oscillations. The sum mean occurrence is encoded as opacity while yellow indicates higher DNx occurrence and blue indicates higher INV occurrence. showing a predominance of high-gain, synchronous, high-coherence pressure-flow in DNx kidneys and more variable, low-gain, asynchronous, low-coherence pressure-flow in INV kidneys.

Discussion

This well-controlled study in unilaterally innervated rabbits with bilateral renal flow probes shows clearly that the renal nerves contribute to the physiological control of RBF. Sympathetic control of the renal vasculature imparts a time-varying vasoconstrictive influence which allows for the modulation of RVC as part of a concerted systemic response to hemodynamic stimuli whether they are small, physiological stimuli like postural changes, activity, and minor AP disturbances or large experimental stimuli like the nasopharyngeal reflex, hypoxia, or hemorrhage. This shows that the renal circulation is under strong sympathetic control like many other vascular beds and begs the question: How has the dogma to the contrary persisted for so long? We propose that the putative non-physiological, non-linear relationship between sympathetic outflow and RBF is simply the manifestation of the failure to consider the confounding influence of powerful renal autoregulatory mechanisms, and we encourage investigators not to forget about TGF and MR when interpreting experiments involving the control of RBF.

Studies performing dynamic electrical stimulation of the renal sympathetic nerves, either by sine wave or pseudorandom binary sequences, are particularly relevant to the discussion of the relationship between the underlying renal sympathetic nerve activity and the resultant renal vasomotion[141–143]. These studies indicate that the renal vasculature works as a low-pass filter, effectively eliminating sympathetic rhythms in the HF range. This explains why RSNA power at the respiratory and cardiac cycle frequencies does not reduce AP-RBF coherence; it is filtered by the vasculature.

Other convincing studies show how the renal nerves play a role in RBF control during normal activities. Chronically instrumented rats while grooming or sleeping show simultaneous increases in RSNA and decreases in RBF[144]. During brief, episodic activity, unilaterally denervated rabbits instrumented with bilateral renal flow probes showed increased variability in the episode-

averaged RBF and the AP-RBF relationship[131]. These studies clearly show that rapid, physiological changes in sympathetic outflow influence RBF.

Still other studies have used dynamic approaches to examine the response to experimental stimuli like hypoxia and hemorrhage[115,116]. These studies have shown an important role for the renal nerves in the generation of LF RBF oscillations in these sympatho-excitatory conditions and are reviewed more comprehensively elsewhere[140].

The techniques employed in this chapter to identify and characterize sympathetic vasomotion have several applications beyond the study of physiology. The most immediate clinical application pertains to the burgeoning field of renal denervation, that is, the use of a minimally invasive medical device to remove the renal sympathetic nerves. Presently, therapeutic renal denervation has significant momentum among clinicians and in the medical device industry. After promising Phase I and Phase II results showing large blood pressure reductions in hypertensive patients after renal denervation, the Phase III trial using the Medtronic catheter failed to lower blood pressure compared to a sham procedure[145]. Post-hoc analysis and expert opinion implicate inadequate renal nerve removal as the main reason for this shortcoming[146,147]. At present, none of the renal denervation systems provide the interventionist with any feedback about the success of the renal denervation. Because removal of the sympathetic nerves abolishes sympathetic vasomotion, this technology could allow for intraoperative validation of renal denervation, increasing the success of the procedure. It could also be used longitudinally to monitor patients to assess regrowth of the renal nerves or prognostically to identify treatment responders. It may also help companies to demonstrate device superiority or non-inferiority without the need to conduct expensive and challenging sham-controlled efficacy trials.

Other potential applications for this technique pertain to chronic, progressive diseases involving the sympathetic nervous system. Many diseases, including multiple systems atrophy, Parkinson's disease, diabetes, and pure autonomic failure can result in sympathetic failure and syncope. Clinical testing of the sympathetic nervous system is a mainstay in the work-up of patients

with clinical indications of sympathetic failure, but current autonomic tests are so crude, insensitive, and poorly reproducible that their use is discouraged in the context of syncope[148]. Our technique is inherently quantitative and allows for assessment of regional sympathetic vasomotor function. This means that this technique could be used clinically to diagnose sympathetic failure, map disease localization, assess disease severity, track progression of disease over time, and to evaluate or predict a patient's response to a therapy. By contrast, in cardiovascular and renal disease, excessive sympathetic activity contributes to disease progression and mortality. At present, no clinically useful test exists for the assessment of sympathetic activity. The introduction of a clinical tool for measuring regional sympathetic vasomotion could be used to better stratify patients, track disease progression, and guide treatment decisions.

In summary, the results of this study refute the idea that the renal sympathetic nerves do not contribute to physiological RBF control. The evidence for this dogma derives from historical interpretations which overlook both the role of the renal nerves and the strength of renal autoregulation. Careful dynamic analysis of the in-tact and denervated renal pressure-flow system reveals a clear role for the renal nerves as physiological regulators of RBF, operating on a beat-to-beat basis to recruit the renal vasculature according to underlying sympathetic rhythms.

Conclusions

Major Findings of the Dissertation

The major findings of the dissertation are:

1. That the pressor, sympatho-excitatory, and baroreflex dysfunction caused by central AngII depend on Rho kinase activation (Chapter I).
2. That pulse rate variability is a generally acceptable surrogate for heart rate variability for time- and frequency-domain measures, but the additional contribution of respiration to and the differing nonlinear properties of pulse rate variability should be considered by investigators (Chapter II).
3. Physiological renal sympathetic vasomotion can be detected, visualized, and comprehensively characterized using time-varying transfer function analysis of renal pressure-flow (Chapter III).

This work spans from the molecular mechanisms underlying sympatho-excitation in cardiovascular disease to validating widely used techniques for cardiac autonomic assessment to the development and application of a new method of detecting sympathetic vasomotion. Each of the major findings is discussed individually and then together in the context of my training as an aspiring physician-scientist.

Main Finding I: The Autonomic Effects of Central AngII Depend on Rho Kinase

Activation of the RAAS and autonomic dysfunction are pathophysiological hallmarks of cardiovascular disease. Our data shows that the pro-hypertensive, sympatho-excitatory, and baroreflex-perturbing effects of AngII in the brain are mediated by Rho kinase activation (Figure 34). This included direct recordings of sympathetic nerve activity, which showed that Rho kinase inhibition prevents the chronic renal sympatho-excitation and baroreflex dysfunction caused by central angiotensin. These data indicate that inhibition of the central Rho kinase pathway may act as a therapeutic brake on the positive feedback between central RAAS activation and sympathetic outflow in many diseases characterized by sympatho-excitation. Statins reduce Rho kinase activity and sympathetic outflow, and this study suggests that Rho kinase inhibition may be an important LDL-independent protective mechanism for the >30 million Americans currently taking statins.

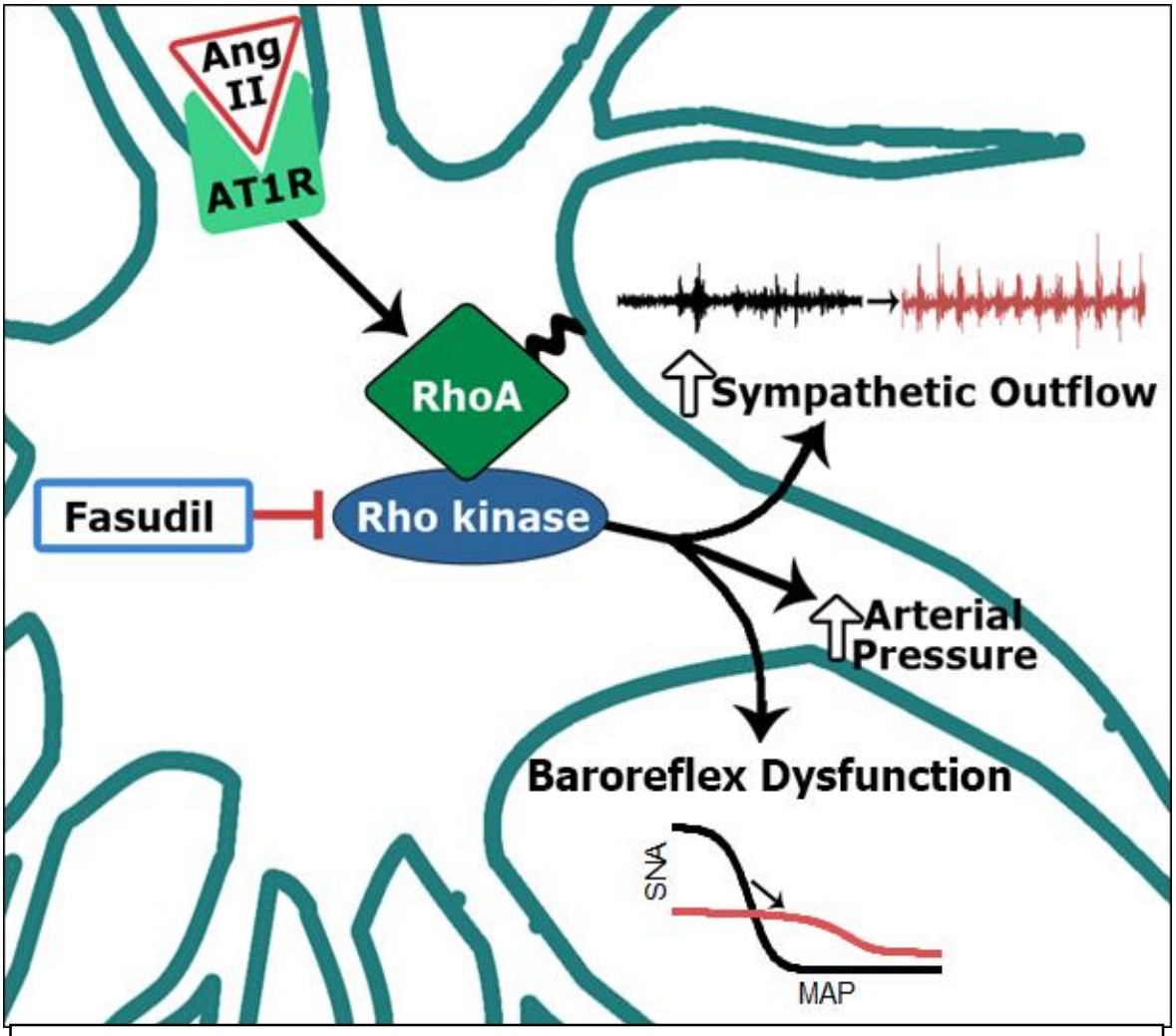

Figure 34 – Summary Figure of Main Finding I

Central AngII activates Rho kinase signaling downstream of AT1R, leading to baroreflex dysfunction, sympatho-excitation, and hypertension.

Main Finding II: Invasive Pulse Rate Variability as a Surrogate for Heart Rate Variability

HRV is the main determinant of invasively acquired PRV, and thus, it is an accurate and precise surrogate for time, frequency, and some non-linear measures of HRV at baseline. PRV slightly overestimates HRV parameters in both the time and frequency domains due to both the amplification of HRV oscillations as well as contributions from HRV-independent rhythms affecting pre-ejection time and pulse transit time. In particular, the mechanical effects of respiration on venous return, preload, stroke volume, and pulse pressure are the likely explanation for the HRV-independent centered in the respiratory frequency range. While robust correlations and moderate to high agreement were found between the changes in time- and absolute frequency-domain PRV and HRV parameters after autonomic blockade, most non-linear parameters showed very poor agreement after administration of autonomic blockers. Thus, invasively acquired PRV is likely an acceptale surrogate for HRV except when non-linear measures are a primary endpoint or when HRV is greatly reduced so that HRV-independent oscillations in the respiratory frequency range predominate. Because of the fact that the acceptable difference between two methods is application-specific, we encourage investigators planning to use PRV as a surrogate for HRV and readers trying to interpret studies in which PRV was performed as a surrogate for HRV to use the data in this chapter provided to assess the acceptability on a case-by-case basis.

Main Finding III: The Sympathetic Nervous System Participates in the Physiological Control of Renal Blood Flow

Similar to other vascular beds, the renal vasculature is under dynamic control by the sympathetic nervous system. This has been shown clearly by studies in unilaterally denervated conscious rabbits instrumented with bilateral renal flow probes. When analyzed by time-varying pressure-flow analysis, the INV kidney shows a clear vasoconstrictive, baroreflex influence in the LF consistent with active sympathetic control. The DNx kidney, while experiencing the same perfusion pressure, has no control mechanism present in this frequency range. This contradicts the long-held dogma that the renal nerves are silent in the physiological control of RBF, exerting vasoconstriction only in the context of disease or experimental stimuli. Further examination of this dogma shows that it relies on an underestimation of the powerful renal autoregulatory mechanisms, TGF and MR. This technique for the detection of sympathetic vasomotion has clinical implications in the setting of therapeutic renal denervation, chronic autonomic disease, and hemodynamic monitoring.

Interactions Between Main Findings: Reflections and Perspectives

The primary aim of my dissertation was focused on the role of Rho kinase as a functional mediator of the autonomic effects of AngII (Objective I), and it is this aim which occupied the vast majority of our time and discussion in supervisory committee meetings. The committee members all contributed in valuable ways. As evidence for this point, the study recently received largely positive reviews from the journal *Hypertension* (as of this writing), and the thing that struck me the most upon receiving the reviews was the similarity between the reviewer comments and the feedback from my supervisory committee. This shows how valuable these meetings have been for the development not only of me as a scientist but also of this project, and I am very grateful for the input and involvement of each of the committee members in this process.

The interplay between Objective I and the others relates mostly to the theme of autonomic neurophysiology and our motivation to make meaningful contributions to the field, be it at the level of molecular mechanism, method validation, or novel biomarker. I will briefly describe the genesis of these objectives and potential interactions which would be extremely interesting to investigate further. These objectives stem from Dr. Zucker's very open and encouraging disposition toward fostering my involvement in projects that leveraged my engineering background and interests. Objectives II and III were directed at the validation and development of methods for assessing autonomic control, and both objectives were born out of questions and struggles faced in our laboratory.

Objective II arose out of a simple question Dr. Zucker posed during a lab meeting. We routinely record AP in rats and mice but rarely are these animals instrumented with EKG telemetry, and several of my former labmates were interested in performing PRV analysis using the AP signal. Dr. Zucker asked if this was an acceptable surrogate for HRV and suggested that I look at this in some of my rabbits, which were instrumented with EKG leads and AP telemeters. I was quickly able to show a strong correlation between HRV and PRV, but, more interestingly, a literature search

revealed that this question had never been addressed in animals. Despite the existence of many preclinical studies in which PRV was used as HRV, no one had ever decided to validate this assumption. This contrasted sharply with the clinical literature, where I could find many studies investigating the acceptability of using finger plethysmography instead of EKG (it is uncommon for invasive AP catheters to be more convenient than EKG in the clinic). It seemed like we had found a significant gap in the literature and that our contribution would be useful not just to our lab but to others. We devised some additional simple experiments to better assess the underlying autonomic contributions to PRV and quickly executed the study, sparking my interest in the study of cardiovascular variability.

Objective III was born out of the frustrating experience of performing conscious recordings of RSNA in chronically instrumented rabbits. The delicate balance of making electrical contact with the renal sympathetic nerves without strangulating these fragile visceral fibers makes this a very difficult process. However, when everything works, the interplay between AP and RSNA in a healthy, conscious rabbit is reminiscent of a symphony. While these RSNA experiments were ongoing, we frequently discussed the assessment and quantification of sympathetic nerve activity, and Dr. Zucker had always expressed a desire for me to develop a new way to quantify RSNA. I was interested in using signals that worked more consistently and for longer durations; RBF was one such signal. We happened to have RBF data from INV and DNx kidneys, which would serve as an interesting all-or-none approach to assessing RSNA using RBF. We decided to compare the RBF between INV and DNx kidneys, uncovering a sympathetic signature in the RBF control of INV kidneys. We instrumented more rabbits with RBF probes and found the same result, indicating a clear role for the renal sympathetic nerves in the regulation of RBF which was completely contrary to the canonical view that the renal nerves were quiescent controllers of RBF. The investigation of the primary evidence for this dogma was a very disillusioning experience for me, and it forced me to confront a lot of very important issues that are rampant in biomedical science[149,150]. It was on this background that we performed the studies in Chapter III in a blinded

fashion and leveraged new tools geared toward improving reproducibility. It is my hope that, in the spirit of the openness of science, we are able to publish not only the findings but the dataset and analysis software, so that others may scrutinize and re-analyze the data to make their own conclusions.

While the different objectives share themes and motivations, I'd like to dedicate a few paragraphs to some of the direct links between the objectives that went unexplored in this dissertation but would have been very interesting to investigate in hindsight.

The first is the interaction between the central AngII-mediated cardiac sympatho-excitation demonstrated in Main Finding I and the relationship between HRV and PRV in Main Finding II. Since we were not inducing CHF in these studies, it became difficult to justify instrumenting rabbits with epicardial pacing leads, which requires an invasive thoracotomy procedure. It would have been interesting, however, to see if the relationship between HRV and PRV were different in a disease model with chronically elevated cardiac sympathetic tone. One might imagine that the additional contribution of contractility to HRV-independent PRV rhythms would be exaggerated, and the response to metoprolol in this context would have been particularly compelling.

Similarly, recording RBF in the rabbits used in Objective I would have yielded very important insights. For rabbits in the within-subjects cohort, this could have provided perspective into renal sympathetic outflow beyond the volume status studies, which are admittedly quite indirect. This data would also have provided valuable insight into how the sympathetic signature changes in the setting of chronic renal sympatho-excitation with sympathetic baroreflex dysfunction in a powerful, within-subjects design.

For rabbits in the between-subjects cohort, the addition of RSNA to the AP-RBF analysis would have served as a very important additional input to the system, which could have been leveraged to perform sophisticated multivariate analysis. One would hypothesize that by taking into account RSNA, the AP-RBF transfer function would be the same for INV and DNx kidneys. This would be a very important finding in support of the system postulated by Main Finding II. While

others have performed recordings of AP, RSNA, and RBF in the same animal, the results of these studies are often illogical (e.g., one study suggests that 90% of RBF variance can be explained by AP and another 90% of RBF variance can be explained by RSNA). Our multivariate approach and expertise could do a better job of characterizing the physiology.

In summary, each of these objectives made a formative contribution to my training as a nascent scientist. Objective I was my first experience in hypothesis generation, disease model testing, grant writing, IACUC protocol writing, and conscious animal experiments. Objective II was my first experience writing a manuscript as a first-author and bearing the critiques of the peer review process in that role. Objective III, because of its relevance to the burgeoning field of therapeutic renal denervation, has garnered considerable clinical and industry interest, teaching me about technology transfer. Each of these objectives emphasized to me the importance of environment, collaboration, luck, patience, and persistence, and these are important lessons that I will not forget as I continue my training to become a physician-scientist.

References

1. Mozaffarian, D. *et al.* Heart Disease and Stroke Statistics-2016 Update: A Report From the American Heart Association. *Circulation* **133,** e38–360 (2015).
2. James, P. A. *et al.* 2014 evidence-based guideline for the management of high blood pressure in adults: report from the panel members appointed to the Eighth Joint National Committee (JNC 8). *JAMA* **311,** 507–20 (2014).
3. Krum, H. *et al.* Device-based antihypertensive therapy: therapeutic modulation of the autonomic nervous system. *Circulation* **123,** 209–15 (2011).
4. Paton, J. F. R. *et al.* The carotid body as a therapeutic target for the treatment of sympathetically mediated diseases. *Hypertension* **61,** 5–13 (2013).
5. Lobo, M. D. *et al.* Central arteriovenous anastomosis for the treatment of patients with uncontrolled hypertension (the ROX CONTROL HTN study): a randomised controlled trial. *Lancet (London, England)* **385,** 1634–41 (2015).
6. Atlas, S. A. The renin-angiotensin aldosterone system: pathophysiological role and pharmacologic inhibition. *J. Manag. Care Pharm.* **13,** 9–20 (2007).
7. Grobe, J. L., Xu, D. & Sigmund, C. D. An intracellular renin-angiotensin system in neurons: fact, hypothesis, or fantasy. *Physiology (Bethesda).* **23,** 187–93 (2008).
8. Mangiapane, M. L. & Simpson, J. B. Subfornical organ: forebrain site of pressor and dipsogenic action of angiotensin II. *Am.J.Physiol.* **239,** R382–R389 (1980).
9. Ferguson, A. V. Angiotensinergic regulation of autonomic and neuroendocrine outputs: critical roles for the subfornical organ and paraventricular nucleus. *Neuroendocrinology* **89,** 370–6 (2009).
10. Bains, J. S., Potyok, A. & Ferguson, A. V. Angiotensin II actions in paraventricular nucleus: functional evidence for neurotransmitter role in efferents originating in subfornical organ. *Brain Res.* **599,** 223–229 (1992).
11. Latchford, K. J., Ferguson, A. V, Kevin, J. & Angiotensin, A. V. F. Angiotensin depolarizes parvocellular neurons in paraventricular nucleus through modulation of putative

nonselective cationic and potassium conductances. **6,** 52–58 (2005).

12. Malpas, S. C. Sympathetic nervous system overactivity and its role in the development of cardiovascular disease. *Physiol. Rev.* **90,** 513–57 (2010).
13. Grassi, G. *et al.* Sympathetic and baroreflex cardiovascular control in hypertension-related left ventricular dysfunction. *Hypertension* **53,** 205–9 (2009).
14. McBryde, F. D., Guild, S. J., Barrett, C. J., Osborn, J. W. & Malpas, S. C. Angiotensin II-based hypertension and the sympathetic nervous system: the role of dose and increased dietary salt in rabbits. *Exp Physiol* **92,** 831–840 (2007).
15. Zucker, I. H. Novel Mechanisms of Sympathetic Regulation in Chronic Heart Failure. *Hypertension* **48,** 1005–1011 (2006).
16. Zucker, I. H., Patel, K. P. & Schultz, H. D. Neurohumoral stimulation. *Heart Fail. Clin.* **8,** 87–99 (2012).
17. Zimmerman, M. C. Superoxide Mediates the Actions of Angiotensin II in the Central Nervous System. *Circ. Res.* **91,** 1038–1045 (2002).
18. Shi, J., Zhang, L. & Wei, L. Rho-kinase in development and heart failure: insights from genetic models. *Pediatr. Cardiol.* **32,** 297–304 (2011).
19. Nguyen Dinh Cat, A. & Touyz, R. M. Cell signaling of angiotensin II on vascular tone: novel mechanisms. *Curr. Hypertens. Rep.* **13,** 122–8 (2011).
20. Higashi, M. *et al.* Long-term inhibition of Rho-kinase suppresses angiotensin II-induced cardiovascular hypertrophy in rats in vivo: effect on endothelial NAD(P)H oxidase system. *Circ. Res.* **93,** 767–75 (2003).
21. Burger, D. *et al.* Endothelial microparticle formation by angiotensin II is mediated via Ang II receptor type I/NADPH oxidase/ Rho kinase pathways targeted to lipid rafts. *Arterioscler. Thromb. Vasc. Biol.* **31,** 1898–907 (2011).
22. Rupérez, M. *et al.* HMG-CoA reductase inhibitors decrease angiotensin II-induced vascular fibrosis: Role of RhoA/ROCK and MAPK pathways. *Hypertension* **50,** 377–383 (2007).

23. Guilluy, C. *et al.* The Rho exchange factor Arhgef1 mediates the effects of angiotensin II on vascular tone and blood pressure. *Nat. Med.* **16,** 183–90 (2010).

24. Calò, L. A. *et al.* Increased level of p63RhoGEF and RhoA/Rho kinase activity in hypertensive patients. *J. Hypertens.* **32,** 331–8 (2014).

25. Bregeon, J., Loirand, G., Pacaud, P. & Rolli-Derkinderen, M. Angiotensin II induces RhoA activation through SHP2-dependent dephosphorylation of the RhoGAP p190A in vascular smooth muscle cells. *Am. J. Physiol. Cell Physiol.* **297,** C1062–70 (2009).

26. Peng, C. K., Havlin, S., Stanley, H. E. & Goldberger, A. L. Quantification of scaling exponents and crossover phenomena in nonstationary heartbeat time series. *Chaos (Woodbury, N.Y.)* **5,** 82–7 (1995).

27. Mann, D. L. & Bristow, M. R. Mechanisms and models in heart failure: the biomechanical model and beyond. *Circulation* **111,** 2837–49 (2005).

28. Schiffrin, E. L., Lipman, M. L. & Mann, J. F. E. Chronic kidney disease: effects on the cardiovascular system. *Circulation* **116,** 85–97 (2007).

29. Converse, R. L. *et al.* Sympathetic overactivity in patients with chronic renal failure. *N. Engl. J. Med.* **327,** 1912–8 (1992).

30. Mancia, G., Dell'Oro, R., Quarti-Trevano, F., Scopelliti, F. & Grassi, G. Angiotensin-sympathetic system interactions in cardiovascular and metabolic disease. *J. Hypertens. Suppl.* **24,** S51–6 (2006).

31. Mancia, G., Grassi, G., Giannattasio, C. & Seravalle, G. Sympathetic Activation in the Pathogenesis of Hypertension and Progression of Organ Damage. *Hypertension* **34,** 724–728 (1999).

32. Sasaki, S. & Dampney, R. A. Tonic cardiovascular effects of angiotensin II in the ventrolateral medulla. *Hypertension* **15,** 274–83 (1990).

33. Matsumura, K., Averill, D. B. & Ferrario, C. M. Angiotensin II acts at AT1 receptors in the nucleus of the solitary tract to attenuate the baroreceptor reflex. *Am J Physiol Regul. Integr*.

Comp Physiol **275,** R1611–1619 (1998).

34. Davisson, R. L. & Zimmerman, M. C. Angiotensin II, oxidant signaling, and hypertension: down to a T? *Hypertension* **55,** 228–30 (2010).

35. Savalia, K. *et al.* Neuronal uptake of nanoformulated superoxide dismutase and attenuation of angiotensin II-dependent hypertension after central administration. *Free Radic. Biol. Med.* **73,** 299–307 (2014).

36. Zimmerman, M. C., Lazartigues, E., Sharma, R. V. & Davisson, R. L. Hypertension caused by angiotensin II infusion involves increased superoxide production in the central nervous system. *Circ. Res.* **95,** 210–216 (2004).

37. Llewellyn, T., Zheng, H., Liu, X., Xu, B. & Patel, K. P. Median preoptic nucleus and subfornical organ drive renal sympathetic nerve activity via a glutamatergic mechanism within the paraventricular nucleus. *Am. J. Physiol. Regul. Integr. Comp. Physiol.* **302,** R424–32 (2012).

38. Li, Y.-F., Mayhan, W. G. & Patel, K. P. NMDA-mediated increase in renal sympathetic nerve discharge within the PVN: role of nitric oxide. *Am J Physiol Hear. Circ Physiol* **281,** H2328–2336 (2001).

39. Sharma, N. M., Llewellyn, T. L., Zheng, H. & Patel, K. P. Angiotensin II-mediated posttranslational modification of nNOS in the PVN of rats with CHF: role for PIN. *Am. J. Physiol. Heart Circ. Physiol.* **305,** H843–55 (2013).

40. Li, Y.-F., Wang, W., Mayhan, W. G. & Patel, K. P. Angiotensin-mediated increase in renal sympathetic nerve discharge within the PVN: role of nitric oxide. *Am. J. Physiol. Regul. Integr. Comp. Physiol.* **290,** R1035–43 (2006).

41. Rikitake, Y. & Liao, J. K. Rho GTPases, statins, and nitric oxide. *Circ. Res.* **97,** 1232–1235 (2005).

42. Dong, M. *et al.* Rho-kinase inhibition: a novel therapeutic target for the treatment of cardiovascular diseases. *Drug Discov. Today* **15,** 622–629 (2010).

43. Hata, T. *et al.* Calcium channel blocker and Rho-associated kinase activity in patients with hypertension. *J. Hypertens.* **29,** 373–9 (2011).

44. Masumoto, A. *et al.* Possible Involvement of Rho-Kinase in the Pathogenesis of Hypertension in Humans. *Hypertension* **38,** 1307–1310 (2001).

45. Kishi, T. *et al.* Rho-kinase inhibitor improves increased vascular resistance and impaired vasodilation of the forearm in patients with heart failure. *Circulation* **111,** 2741–7 (2005).

46. Haack, K. K. V *et al.* Central Rho kinase inhibition restores baroreflex sensitivity and angiotensin II type 1 receptor protein imbalance in conscious rabbits with chronic heart failure. *Hypertension* **61,** 723–9 (2013).

47. Ito, K. *et al.* Rho/Rho-kinase pathway in the brainstem contributes to hypertension caused by chronic nitric oxide synthase inhibition. *Hypertension* **43,** 156–62 (2004).

48. Ito, K. *et al.* Rho/Rho-kinase pathway in brain stem contributes to blood pressure regulation via sympathetic nervous system: Possible involvement in neural mechanisms of hypertension. *Circ. Res.* **92,** 1337–1343 (2003).

49. Ito, K., Kimura, Y., Hirooka, Y., Sagara, Y. & Sunagawa, K. Activation of Rho-kinase in the brainstem enhances sympathetic drive in mice with heart failure. *Auton. Neurosci. Basic Clin.* **142,** 77–81 (2008).

50. Ito, K. *et al.* Inhibition of Rho-kinase in the nucleus tractus solitarius enhances glutamate sensitivity in rats. *Hypertension* **46,** 360–365 (2005).

51. Sagara, Y. *et al.* Pressor response induced by central angiotensin II is mediated by activation of Rho/Rho-kinase pathway via AT1 receptors. *J. Hypertens.* **25,** 399–406 (2007).

52. Ricketts, J. H. & Head, G. A. A five-parameter logistic equation for investigating asymmetry of curvature in baroreflex studies. *Am. J. Physiol.* **277,** R441–54 (1999).

53. Schiller, A. M., Pellegrino, P. R. & Zucker, I. H. Renal nerves dynamically regulate renal blood flow in conscious, healthy rabbits. *Am. J. Physiol. Regul. Integr. Comp. Physiol.* **310,** R156–66 (2016).

54. Dorward, P. K., Riedel, W., Burke, S. L., Gipps, J. & Korner, P. I. The renal sympathetic baroreflex in the rabbit. Arterial and cardiac baroreceptor influences, resetting, and effect of anesthesia. *Circ. Res.* **57,** 618–33 (1985).

55. Eaton, S. L. *et al.* Quantitative imaging of tissue sections using infrared scanning technology. *J. Anat.* **228,** 203–13 (2016).

56. Potvin, P. J. & Schutz, R. W. Statistical power for the two-factor repeated measures ANOVA. *Behav. Res. Methods. Instrum. Comput.* **32,** 347–56 (2000).

57. Guild, S.-J. *et al.* Quantifying sympathetic nerve activity: problems, pitfalls and the need for standardization. *Exp. Physiol.* **95,** 41–50 (2010).

58. Gao, L. *et al.* Sympathoexcitation by central ANG II: roles for AT1 receptor upregulation and NAD(P)H oxidase in RVLM. *Am. J. Physiol. Heart Circ. Physiol.* **288,** H2271–H2279 (2005).

59. Lontay, B. *et al.* Localization of myosin phosphatase target subunit 1 in rat brain and in primary cultures of neuronal cells. *J. Comp. Neurol.* **478,** 72–87 (2004).

60. Lohmeier, T. E., Irwin, E. D., Rossing, M. A., Serdar, D. J. & Kieval, R. S. Prolonged Activation of the Baroreflex Produces Sustained Hypotension. *Hypertension* **43,** 306–311 (2004).

61. Lohmeier, T. E. *et al.* Renal denervation does not abolish sustained baroreflex-mediated reductions in arterial pressure. *Hypertension* **49,** 373–379 (2007).

62. Lohmeier, T. E. & Iliescu, R. The baroreflex as a long-term controller of arterial pressure. *Physiology (Bethesda).* **30,** 148–58 (2015).

63. Lohmeier, T. E. *et al.* Sustained suppression of sympathetic activity and arterial pressure during chronic activation of the carotid baroreflex. *Am. J. Physiol. Heart Circ. Physiol.* **299,** H402–9 (2010).

64. Thrasher, T. N. Unloading arterial baroreceptors causes neurogenic hypertension. *Am. J. Physiol. Regul. Integr. Comp. Physiol.* **282,** R1044–53 (2002).

65. Thrasher, T. N. Effects of chronic baroreceptor unloading on blood pressure in the dog. *Am. J. Physiol. Regul. Integr. Comp. Physiol.* **288,** R863–71 (2005).

66. Bisognano, J. D. *et al.* Baroreflex activation therapy lowers blood pressure in patients with resistant hypertension: results from the double-blind, randomized, placebo-controlled rheos pivotal trial. *J. Am. Coll. Cardiol.* **58,** 765–73 (2011).

67. Ehmke, H., Persson, P. B., Seyfarth, M. & Kirchheim, H. R. Neurogenic control of pressure natriuresis in conscious dogs. *Am. J. Physiol.* **259,** F466–73 (1990).

68. Brand, P. H. *et al.* Pressure diuresis and autonomic function in conscious dogs. *Am. J. Physiol.* **261,** R802–10 (1991).

69. Guyton, A. Blood pressure control--special role of the kidneys and body fluids. *Science (80-.).* **252,** 1813–1816 (1991).

70. Tan, W., Panzenbeck, M. J., Hajdu, M. A. & Zucker, I. H. A central mechanism of acute baroreflex resetting in the conscious dog. *Circ. Res.* **65,** 63–70 (1989).

71. Chapleau, M. W., Hajduczok, G. & Abboud, F. M. PERIPHERAL CENTRAL MECHANISMS OF BAROREFLEX RESETTING. *Clin. Exp. Pharmacol. Physiol.* **16,** 31–43 (1989).

72. McKinley, M. J., Badoer, E., Vivas, L. & Oldfield, B. J. Comparison of c-fos expression in the lamina terminalis of conscious rats after intravenous or intracerebroventricular angiotensin. *Brain Res. Bull.* **37,** 131–137 (1995).

73. Wirth, A. Rho kinase and hypertension. *Biochim. Biophys. Acta - Mol. Basis Dis.* **1802,** 1276–1284 (2010).

74. Zimmerman, M. C., Sharma, R. V & Davisson, R. L. Superoxide mediates angiotensin II-induced influx of extracellular calcium in neural cells. *Hypertension* **45,** 717–23 (2005).

75. Loirand, G. Rho Kinases in Health and Disease: From Basic Science to Translational Research. *Pharmacol. Rev.* **67,** 1074–95 (2015).

76. Huang, H. *et al.* Rho-kinase regulates energy balance by targeting hypothalamic leptin

receptor signaling. *Nat. Neurosci.* **15,** 1391–8 (2012).

77. Liao, J. K., Seto, M. & Noma, K. Rho kinase (ROCK) inhibitors. *J. Cardiovasc. Pharmacol.* **50,** 17–24 (2007).

78. Shibuya, M., Hirai, S., Seto, M., Satoh, S. & Ohtomo, E. Effects of fasudil in acute ischemic stroke: results of a prospective placebo-controlled double-blind trial. *J. Neurol. Sci.* **238,** 31–9 (2005).

79. Suzuki, Y., Shibuya, M., Satoh, S.-I., Sugimoto, Y. & Takakura, K. A postmarketing surveillance study of fasudil treatment after aneurysmal subarachnoid hemorrhage. *Surg. Neurol.* **68,** 126–31; discussion 131–2 (2007).

80. Garnock-Jones, K. P. Ripasudil: first global approval. *Drugs* **74,** 2211–5 (2014).

81. Hall, A. Rho GTPases and the Actin Cytoskeleton. *Science (80-.).* **279,** 509–514 (1998).

82. Nohria, A. *et al.* Statins inhibit Rho kinase activity in patients with atherosclerosis. *Atherosclerosis* **205,** 517–21 (2009).

83. Haack, K. K. V, Marcus, N. J., Del Rio, R., Zucker, I. H. & Schultz, H. D. Simvastatin treatment attenuates increased respiratory variability and apnea/hypopnea index in rats with chronic heart failure. *Hypertension* **63,** 1041–9 (2014).

84. Pliquett, R. U., Cornish, K. G., Peuler, J. D. & Zucker, I. H. Simvastatin normalizes autonomic neural control in experimental heart failure. *Circulation* **107,** 2493–8 (2003).

85. Gao, L., Wang, W. & Zucker, I. H. Simvastatin inhibits central sympathetic outflow in heart failure by a nitric-oxide synthase mechanism. *J. Pharmacol. Exp. Ther.* **326,** 278–85 (2008).

86. Gao, L. Simvastatin Therapy Normalizes Sympathetic Neural Control in Experimental Heart Failure: Roles of Angiotensin II Type 1 Receptors and NAD(P)H Oxidase. *Circulation* **112,** 1763–1770 (2005).

87. Deo, S. H. *et al.* Statin therapy lowers muscle sympathetic nerve activity and oxidative stress in patients with heart failure. *Am. J. Physiol. Heart Circ. Physiol.* **303,** H377–85 (2012).

88. Lewandowski, J., Symonides, B., Gaciong, Z. & Siński, M. The effect of statins on

sympathetic activity: a meta-analysis. *Clin. Auton. Res.* **25,** 125–31 (2015).

89. Lewandowski, J. *et al.* Simvastatin reduces sympathetic activity in men with hypertension and hypercholesterolemia. *Hypertens. Res.* **33,** 1038–1043 (2010).

90. McGowan, C. L. *et al.* Simvastatin reduces sympathetic outflow and augments endothelium-independent dilation in non-hyperlipidaemic primary hypertension. *Heart* **99,** 240–6 (2013).

91. Trebicka, J. *et al.* Atorvastatin lowers portal pressure in cirrhotic rats by inhibition of RhoA/Rho-kinase and activation of endothelial nitric oxide synthase. *Hepatology* **46,** 242–253 (2007).

92. Barretto, A. C. P. *et al.* Increased muscle sympathetic nerve activity predicts mortality in heart failure patients. *Int. J. Cardiol.* **135,** 302–7 (2009).

93. Brunner-La Rocca, H. P., Esler, M. D., Jennings, G. L. & Kaye, D. M. Effect of cardiac sympathetic nervous activity on mode of death in congestive heart failure. *Eur. Heart J.* **22,** 1136–43 (2001).

94. Cohn, J. N. *et al.* Plasma norepinephrine as a guide to prognosis in patients with chronic congestive heart failure. *N. Engl. J. Med.* **311,** 819–23 (1984).

95. Zucker, I. H. *et al.* Chronic baroreceptor activation enhances survival in dogs with pacing-induced heart failure. *Hypertension* **50,** 904–10 (2007).

96. Li, M. *et al.* Vagal nerve stimulation markedly improves long-term survival after chronic heart failure in rats. *Circulation* **109,** 120–4 (2004).

97. Nolan, J. *et al.* Prospective study of heart rate variability and mortality in chronic heart failure: results of the United Kingdom heart failure evaluation and assessment of risk trial (UK-heart). *Circulation* **98,** 1510–6 (1998).

98. Cooke, W. H. *et al.* Heart period variability in trauma patients may predict mortality and allow remote triage. *Aviat. Space. Environ. Med.* **77,** 1107–12 (2006).

99. Task Force of the European Society of Cardiology and the North American Society of

Pacing and Electrophysiology. Heart rate variability: standards of measurement, physiological interpretation and clinical use. *Circulation* **93,** 1043–65 (1996).

100. Schäfer, A. & Vagedes, J. How accurate is pulse rate variability as an estimate of heart rate variability? A review on studies comparing photoplethysmographic technology with an electrocardiogram. *Int. J. Cardiol.* **166,** 15–29 (2013).

101. Constant, I., Laude, D., Murat, I. & Elghozi, J. Pulse rate variability is not a surrogate for heart rate variability. **397,** 391–397 (1999).

102. Baudrie, V., Laude, D. & Elghozi, J.-L. Optimal frequency ranges for extracting information on cardiovascular autonomic control from the blood pressure and pulse interval spectrograms in mice. *Am. J. Physiol. Regul. Integr. Comp. Physiol.* **292,** R904–12 (2007).

103. Baltatu, O. *et al.* Alterations in blood pressure and heart rate variability in transgenic rats with low brain angiotensinogen. *Hypertension* **37,** 408–13 (2001).

104. Moguilevski, V. a., Shiel, L., Oliver, J. & McGrath, B. P. Power spectral analysis of heart-rate variability reflects the level of cardiac autonomic activity in rabbits. *J. Auton. Nerv. Syst.* **58,** 18–24 (1996).

105. La Rovere, M. T., Bigger, J. T., Marcus, F. I., Mortara, A. & Schwartz, P. J. Baroreflex sensitivity and heart-rate variability in prediction of total cardiac mortality after myocardial infarction. ATRAMI. *Lancet* **351,** 478–484 (1998).

106. Eckberg, D. L. Sympathovagal balance: a critical appraisal. *Circulation* **96,** 3224–32 (1997).

107. Valencia, J. F. *et al.* Multiscale sample entropy in heart rate variability of aortic stenosis patients. *Conf. Proc. ... Annu. Int. Conf. IEEE Eng. Med. Biol. Soc. IEEE Eng. Med. Biol. Soc. Annu. Conf.* **2008,** 2000–3 (2008).

108. Trunkvalterova, Z. *et al.* Reduced short-term complexity of heart rate and blood pressure dynamics in patients with diabetes mellitus type 1: multiscale entropy analysis. *Physiol. Meas.* **29,** 817–28 (2008).

109. Costa, M. & Healey, J. A. Multiscale entropy analysis of complex heart rate dynamics: discrimination of age and heart failure effects. in *Computers in Cardiology, 2003* 705–708 (IEEE, 2003). doi:10.1109/CIC.2003.1291253

110. Norris, P. R., Anderson, S. M., Jenkins, J. M., Williams, A. E. & Morris, J. a. Heart rate multiscale entropy at three hours predicts hospital mortality in 3,154 trauma patients. *Shock* **30,** 17–22 (2008).

111. Riordan, W. P., Norris, P. R., Jenkins, J. M. & Morris, J. A. Early loss of heart rate complexity predicts mortality regardless of mechanism, anatomic location, or severity of injury in 2178 trauma patients. *J. Surg. Res.* **156,** 283–9 (2009).

112. Norris, P. R., Stein, P. K. & Morris, J. A. Reduced heart rate multiscale entropy predicts death in critical illness: a study of physiologic complexity in 285 trauma patients. *J. Crit. Care* **23,** 399–405 (2008).

113. Ho, Y.-L., Lin, C., Lin, Y.-H. & Lo, M.-T. The prognostic value of non-linear analysis of heart rate variability in patients with congestive heart failure--a pilot study of multiscale entropy. *PLoS One* **6,** e18699 (2011).

114. Gao, L. *et al.* Simvastatin therapy normalizes sympathetic neural control in experimental heart failure: roles of angiotensin II type 1 receptors and NAD(P)H oxidase. *Circulation* **112,** 1763–70 (2005).

115. Janssen, B. J., Malpas, S. C., Burke, S. L. & Head, G. A. Frequency-dependent modulation of renal blood flow by renal nerve activity in conscious rabbits. *Am. J. Physiol.* **273,** R597–608 (1997).

116. Malpas, S. C., Evans, R. G., Head, G. A. & Lukoshkova, E. V. Contribution of renal nerves to renal blood flow variability during hemorrhage. *Am. J. Physiol.* **274,** R1283–94 (1998).

117. Costa, M., Goldberger, A. L. & Peng, C.-K. Multiscale entropy analysis of biological signals. *Phys. Rev. E. Stat. Nonlin. Soft Matter Phys.* **71,** 021906 (2005).

118. Goldberger, A. L. *et al.* PhysioBank, PhysioToolkit, and PhysioNet: components of a new

research resource for complex physiologic signals. *Circulation* **101,** E215–20 (2000).

119. Allen, J. Photoplethysmography and its application in clinical physiological measurement. *Physiol. Meas.* **28,** R1–39 (2007).

120. Giardino, N. D., Lehrer, P. M. & Edelberg, R. Comparison of finger plethysmograph to ECG in the measurement of heart rate variability. *Psychophysiology* **39,** 246–53 (2002).

121. Dawson, S., Panerai, R. & Potter, J. Should one use electrocardiographic or Finapres-derived pulse intervals for calculation of cardiac baroreceptor sensitivity? *Blood Press. Monit.* **3,** 315–320 (1998).

122. Rauh, R., Limley, R., Bauer, R.-D., Radespiel-Troger, M. & Mueck-Weymann, M. <title>Comparison of heart rate variability and pulse rate variability detected with photoplethysmography</title>. in *Proceedings of the SPIE* (ed. Tuchin, V. V.) **5474,** 115–126 (2004).

123. Bhatia, V., Rarick, K. R. & Stauss, H. M. Effect of the data sampling rate on accuracy of indices for heart rate and blood pressure variability and baroreflex function in resting rats and mice. *Physiol. Meas.* **31,** 1185–201 (2010).

124. HF, P.-Q., D, D.-R., MB, C.-S. & RR, F. de la V.-P. Evaluation of pulse rate variability obtained by the pulse onsets of the photoplethysmographic signal.

125. Bland, J. M. & Altman, D. G. Statistical Methods in Medical Research. *Stat. Methods Med. Res.* **8,** 161–179 (1999).

126. Carlström, M., Wilcox, C. S. & Arendshorst, W. J. Renal Autoregulation in Health and Disease. *Physiol. Rev.* **95,** 405–511 (2015).

127. Coote, J. H., Johns, E. J., Macleod, V. H. & Singer, B. Effect of renal nerve stimulation, renal blood flow and adrenergic blockade on plasma renin activity in the cat. *J. Physiol.* **226,** 15–36 (1972).

128. Kopp, U., Aurell, M., Nilsson, I. M. & Ablad, B. The role of beta-1-adrenoceptors in the renin release response to graded renal sympathetic nerve stimulation. *Pflügers Arch. Eur.*

J. Physiol. **387,** 107–13 (1980).

129. Kopp, U., Aurell, M., Sjölander, M. & Ablad, B. The role of prostaglandins in the alpha- and beta-adrenoceptor mediated renin release response to graded renal nerve stimulation. *Pflügers Arch. Eur. J. Physiol.* **391,** 1–8 (1981).

130. Poucher, S. M. & Karim, F. The renal response to electrical stimulation of renal efferent sympathetic nerves in the anaesthetized greyhound. *J. Physiol.* **434,** 1–10 (1991).

131. Barrett, C. J., Navakatikyan, M. A., Malpas, S. C. & Carolyn, J. Long-term control of renal blood flow : what is the role of the renal nerves ? *Am J Physiol Regul. Integr. Comp Physiol* 1534–1545 (2001).

132. Berne, R. Hemodynamics and sodium excretion of denervated kidney in anesthetized and unanesthetized dog. *Am. J. Physiol.* **171,** 148–58 (1952).

133. Sadowski, J., Kurkus, J. & Gellert, R. Denervated and intact kidney responses to saline load in awake and anesthetized dogs. *Am. J. Physiol.* **237,** F262–7 (1979).

134. Brown, G. & Venuto, R. Measurement of Renal Blood-Flow of Conscious Rabbits Utilizing Ultrasonic Flowprobes - The Effect of Cyclooxygenase Inhibition. in *Clinical Research* **37,** A950–A950 (1989).

135. Malpas, S. C. Neural influences on cardiovascular variability: possibilities and pitfalls. *Am J Physiol Hear. Circ Physiol* **282,** H6–20 (2002).

136. Abu-Amarah, I., Ajikobi, D. O., Bachelard, H., Cupples, W. A. & Salevsky, F. C. Responses of mesenteric and renal blood flow dynamics to acute denervation in anesthetized rats. *Am. J. Physiol.* **275,** R1543–52 (1998).

137. DiBona, G. F. & Sawin, L. L. Effect of renal denervation on dynamic autoregulation of renal blood flow. *Am. J. Physiol. Renal Physiol.* **286,** F1209–18 (2004).

138. Lessard, A., Salevsky, F. C., Bachelard, H. & Cupples, W. A. Incommensurate frequencies of major vascular regulatory mechanisms. *Can. J. Physiol. Pharmacol.* **77,** 293–9 (1999).

139. Iliescu, R., Cazan, R., McLemore, G. R., Venegas-Pont, M. & Ryan, M. J. Renal blood flow

and dynamic autoregulation in conscious mice. *Am. J. Physiol. Renal Physiol.* **295,** F734–F740 (2008).

140. Malpas, S. C. & Leonard, B. L. Neural Regulation Of Renal Blood Flow: A Re-Examination. *Clin. Exp. Pharmacol. Physiol.* **27,** 956–964 (2000).

141. Guild, S. J., Austin, P. C., Navakatikyan, M., Ringwood, J. V & Malpas, S. C. Dynamic relationship between sympathetic nerve activity and renal blood flow: a frequency domain approach. *Am. J. Physiol. Regul. Integr. Comp. Physiol.* **281,** R206–12 (2001).

142. Malpas, S. C. *et al.* Resonance in the renal vasculature evoked by activation of the sympathetic nerves. *Am. J. Physiol.* **276,** R1311–9 (1999).

143. DiBona, G. F. & Sawin, L. L. Frequency response of the renal vasculature in congestive heart failure. *Circulation* **107,** 2159–64 (2003).

144. Yoshimoto, M., Sakagami, T., Nagura, S. & Miki, K. Relationship between renal sympathetic nerve activity and renal blood flow during natural behavior in rats. *Am. J. Physiol. Regul. Integr. Comp. Physiol.* **286,** R881–7 (2004).

145. Bhatt, D. L. *et al.* A controlled trial of renal denervation for resistant hypertension. *N. Engl. J. Med.* **370,** 1393–401 (2014).

146. Kandzari, D. E. *et al.* Predictors of blood pressure response in the SYMPLICITY HTN-3 trial. *Eur. Heart J.* **36,** 219–27 (2015).

147. Esler, M. Illusions of truths in the Symplicity HTN-3 trial: generic design strengths but neuroscience failings. *J. Am. Soc. Hypertens.* **8,** 593–8 (2014).

148. Strickberger, S. A. *et al.* AHA/ACCF Scientific Statement on the evaluation of syncope: from the American Heart Association Councils on Clinical Cardiology, Cardiovascular Nursing, Cardiovascular Disease in the Young, and Stroke, and the Quality of Care and Outcomes Research Interdi. *Circulation* **113,** 316–27 (2006).

149. Begley, C. G. & Ioannidis, J. P. A. Reproducibility in science: Improving the standard for basic and preclinical research. *Circ. Res.* **116,** 116–126 (2015).

150. Open Science Collaboration. Estimating the reproducibility of psychological science. *Science (80-.).* **349,** aac4716–aac4716 (2015).

Appendix

Table 1 – Indices of HRV and PRV derived from the systolic maximum fiducial point for 30 baseline recordings

Category	Index	HRV	PRV	Bland-Altman Interval (%)	Bias Consistency	r^2
Time Domain	Heart rate (bpm)	187 ± 4	187 ± 4	-0.06 ± 0.22	27/30***	0.999
	SDNN (ms)	26.8 ± 2.6	27.8 ± 2.6	-4.56 ± 4.46	29/30***	0.996
	RMSSD (ms)	25.1 ± 3.1	27.1 ± 3.1	-15.2 ± 20.9	27/30***	0.970
Frequency Domain	Total Power (ms^2)	847 ± 165	890 ±174	-7.73 ± 9.08	28/30***	0.991
	VLF Power (ms^2)	299 ± 55.7	302 ±58	-2.2 ± 19.6	19/30	0.894
	LF Power (ms^2)	102 ± 18	106 ±18	-5.5 ± 19.1	28/30***	0.955
	LF Power (nu)	25.8 ± 2.5	23.3 ± 2.0	5.8 ± 22.6	23/30*	0.881
	HF Power (ms^2)	444 ± 103	480 ±108	-20.2 ± 23.0	28/30***	0.992
	HF Power (nu)	73.6 ± 2.5	76.2 ±2.1	-4.97 ± 9.74	23/30*	0.875
	LF/HF Ratio	0.413 ± 0.062	0.336 ± 0.041	8.3 ± 30.3	23/30*	0.866
Non-linear	$MSE_{\sum 1\text{-}39}$	29.9 ± 0.7	31.0 ± 0.8	-3.91 ± 9.23	16/30	0.921
	Shannon Entropy	3.81 ± 0.09	3.71 ± 0.09	2.48 ± 3.19	25/30**	0.948
	Approximate Entropy	1.24 ± 0.04	1.40 ± 0.05	-14.0 ± 15.1	29/30***	0.841
	Sample Entropy	1.26 ± 0.06	1.33 ± 0.027	-8.52 ± 9.55	29/30***	0.813
	DFA short-term (α_1)	0.949 ± 0.032	0.865 ± 0.024	7.4 ±13.9	23/30*	0.370
	DFA long-term (α_2)	0.948 ± 0.034	0.926 ± 0.033	2.09 ± 6.03	23/30*	0.907

Values are displayed as mean ± SEM, Bland-Altman intervals (mean bias ± 95% limits of agreement), bias consistency, and pairwise coefficient of determination (r^2) between HRV and PRV values. * $p < 0.05$, ** $p < 0.01$, *** $p < 0.001$ by Pearson's χ^2 test.

Table 2 – Indices of HRV and PRV derived from the diastolic minimum fiducial point for 30 baseline recordings

Category	Index	HRV	PRV	Bland-Altman Interval (%)	Bias Consistency	r^2
Time Domain	Heart rate (bpm)	187 ± 4	187 ± 4	-0.18 ± 0.44	27/30***	0.999
	SDNN (ms)	26.8 ± 2.6	28.4 ± 2.8	-7.0 ± 20.6	26/30***	0.887
	RMSSD (ms)	25.1 ± 3.1	29.6 ± 3.7	-26.0 ± 59.0	20/30	0.673
Frequency Domain	Total Power (ms^2)	847 ± 165	917 ± 178	-12.3 ±45.1	22/30*	0.918
	VLF Power (ms^2)	299 ± 55.7	293 ± 57	1.5 ±22.8	17/30	0.892
	LF Power (ms^2)	102 ± 18	101 ± 18	-1.0 ± 22.2	23/30*	0.947
	LF Power (nu)	25.8 ± 2.5	23.4 ± 2.4	3.7 ± 41.6	20/30	0.585
	HF Power (ms^2)	444 ± 103	520 ± 115	-37 ± 103	23/30*	0.833
	HF Power (nu)	73.6 ± 2.5	76.0 ± 2.5	-4.5 ± 14.6	20/30	0.577
	LF/HF Ratio	0.413 ± 0.062	0.363 ± 0.058	0.4 ± 71.4	20/30	0.664
Non-linear	$MSE_{\sum 1\text{-}39}$	29.9 ± 0.7	30.4 ± 0.9	-8.1 ± 12.3	17/30	0.762
	Shannon Entropy	3.81 ± 0.09	3.71 ± 0.076	2.17 ± 6.01	21/30*	0.792
	Approximate Entropy	1.24 ± 0.04	1.26 ± 0.052	-1.35 ± 8.20	20/30	0.921
	Sample Entropy	1.26 ± 0.06	1.24 ± 0.03	-0.90 ±5.05	20/30	0.922
	DFA short-term (α_1)	0.949 ± 0.032	0.831 ± 0.036	11.1 ± 19.7	23/30*	0.213
	DFA long-term (α_2)	0.948 ± 0.034	0.929 ± 0.035	1.87 ± 8.77	21/30*	0.808

Values are displayed as mean ± SEM, Bland-Altman intervals (mean bias ± 95% limits of agreement), bias consistency, and pairwise coefficient of determination (r^2) between HRV and PRV values. * $p < 0.05$, ** $p < 0.01$, *** $p < 0.001$ by Pearson's χ^2 test.